POLITECNICO DI MILANO
DEPARTMENT OF MECHANICAL ENGINEERING
DOCTORAL PROGRAMME IN MACHINE AND VEHICLE DESIGN

CRACK INITIATION AND GROWTH IN POWER PLANT STEELS

Doctoral Dissertation of:
Federico Bassi

Supervisor:
Prof. Stefano Beretta

Tutor:
Prof. Maurizio Vedani

The Chair of the Doctoral Program:
Prof.ssa Bianca Maria Colosimo

2016-2017 - XXIX Cycle

Abstract

In recent years, power generation industry is facing new issues given by the need to increase productivity as well as improve flexibility of production due to dispatching priority of alternative power sources. While in the past the target of higher productivity was reached with the development of new plants, nowadays the industry of power generation prefers to improve the performances of existing plants. In steam cycles for example, the efficiency of the energy conversion is optimized by increasing the operating temperature of the steam boiler. This action has a negative impact in the creep resistance of the boiler and its components, that were designed to operate at lower temperatures. On the other hand, the demand for flexibility directly affects the load cycles subject by the components. From this viewpoint, a large number of start-ups and load variations lead to a fatigue damage that has a detrimental effect on the residual life of the power plant. The interaction between the critical creep and fatigue conditions may then results in unexpected onset of cracks or premature failure of cracked bodies. In order to prevent this catastrophic scenario, periodic inspections are requested to identify the presence of defects and characterise their entity. However, in situ inspections are not always possible. The pressurized pipes of power plants for example, may present flaws on the inside surface. These defects are not easily detectable by modern non-destructive testing and even when detected, the estimation of the time to failure at the in service temperature is still a challenging topic. The development of reliable assessment strategies to evaluate the presence and the evolution of cracks is therefore strongly requested by the industry.

Lately, several international committees have developed codes to assess the acceptability of flaws in metallic structures for high temperature applications. Among these codes

it is worth mentioning EDF Energy R5 [10], British standard BS7910 [12], API 579 [5], and FITNET [24]. These procedures, despite the large scatter in creep and creep-fatigue resistance properties, divide materials into classes depending on their chemical composition, and tend to consider the lower resistance bound. This choice might result in an over conservative estimation of the residual life of the component. In this context, the availability of experimental data performed on the same batch material of the plant components, could drastically improve the assessments without affecting reliability. In addition to this, it is worth noting that even if standard calculation procedures have been sufficiently tested and verified, in some critical operating conditions, however, they tend to simplify the actual problem. Although in creep crack growth (CCG) conditions, the assessment is successfully performed and validated on components by using the crack tip parameter C^*, in creep-fatigue regime instead, it is treated by superposing creep and fatigue damages rather than analyze their interactions. However, experimental tests show that simple superposition of the phenomena is not always acceptable. From this point of view, the transposition to components of specific crack tip parameters still not considered by these standards, might result in a better quality of the assessments that could, in this way, consider the interactions between creep and fatigue.

The aim of this thesis is to study the relationship between crack propagation rates and crack tip parameters represents a material property that does not depend on the geometry of the cracked body, and thus it can be used in assessment procedures to evaluate the residual life of components operating at HT in both CCG and creep-fatigue (CFCG) conditions. Differently from the available codes, the assessment of a pressurized pipe subject to cyclic load was modeled by introducing the crack tip parameter of CFCG tests rather than simply superposing the two damages separately. This parameter is intended to represent the physical interactions between fatigue and creep.

To support this apporach, a high temperature (HT) resistance map for a modified P91 power plant steel produced by Tenaris has been built. The uniaxial creep data provided by Tenaris represents a starting point for the CCG, CGCG, and fatigue crack growth (FCG) tests performed at 600 °C, at different stress intensity factors, and at different hold times (CFCG only) in order to complete the HT resistance map. The results of these tests are used to define time-dependent crack tip parameters that govern crack propagation rates.

After a preliminary study dedicated to the identification of an opportune uniaxial creep model able to predict the viscous behavior at different stress conditions reliably, CCG and CFCG tests were performed. A constant monitoring of the load-line displacement through a high sensitivity transducer and crack size through the direct current potential drop method, was necessary to define the crack tip parameters that govern crack

propagation. The target of CCG tests was the identification of the two time dependent fracture mechanics parameters valid for steady-state creep and small-scale creep conditions respectively: the C^* integral and the C_t parameter. The C^* integral derives from Rice definition of integral J but accounts for the displacement vector rate introducing a time dependency that is typical of creep strains. If plotted in logarithmic scale with crack propagation rates, a linear relationship can be found representing the material behavior at HT independent from the geometry of the cracked body. The C^* parameter was also determined numerically from the load-line displacement records of 2D and 3D finite element (FE) simulations that combined the creep model by Graham-Walles [26] with a modified cavity growth theory by Cocks and Ashby [14] in order to predict CCG in compact tension C(T) specimens. The numerical C^* well correlated with the experimental values confirming the Graham-Walles as a valid creep model for FE simulations. In small-scale creep instead, the C_t parameter represents a measurable estimation of the C(t) integral that has a similar meaning of the C^* integral but is defined only on a limited contour close to the crack tip where the creep zone size is still dominant with respect to the elastic-plastic zones. The C_t parameter is then a crack driving parameter that is able to represent the transition between small-scale and extensive creep conditions since as per definition it trends to C^* at times higher than the transition ones.
During creep-fatigue tests at reasonable short hold times, the condition of extensive creep may not occur during a cycle. The crack tip parameter in this regime is represented by the $(C_t)_{avg}$ parameter that is defined as the integral of the C_t parameter evaluated at the hold time and requires the acquisition of crack propagation and load-line deflection during each cycle. Despite some scatter in the experimental data given by the complexity of the load-line displacement measurements during the hold time, the creep-fatigue crack growth rates exhibited a power law based trend with the $(C_t)_{avg}$ parameter. The main advantage of working with crack tip parameters is that they have been also formulated for a wide range of components, e.g. pressurized pipes with several crack configurations, according to the results of numerical simulations and thus they can be easily included in calculation codes. The fracture mechanisms of creep and creep-fatigue have been also studied with detailed micrographs of the crack front section showing that the crack propagation starts with voids concentration at the grain boundaries that coalesce originating creep micro-cavities. Micrographs prove the application of void growth continuum damage approaches to model CCG numerically.
A CCG assessment method was developed to model creep crack initiation (CCI) and growth in pressurized cylinders with circumferential/axial semi-elliptical defects. It is based on the combination of two main criteria, the two criteria diagram (2CD) and the

σ_{ref} based C^* approach recognised and accepted by the FITNET and BS7910 procedures respectively. The 2CD implemented in this analysis is strictly related to uniaxial creep data and the stress intensity factor calculated at crack initiation, i.e. a crack propagation of 0.2 mm, during CCG tests. The C^* parameter in case of pressurized pipes is C_ref and is defined by using the concept of reference stress under the hypothesis that steady-state creep generates a uniform stress distribution. CCI and CCG have been calculated as an example for a P91 pipe subject to internal pressure with an axial defect on the inside surface and compared with the procedure described in API 579 code applied with the material properties of 9Cr1MoV steel according to the MPC Omega method [42]. API 579 assessment is too conservative when compared with the combination of the 2CD and C_{ref} models. In creep-fatigue conditions instead, the residual life of a component depends not only on the creep properties of the material but also on the frequency of application of the load cycle. If the pressure is maintained for a long hold time t_h, the creep zone size has time to increase and dominate the cyclic plastic zone while when hold times are short enough, this does not happen and the creep zone is confined to the crack tip. The $(C_t)_{avg}$ parameter is able to characterize the crack propagation depending on the hold time and addresses the shortage of CFCG assessment procedures that actually account for the interaction mechanisms between creep and fatigue damage. It is defined under the hypotheses of complete and no creep reversal due to cyclic plasticity or, thanks to the creep reversal parameter C_R determined from experimental CFCG tests, for partial creep reversal. The $(C_t)_{avg}$ parameter was integrated in the R5 TDFAD approach to evaluate creep-fatigue crack initiation and propagation. The TDFAD procedure evaluates crack initiation by superposing the effects of creep and fatigue separately. It required the uniaxial creep data, CCG initiation data and fatigue crack growth (FCG) data in terms of Paris-Erdogan law that was collected from dedicated tests. CFCG is modelled according to the $(C_t)_{avg}$ parameter that was calculated for the same pipe geometry previously mentioned according to a combination of the analytical definition of the creep zone size and a numerical estimation of C^*. As expected, at low hold times (0.1 and 1 h) the fatigue damage becomes dominant reducing the residual life drastically. The case study at $t_h = 10h$ represents the actual operating condition of power plants and exhibited a propagation close to the pure CCG behaviour.

With the aim to improve the quality of future assessments, the C^* parameter of pressurized cylinders was investigated by means of FE analyses with different crack configurations. These simulations extend the aforementioned FE CCG analysis to large scale components and, if integrated with an opportune model of cyclic plasticity, they could represent the creep-fatigue interactions, one still challenging target of computational time dependent fracture mechanics.

Acknowledgements

I would like to thank Prof. Ashok Saxena for his comprehensive and informative discussions, as well as for his friendship.

Nomenclature

Symbols

$(C_t)_{avg}$ Crack tip parameter in creep-fatigue conditions

$(C_t)_{ssc}$ Crack tip parameter valid for small-scale creep conditions only

(da/dt) Crack propagation rate

$(da/dt)_{avg}$ Average crack propagation rate in CFCG

$2c$ Semi-elliptical crack shape

α Coefficient in $(C_t)_{avg}$ model

α' Multiaxial stress state parameter

α'' Semi-empirical function in the cavity growth theory

α''_0 Semi-empirical function for uniaxial conditions in the cavity growth theory

α^{dev} Deviatoric part of the backstress tensor

α_0 Multiplier in material elastic-plastic behavior

α_c Backstress tensor in Chaboche model

α_i Coefficient in creep load-line displacement rate model

α_k Backstress component

α_n Constant for creep zone size determination

β Coefficient in $(C_t)_{avg}$ model

β_0	Coefficient in Irwin's theory
χ'	Material constant in Kachanov model
χ''	Material constant in Liu-Murakami model
$\Delta\varepsilon^c$	Creep strain variation
Δa	Crack propagation variation
Δa_c	Creep crack propagation
Δa_f	Fatigue crack propagation
Δa_{cf}	Creep-fatigue crack growth
ΔK	Stress intensity factor range
ΔP	Load variation during fatigue cycles
Δt	Time step
ΔV_c	Load-line deflection variation during the hold time
ΔV_r	Load-line deflection range between 2 adjacent fatigue cycles.
δ	Normalised angle of semi-elliptical crack
$\Delta\dot{U}$	Energy rate variation
$\dot{\alpha}_k$	Backstress component evolution
$\dot{\bar{\varepsilon}}^p$	Equivalent plastic strain increment
$\dot{\Delta}^c$	Creep load-line displacement rate
$\dot{\omega}$	Damage evolution rate
$\dot{\sigma}$	Total stress rate
$\dot{\varepsilon}$	Total strain rate
$\dot{\varepsilon}^c$	Creep strain rate
$\dot{\varepsilon}_a$	Axial strain rate
$\dot{\varepsilon}_r$	Radial strain rate
$\dot{\varepsilon}_{ref}$	Reference strain rate
$\dot{\varepsilon}_{ss}$	Steady-state creep strain rate

$\dot{r}_c$	Creep zone size rate
$\dot{U}$	Energy rate
$\dot{u}_i$	Components of the displacement rate vector
$\dot{U}_t$	Energy rate variation in transient creep
$\dot{V}_c$	Creep load-line deflection rate
$\dot{V}_{ss}$	Steady-state load line deflection rate
$\dot{W}_E$	Strain energy density rate
η	Coefficient in C^* generic definition
η^{LLD}	Coefficient in C^* definition of ASTM E1457
η_1	Calibration function for C^* determination
Γ	Contour around the crack tip
γ	coefficient for limit stress solution
γ_k	Coefficient in backstress components evolution
$\hat{r}_c$	Angular-dependent function in Adefris' creep zone size definition
λ	Coefficient in creep isochronous curves
ν	Poisson ratio
ω	Damage
Φ	Coefficient in creep load-line displacement rate model
ϕ	Exponent of the da/dt vs. C^* relation
ϕ'	Exponent for da/dt vs. C_t relation
ϕ''	Coefficient in $(da/dt)_{avg}$ vs. $(C_t)_{avg}$ relation
σ	Applied stress
σ_0	Yield stress
σ_1	Maximum principal stress
σ_a	Axial stress
σ_h	Hydrostatic stress

$\sigma_{0.2}^{c}$	0.2% proof stress from average isochronous stress-strain curves
σ_{0cp}	Cyclic yield stress
σ_{ax}	Axial stress
σ_{eq}	Equivalent stress
$\sigma_{n,pl}$	Nominal stress
σ_{ref}	Reference stress
σ_{R}	Rupture stress
Triax	Triaxial stress
θ	Angle taken from the semi-elliptical crack surface
ε	Total strain
ε_{f}^{*}	Multiaxial creep ductility
ε^{c}	Creep strain
$\varepsilon_{exp.}^{c}$	Experimental creep strain
$\varepsilon_{pred.}^{c}$	Predicted creep strain
ε^{e}	Elastic Strain
ε^{p}	Plastic strain
ε_{0}	Yield strain
ε_{f}	Uniaxial creep ductility
ε_{ref}	Total reference strain
φ'	Material constant in Kachanov model
ϑ	Angle from the crack tip
ξ_{cp}	Constraint factor in cyclic plastic theory
A	Norton law multiplier
a	Crack length
A'	Material constant in Kachanov model
A''	Material constant in Liu-Murakami model

a_0	Initial crack length
A_i	Material constant in Graham-Walles model
a_{eff}	Effective crack length
$A_{i,i}$	Coefficients for $G_{0,1}$ coefficients determination
A_{pl}	Plastic are used to calculate the J integral
B	C(T) specimen thickness
b	Remaining ligament ahead of the crack tip
B'	Material constant in Kachanov model
B''	Material constant in Liu-Murakami model
b_c	Material parameters in isotropic hardening law
B_n	Net section thickness
C	Paris law multiplier
c	Exponent in the t_T vs. σ_R relation
$C(t)$	C(t)-integral in small-scale creep
C^*	Crack tip parameter in steady state creep conditions
C_0	Material constant of Larson Miller model
C_1	Material constant for material creep toughness determination in TDFAD approach
C_i	Elastic compliance
C_k	Coefficient in backstress components evolution
C_R	Creep reversal parameter
C_t	Crack tip parameter valid for small-scale and extensive creep conditions
C_{ref}	Reference crack tip parameter in creep conditions
COD_f	Final crack opening displacement of J_{IC} tests
D	Multiplier of the da/dt vs. C^* relation
d	Grain size

D' Multiplier for da/dt vs. C_t relation

D'' Coefficient in $(da/dt)_{avg}$ vs. $(C_t)_{avg}$ relation

D_1 Material constant for material creep toughness determination in TDFAD approach

D_v Material parameter in CFCG model

D_{AC} Damage after crack according to API RP 579

D_{BC} Damage before crack according to API RP 579

E Elastic modulus

F Shape function

f Frequency

F^I Derivative of the shape function

F_0 Coefficient in C^* definition

f_c Void fraction at coalescence

f_h Area fraction of voids in grain boundary

f_i Initial void fraction

f_z Area fraction of voids in the arbitrary boundary

$F_{cr}(\theta, n)$ Creep angular function

f_{ps} Coefficient for plastic collapse load determination

G Parameter used in the cavity growth theory

G_i Coefficients for stress intensity factor determination

H Multiplier in the t_R vs. σ_R relation

H^{LLD} Coefficient in C^* definition of ASTM E1457

h_1 Calibration function for determining C^*

h_3 Calibration function for determining the load-line displacement rate $\dot{V}_{ss}$

I_n Parameter in stress fields formulation

J Crack tip parameter for elastic-plastic fracture mechanics

J_{el}	Elastic component of the J integral
J_{IC}	Critical J-Integral at initiation
K	Nominal stress intensity factor
K_0	Stress intensity factor at the beginning of the test
K_r	Fracture thoughness parameter in TDFAD approach
K_{Ii}	Stress intensity factor at initiation
K_{mat}	Material total fracture toughness considering creep and fatigue
$K_{max,0}$	Maximum initial stress intensity factor
K_{ri}	Fracture toughness parameter in TDFAD approach
l	Half distance between voids
L_r	Plastic collapse parameter in TDFAD approach
L_r^{max}	Limit line for plastic collapse in TDFAD approach
L_{el}	Average element size
LLD	Load-line displacement
LS	Least squares
m	Paris law exponent
m'	Material constant in Kachanov model
m''	Material constant in Liu-Murakami model
m_0	Exponent in material elastic-plastic behavior
M_i	Coefficients for determining $G_{2,3,4}$
m_i	Material constant in Graham-Walles model
m_{cp}	Exponent in cyclic plastic theory
M_{in}	Coefficient for plastic collapse load determination
N	Number of cycles
n	Norton law exponent
n'	Material constant in Kachanov model

n'' Material constant in Liu-Murakami model

n_i Material constant in Graham-Walles model

N_{bs} Number of backstress

P Applied load

P_0 Coefficient in numerical estimation of C^* parameter

P_i Pipe internal pressure

p_L Plastic collapse load

P_R Creep reversal constant

P_{LM} Larson Miller parameter

Q Coefficients in TDFAD approach

q_1 Material constant for material creep toughness determination in TDFAD approach

q_2 Material constant in Liu-Murakami model

Q_∞ Material parameters in isotropic hardening law

R Load ratio

r Radial distance from the crack tip

R_σ TCD Ligament damage parameter

r_c Creep zone size radius

r_i Inner radius of a pipe

R_K TCD crack tip damage parameter

r_o Outer radius of a pipe

r_{cp} Cyclic plastic zone size

S Deviatoric stress tensor

s Arc length of the contour Γ

S_{ij} Deviatoric stress

T Temperature

t Time

t_A Assessment time

t_c Time to coalescence of voids

t_h Hold time

T_i Components of the traction vector

t_i Initiation time

t_R Rupture time

t_T Transition time from small-scale creep to extensive creep

t_{CCG} Time of CCG propagation

t_{exposure} Total exposure time of a component at high temperature

t_{T} Transition time from small-scale creep to steady-state creep condition

V Volume of the cylinder in the cavity growth theory

V_0 Instantaneous load-line deflection

V_c Creep load-line deflection

V_t Total load-line deflection

W C(T) specimen width

w Pipe wall thickness

z Arbitrary half distance comprehended between l and w in the cavity growth theory

Acronyms

2CD Two criteria diagram

C(T) Compact tension

CCG Creep crack growth

CCI Creep crack initiation

CFCG Creep-fatigue crack growth

CFCI Creep-fatigue crack initiation

COD Crack opening displacement

EC Extensive creep

EPFM Elastic-plastic fracture mechanics

FCG Fatigue crack growth

FE Finite Element

HRR Hutchinson Rice and Rosengren stress fields

HT High temperature

LCF Low cycle fatigue

LEFM Linear elastic fracture mechanics

PD Potential drop

SEM scanning electron microscope

SSC Small-scale creep

TC Transition creep

TDFAD Time dependent failure assessment diagram

TDFM Time dependent fracture mechanics

Contents

List of Figures

List of Tables

CHAPTER 1

Analysis of Cracks in Creep and Creep-Fatigue Regime

Most of the components operating in the power generation industries must deal with critical operating conditions due to the high temperature (HT) and the sustained load cyclically reached, due to the sequence of start-ups and shut-downs. Under these conditions, creep damage can occur widespread, interesting the entire structure, or localized, e.g. at the crack tip of geometrical defects.
In modern power plant components, the first kind of damage is unlikely to happen due to the high attention paid in the creep resistance design, deriving from considerable knowledge about the behavior of materials under HT. The latter, instead, is a more insidious issue, dependent on the presence of defects that may derive from manufacturing or operating at critical conditions. In this case, the cracked component might be subjected to creep crack growth (CCG) and creep-fatigue crack growth (CFCG) even at low loading conditions.
This Chapter deals with the main aspects associated to time dependent fracture mechanics in creep and creep-fatigue regime of components operating at high temperature.
A review of the crack tip parameters for characterizing creep crack growth, and how they are calculated, in extensive and small-scale creep conditions, by analytical ap-

proach and/or from the load-line displacement records is presented.
The fracture mechanics parameter valid for small-scale creep conditions are extended to describe creep-fatigue crack growth, after appropriate integration during the hold time of the load cycle.
The energy rate definition of these crack tip parameters is given and the extension to pipe components operating at high temperature, as covered by several assessment codes, is discussed.

1.1 Creep Crack Growth

Since the concepts of linear elastic fracture mechanics (LEFM) and elastic-plastic fracture mechanics (EPFM) do not deal with creep strains, it is evident that a new approach shall be followed to characterize crack growth at high temperature: the time dependent fracture mechanics (TDFM). TDFM does not exclude LEFM and in addition to this is strictly related to the concepts of EPFM. A component subjected to high temperature (T exceeds the 35% of material's melting temperature) and a sustained load presents an irreversible creep strain ε^c that has the typical behavior of Fig. 1.1. It is made up by three main zones:

- primary creep (zone I): it happens right after the loading phase and is characterized by a fast decrease of the creep strain rate $\dot{\varepsilon}^c$. It lasts for a limited amount of time.
- steady-state creep (zone II): it starts after the primary creep and is characterized by a constant creep strain rate for the material under investigation. For a large class of materials, including the power plant steel of interest in this thesis, it is the longest phase in a creep test. Most of the components operate under steady-state creep conditions and for this reason most of the following crack tip parameter will be defined under these conditions.
- tertiary creep (zone III): it is characterized by rapid increase in the creep strain rate until rupture. The components that work at high temperatures are not designed to operate under these critical conditions.

During steady-state creep the creep strain rate $\dot{\varepsilon}_{ss}$ is mainly defined by the Norton law:

$$\dot{\varepsilon}_{ss} = A\sigma^n \tag{1.1}$$

where A and n are material constants fitted to uniaxial creep data and σ is the applied stress. Under steady-state creep, the stress field at crack tip can be described by the combination of three different zones as shown in Fig. 1.2:

- P. is the plastic zone characterized by the crack tip parameters K and J integral.

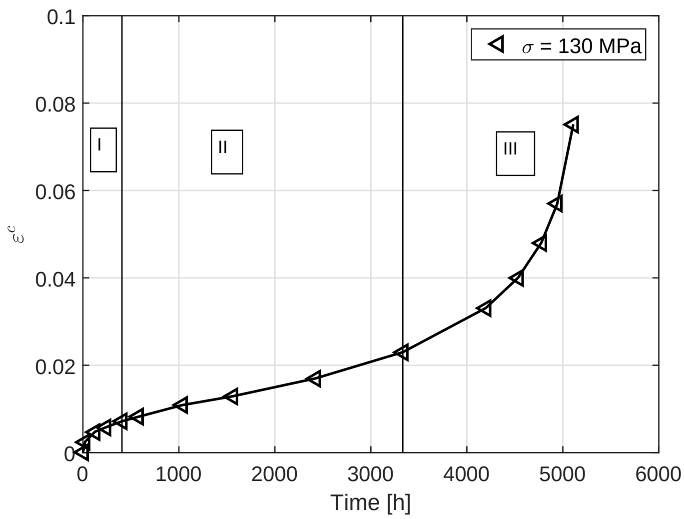

Figure 1.1: *Uniaxial creep curve of P91 at 600°C.*

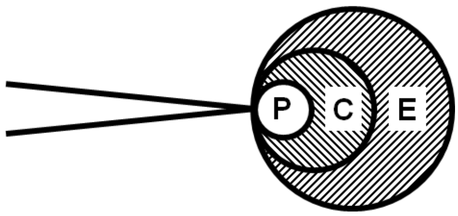

Figure 1.2: *Stress fields at the crack tip during steady state creep.*

- E. is the elastic zone if the small-scale yielding conditions are verified, i.e. the yield radius is limited to a zone confined to the crack tip. In case this condition is not verified, the elastic zone is completely replaced by the plastic zone.

- C. is the creep zone characterized by stress relaxation due to creep strain.

The size of the creep zone is strictly related to the creep behavior of the material as well as the crack propagation rate. In a stationary crack, for example, the creep zone is likely to increase becoming dominant. When the creep zone size is relatively small compared to the elastic and plastic zones, J and K still remain the crack tip parameters to define the crack propagation rate. However when the creep zone size is comparable to the elastic and plastic zone sizes, J and K loses their meaning and thus new parameters that accounts for time dependent deformation should be defined. The typical creep zone size evolution is shown in Fig. 1.3. Three different zones are identified:

- small-scale creep (SSC) i.e. when the creep zone is confined to the crack tip and is small compared with the elastic zone;

- transition creep (TC). The creep zone size has increased to its maximum radius;

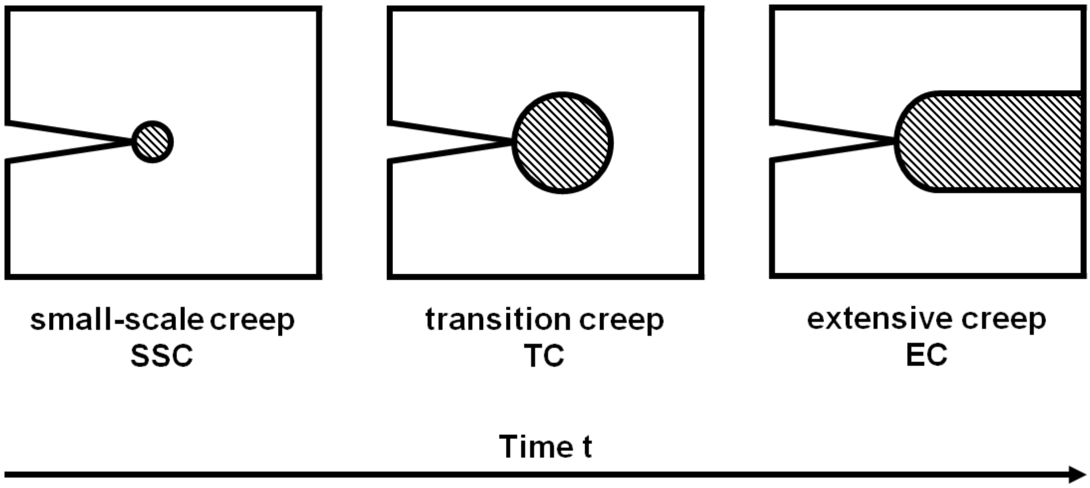

Figure 1.3: *Creep zone evolution with time.*

- extensive creep (EC). The creep zone size is extended to all the remaining ligament of the cracked component. This condition is reached when the creep strain is in the steady-state of Fig. 1.1.

The simplest parameters that characterize crack tip stress field in CCG regime are defined in EC conditions, because the steady-state creep zone is constant and, therefore, no interactions with the elastic-plastic zones are considered. For this reason they will be discussed earlier than the crack tip parameters under SSC and TC which are more complicated to be defined, although under the assumptions of stationary cracks they may also be obtained.

1.1.1 The C^* Integral

When a specimen is subjected to high temperature and a sustained load for a sufficient amount of time to reach the steady-state creep, the creep strain rate $\dot{\varepsilon}^c$ can be expressed as a function of the applied stress σ according to Eq. (1.1). This expression is analogous in case of plastic strain ε^p:

$$\frac{\varepsilon^p}{\varepsilon_0} = \alpha_0 \left(\frac{\sigma}{\sigma_0}\right)^{m_0} \tag{1.2}$$

where σ_0 and ε_0 are normalization values commonly taken as yield strength and strain and α_0 and m_0 are material constants obtained by fitting a tensile test. Proceeding with the analogy between the creep strain rates and the plastic strains, if $\dot{\varepsilon}^c$ then

$$A = \frac{\alpha_0 \varepsilon_0}{\sigma_0^{m_0}} \tag{1.3}$$

$$n = m \tag{1.4}$$

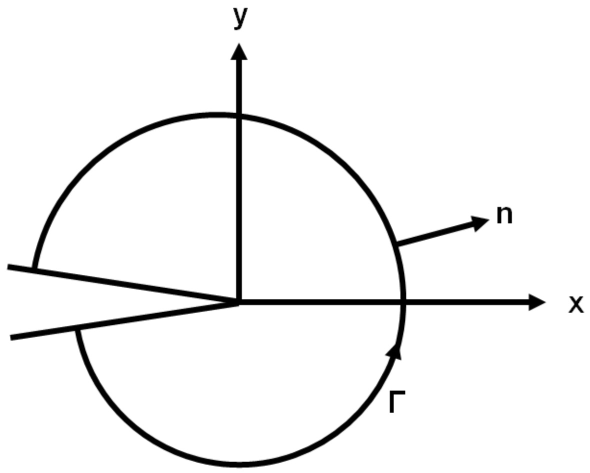

Figure 1.4: *Schematic draw of the line contour used to define C^* integral.*

With Eqs. (1.3) and (1.4) Landes and Begley [15] and at the same time Nikbin et al. [34], modified the expression of J integral by Rice [43] by changing from the displacement vector u to its derivative $\dot{u}$:

$$C^* = \int_\Gamma \dot{W}_E dy - T_i \left(\frac{\partial \dot{u}_i}{\partial x} \right) ds \tag{1.5}$$

In Eq. (1.5) Γ is a line contour taken counter-clockwize from crack's lower surface to upper surface (Fig. 1.4), $\dot{W}_E$ is the strain energy rate density, T_i is the traction vector defined by the outward normal n_j and s is the arc length of the contour. The strain energy rate density can be related to the point stress σ_{ij}:

$$\dot{W}_E = \int_0^{\dot{\varepsilon}_{ij}} \sigma_{ij} d\dot{\varepsilon}_{ij} \tag{1.6}$$

One of the main aspects that candidate the C^* integral as a crack tip parameter in EC conditions is its path independence that can be demonstrated by considering the closed line contour of Fig. 1.5. Because of a closed line contour the sum of the C^* integrals shall be null.

$$C^*_{\Gamma_1} + C^*_{\Gamma_2} + C^*_{\Gamma_3} + C^*_{\Gamma_4} = 0 \tag{1.7}$$

but since the line contours Γ_2 and Γ_4 are approximately parallel to the x axis, $dy = 0$ as well as the traction vectors T_i. Thus $C^*_{\Gamma_1} = -C^*_{\Gamma_3}$ demonstrating the path independence of the C^* integral. In the same work Landes and Begley [15] gave an energy rate interpretation of the C^* integral by analysing the load-line deflection of two identical specimens that have a different initial crack length, a_0 and $a_0 + \Delta a$, loaded at the same load level P. If multiple specimen couples are loaded at different loads it is possible to obtain the load variation as a function of the steady-state load-line deflection rate. At a fixed $\dot{V}_{ss}$ value, the energy rate or the stress power input $\dot{U}$ to a cracked body is

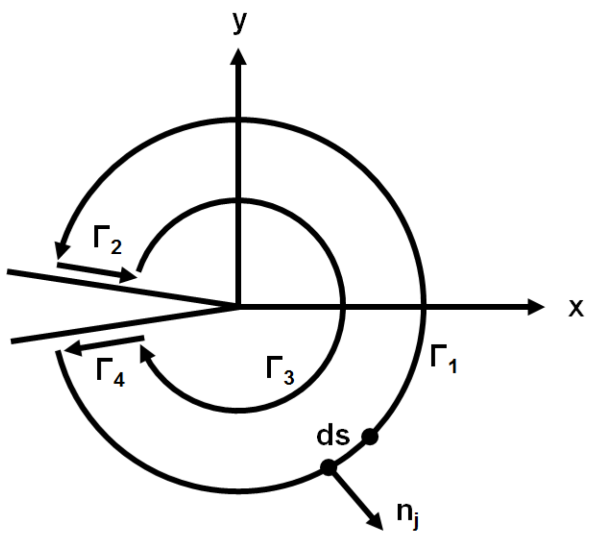

Figure 1.5: *C^* integral path independence demonstration.*

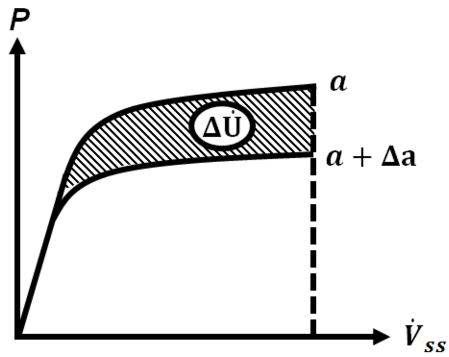

Figure 1.6: *Energy rate interpretation of the C^* integral.*

represented by the area underneath the plot of Fig. 1.6. Thus during a crack propagation from a_0 to $a_0 + \Delta a$ the stress input variation $\Delta\dot{U}$ is given by the difference between $\dot{U}(a)$ and $\dot{U}(a + \Delta a)$. C^* integral can be expressed equal to:

$$C^* = -\frac{1}{B}\frac{d\dot{U}}{da} \tag{1.8}$$

where B is the thickness of the cracked body. Another important step to validate the C^* integral as a crack tip parameter is to find a relationship with the crack tip stress fields. Goldman and Hutchinson [25] found this relationship valid in EC conditions starting from the Hutchinson Rice and Rosengren (HRR) stress fields:

$$\sigma_{ij} = \left(\frac{C^*}{I_n A r}\right)^{1/(1+n)} \hat{\sigma}_{ij}(\vartheta, n) \tag{1.9a}$$

$$\dot{\varepsilon}_{ij} = A\left(\frac{C^*}{I_n A r}\right)^{n/(n+1)} \hat{\varepsilon}_{ij}(\vartheta, n) \tag{1.9b}$$

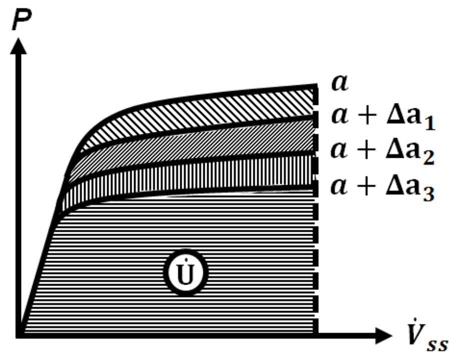

Figure 1.7: *Schematic plot of the test load as a function of the steady-state load-line deflection.*

where r is the radial distance from the crack tip, ϑ is the considered angle and $\hat{\sigma}_{ij}$ and $\hat{\varepsilon}_{ij}$ are angular functions. The expressions for I_n are obtained by the HRR definition for plane stress and plane strain conditions:

$$I_n = 6.568 - 0.4744n + 0.04042n^2 - 0.001262n^3 \qquad \text{P. Strain} \qquad (1.10a)$$

$$I_n = 4.546 - 0.2827n + 0.0175n^2 - 0.45816n^3 \qquad \text{P. Stress} \qquad (1.10b)$$

After the previous considerations, the C^* integral has been widely accepted as a crack tip parameter to correlate creep crack growth rates in extensive creep conditions. The next step is to discuss the methods to allow its estimation. There are three possible ways to determine C^*:

- Experimental methods;
- Semi-empirical methods;
- Numerical solutions.

Experimental determination of C^* integral

The experimental method for determining C^* was studied by Landes and Begley [15]. It consists in the analysis of the load-line deflection rate $\dot{V}_{ss}$ of a set of identical specimens with different crack lengths a tested at different load levels for sufficient time to reach steady-state creep conditions (Fig. 1.7). At different load-line deflection rate it is possible to express the energy rate $\dot{U}$ as a function of the crack size a as shown in Fig. 1.8. The slope of each curve is simply related to C^* by Eq. (1.8). Although the C^* obtained with this method is valid for all the specimen configurations, it requires a great number of specimens.

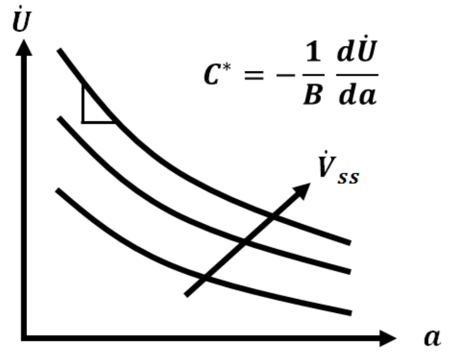

Figure 1.8: *Schematic plot used to calculate C^* experimentally.*

Semi-empirical method to determine C^* integral

A semi-empirical method to determine C^* can be derived by applying the following relationships to Eq. (1.8):

$$C^* = \frac{1}{B}\int_0^{\dot{V}_{ss}} \left(\frac{\partial P}{\partial a}\right)_{\dot{V}_{ss}} d\dot{V}_{ss} \tag{1.11}$$

$$C^* = \frac{1}{B}\int_0^{P} \left(\frac{\partial \dot{V}_{ss}}{\partial a}\right)_{P} dP \tag{1.12}$$

During EC the load-line displacement rate $\dot{V}_{ss}$ is related to the load P according to Eq. (1.13):

$$\dot{V}_{ss} = \phi\left(\frac{a}{W}, n\right) P^n \tag{1.13}$$

Where W is the width of the cracked body and n is the exponent of the Norton power law. Combining Eqts (1.13) and (1.11)) the C^* can now be expressed for known geometries. In Eq. (1.14) the C^* solution for a compact tension (CT) specimen with $a/W > 0.40$ is reported:

$$C^* = \frac{P\dot{V}_{ss}}{B(W-a)}\phi(a/W, n)\frac{n}{n+1} \tag{1.14}$$

where $\phi(a/W, n) = (2 + .522(1 - a/W))$ and $(W - a)$ is the length of the remaining ligament ahead of the crack tip. Several expressions of $\phi(a/W, n)$ function exists for a wide range of testing specimen geometries.

Numerical solution to determine C^* integral

A possible way to calculate the C^* parameter is through finite element (FE) analyses. This approach starts from the numerical estimation of J integral according to Eq. (1.15):

$$J = \alpha_0\sigma_0\varepsilon_0(W-a)h_1(a/W, m_0)\left(\frac{P}{BP_0}\right)^{m_0+1} \tag{1.15}$$

where h_1 is a calibration function fitted to numerical simulations that for CT specimens has the values reported in Tab. 2.12, and P_0 depends on another calibration function η_1:

$$\begin{aligned} P_0 &= 1.455\eta_1(W-a)\sigma_0 \qquad \text{P. Strain} \\ P_0 &= 1.071\eta_1(W-a)\sigma_0 \qquad \text{P. Stress} \end{aligned} \tag{1.16}$$

with:

$$\eta_1 = \left[\left(\frac{2a}{W-a}\right)^2 + 2\left(\frac{2a}{W-a}\right) + 2\right]^{1/2} - \left[\left(\frac{2a}{W-a}\right) + 1\right] \tag{1.17}$$

By performing a substitution according to Eq. (1.3) and (1.4), C^* parameter as well as steady-state load-line displacement rate $\dot{V}_{ss}$ can be determined according to the following equations:

$$C^* = A(W-a)h_1\left(\frac{a}{W}, n\right)\left(\frac{P}{1.455\eta_1 B(W-a)}\right)^{n+1} \tag{1.18a}$$

$$\dot{V}_{ss} = Aah_3\left(\frac{a}{W}, n\right)\left(\frac{P}{1.455\eta_1 B(W-a)}\right)^{n} \tag{1.18b}$$

where h_3 is an analogous of h_1.

Crack Growth Rate - C^* correlation

Once that C^* is determined by means of different methods, different authors, e.g. Saxena [51], demonstrated its ability to represent the creep crack propagation in EC conditions in different specimen geometries and components validating once again its use as a crack tip parameter able to correlate the crack propagation rate in creep regime as:

$$\frac{da}{dt} = D \cdot (C^*)^{\phi} \tag{1.19}$$

with D and ϕ material constants.

1.1.2 Crack tip parameters in small-scale/transition creep

The study of CCG under the hypothesis of extensive creep conditions is justified by the fact that at high temperatures, the longest period of time is spent in steady-state creep. However a residual life estimation of a component, performed by just considering EC conditions, might be non-conservative because the stress at the crack tip may be significantly lower then under SSC/TC conditions. For this reason, the crack tip stress fields defined in Eq. (1.9a) and b) may be updated for SSC/TC conditions, by considering an elastic-viscous behaviour of the material under power-law creep according to Eq. (1.20):

$$\dot{\varepsilon} = \frac{\dot{\sigma}}{E} + A\sigma^n \tag{1.20}$$

where $\dot{\varepsilon}$ and $\dot{\sigma}$ are the total strain rate and stress of the material. Equation (1.20) can be easily integrated in the time t obtaining the total strain ε:

$$\varepsilon = \frac{\sigma(t)}{E} + \int_0^t A(\sigma(\tau))^n d\tau \tag{1.21}$$

Riedel and Rice [29] rewrote Eq. (1.21) in order to find a unique relationship between stress and strain:

$$\varepsilon = \frac{\sigma(t)}{E} + Af(t)(\sigma(t))^n \tag{1.22}$$

where E is the elastic modulus and

$$f(t) = \int_0^t \left(\frac{\sigma(\tau)}{\sigma(t)}\right)^n d\tau \tag{1.23}$$

at a constant value of t Eq. (1.22) becomes:

$$\varepsilon = \frac{\sigma}{E} + Af(t)\sigma^n \tag{1.24}$$

That is written in the same form of the Ramberg-Osgood relation in elastic-plastic material properties ($\varepsilon = \sigma/E + \alpha_0(\sigma/E)^{m_0}$). Stress σ is then uniquely related to the strain ε so that J is path independent. Thus HRR stress fields of Eq. (1.9a) and b) can be rewritten:

$$\sigma_{ij} = \sigma_0 \left(\frac{J}{\alpha_0\sigma_0\varepsilon_0 I_m r}\right)^{\frac{1}{1+m_0}} \hat{\sigma}_{ij}(\vartheta, m_0) = \left[\frac{J}{I_n A f(t) r}\right]^{\frac{1}{n+1}} \hat{\sigma}_{ij}(\vartheta, n) \tag{1.25a}$$

$$\varepsilon_{ij} = \alpha_0\varepsilon_0 \left(\frac{J}{\alpha_0\sigma_0\varepsilon_0 I_m r}\right)^{\frac{m_0}{1+m_0}} \hat{\varepsilon}_{ij}(\vartheta, m_0) = Af(t)\left[\frac{J}{I_n A f(t) r}\right]^{\frac{n}{n+1}} \hat{\varepsilon}_{ij}(\vartheta, n) \tag{1.25b}$$

With $I_m = I_n$. Since $\sigma_{ij} \propto [1/f(t)]^{1/(n+1)}$ Eq. (1.23) becomes:

$$f(t) = \int_0^t \left[\frac{f(t)}{f(\tau)}\right]^{\frac{n}{n+1}} d\tau \tag{1.26}$$

By trial and error it has been found that the solution of this integral is:

$$f(t) = (n+1)t \tag{1.27}$$

By substituting the solution of Eq. (1.27) into Eq. (1.25a) and considered that in small-scale yielding conditions J integral is related to the stress intensity factor K by Eq. (1.28):

$$J = \frac{K^2}{E}(1-\nu^2) \tag{1.28}$$

the HRR stress fields are rewritten according to:

$$\sigma_{ij} = \left[\frac{K^2(1-\nu^2)}{EI_n A(n+1)tr}\right]^{\frac{1}{n+1}} \hat{\sigma}_{ij}(\vartheta, n) \tag{1.29a}$$

$$\varepsilon_{ij} = \left[\frac{K^2(1-\nu^2)}{EI_n A(n+1)tr}\right]^{\frac{n}{n+1}} A(n+1)t\hat{\varepsilon}_{ij}(\vartheta, n) \tag{1.29b}$$

If Eq. (1.29a) is derived it is possible to express the strain rate $\dot{\varepsilon}_{ij}$:

$$\dot{\varepsilon}_{ij} = A \left[\frac{K^2(1-\nu^2)}{EI_n A(n+1)tr} \right]^{\frac{n}{n+1}} \hat{\varepsilon}_{ij} \tag{1.30}$$

All the equations that describe the stress fields in SSC conditions depend on time and on the extension of the creep zone size r which from now on will be identified as r_c. Equation (1.29a),1.29b), and (1.30) are valid only until the transition, from SSC/TC to EC conditions, occurs at the crack tip.

Estimation of the creep zone size r_c

Riedel and Rice [29] proposed a definition of the creep zone size as the radius from the crack tip where creep strain ε^c is equal to the elastic strain ε^e. Through numerical simulations they have characterized the creep zone size as a function of proper angular functions F_{cr} defined in plane stress and strain conditions for different values of the Power law exponent n:

$$r_c(\vartheta, n) = \frac{1}{2\pi} \left(\frac{K}{E} \right)^2 \left[\frac{(n+1)I_n E^n At}{2\pi(1-\nu^2)} \right]^{\frac{2}{n-1}} F_{cr}(\vartheta, n) \tag{1.31}$$

that can be rewritten:

$$r_c(\vartheta, n) = \frac{1}{2\pi} \left[\frac{(n+1)^2}{2n\alpha_n^{n+1}} \right]^{\frac{2}{n-1}} K^2 (EAt)^{\frac{2}{n-1}} F_{cr}(\vartheta, n) \tag{1.32}$$

where α_n^{n+1} is a coefficient that for $3 < n < 13$ is equal to 0.69. The angular functions F_{cr} are shown for different values of n and ϑ in Fig. 1.9 as continuous lines. Adefris et al. [40] gave an alternative definition of the creep zone size as the radius where the creep strains ε^c are equal to 0.2% changing Eq. (1.31) to:

$$r_{c,0.2\%}(\vartheta, n) = \left[\frac{(n+1)A}{.002} \right]^{\frac{n+1}{n}} \frac{(1-\nu^2)K^2}{(n+1)AEI_n} t^{\frac{1}{n}} \cdot \hat{r}_c(\vartheta, n) \tag{1.33}$$

where $\hat{r}_c$ is an angular-dependent function. This expression of the creep zone size is more stable with respect to the one of Eq. (1.31) when $n = 1$. In this condition Eq.(1.33) shows a linear growth of the creep zone size with time. A transition time t_T can now be defined by equating the equations that define the stress fields in SSC/TC (Eq. 1.29a) and in EC (Eq. 1.9a):

$$t_T = \frac{K^2(1-\nu^2)}{E(n+1)C^*} \tag{1.34}$$

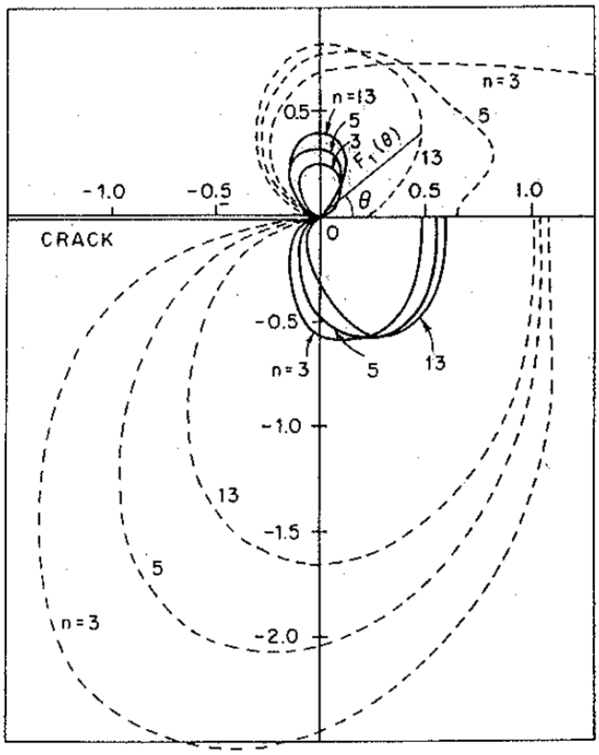

Figure 1.9: *Angular functions F_{cr} to determine the creep zone size according to Riedel and Rice [29]: upper half = plane strain, lower half = plane stress*

$C(t)$ **Integral**

Bassani and McClintock [7] demonstrated that in SSC the crack tip stress fields can be related to the $C(t)$ integral calculated at a contour line close to the crack tip Γ:

$$C(t) = \int_{\Gamma \to 0} \dot{W}_E dy - T_i \frac{\partial \dot{u}_i}{\partial x} ds \tag{1.35}$$

Equation (1.35) is similar to the C^* integral definition of Eq. (1.5), with the difference that is calculated close to the crack tip where the creep is dominant. In their work Bassani and McClintock [7] found a relationship between the $C(t)$ integral and the HRR stress fields:

$$\sigma_{ij} = \left(\frac{C(t)}{AI_n r} \right)^{\frac{1}{n+1}} \hat{\sigma}_{ij} \tag{1.36a}$$

$$\dot{\varepsilon}_{ij} = A \left(\frac{C(t)}{AI_n r} \right)^{\frac{n}{n+1}} \hat{\varepsilon}_{ij} \tag{1.36b}$$

If the stress fields of Eq. (1.29a) and (1.36a) it is possible to demonstrate that when $r \to 0$:

$$\frac{K^2(1-\nu^2)}{E(n+1)t} \approx C(t) \tag{1.37}$$

Thus $C(t)$ shall become equal to C^* when EC conditions are reached becoming path independent. This consideration in summarized in Eq. (1.38):

$$C(t) \approx \frac{K^2(1-\nu^2)}{E(n+1)t} + C^* \tag{1.38}$$

that combined with the definition of transition time t_T (Eq. 1.34) becomes:

$$C(t) = \left(1 + \frac{t_T}{t}\right) C^* \tag{1.39}$$

$C(t)$ integral is then valid for the entire range of creep deformation covering SSC, TC, and EC. Although, in SSC, TC, and EC regimes, the $C(t)$ definition as a contour integral at a contour line $\Gamma \to 0$ represents a limitation with respect to the practical application of this parameter. In fact, with the definition for $\Gamma \to 0$, it is not possible to measure this parameter on the basis of the load-line displacement under SSC and TC and, as a consequence, the $C(t)$ parameter can not be used as crack tip parameter able to correlate creep crack growth in SSC and TC regime. In addition to this, FE simulations proved that Eq. (1.38) is very sensitive to the creep constants A and n affecting the reliability of its estimation as proved by Saxena [50] (Fig. 1.10).

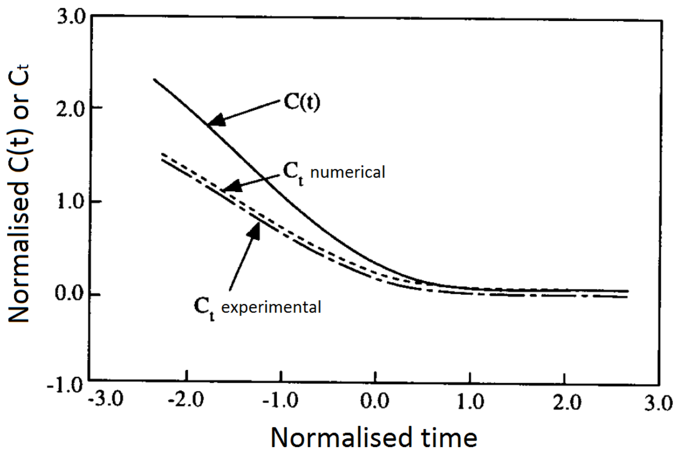

Figure 1.10: *Comparison between the analytical estimation of $C(t)$ according to Eq. (1.38) and the numerical and experimental estimation of an alternative crack tip parameter C_t [50].*

C_t parameter

To overcome this difficulty, Saxena [49] proposed a new crack tip parameter, C_t that also tends to C^* in EC condition as $C(t)$ parameter, moreover, according to its definition, it is measurable at the load-line displacement, also in SSC and TC regimes. C_t parameter is defined under the hypotheses that no crack extension occurs and that a linear elastic response occurs at the load application. If several pairs of identical specimens with different crack sizes (a and $a + \Delta a$) are tested at different load conditions

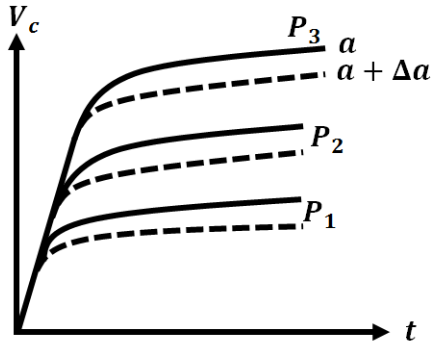

Figure 1.11: *Creep load-line displacement of coupled specimens with different crack sizes loaded at different stress levels.*

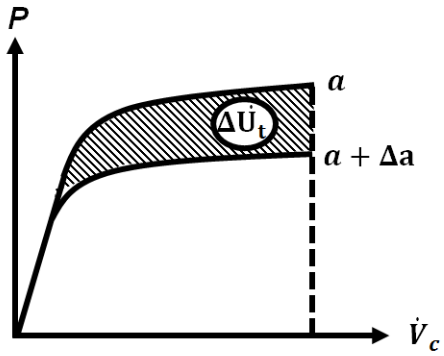

Figure 1.12: *Schematic draw of the meaning of the energy rate variation in transient creep.*

it is possible to analyze the change in the creep load-line deflection V_c as shown in Fig. 1.11. If a time t in SSC is considered (i.e. $t/t_T << 1$), the difference of the areas under the plot of the applied stress as the function of creep load-line deflection rate $\dot{V}_c$ for the two crack lengths of Fig. 1.12 represents the instantaneous stress power supplied to two cracked bodies tested with the same creep strain histories $\Delta\dot{U}_t$. The C_t parameter can be related to the energy rate variation according to Eq. (1.40):

$$C_t = -\frac{1}{B}\frac{\partial \dot{U}_t(a, t, \dot{V}_c)}{\partial a} \tag{1.40}$$

This equation represents the energy rate interpretation of the crack tip parameter C_t, where the time dependency can be observed.
In order to be able to determine C_t experimentally a relationship between load P, creep load-line deflection V_c, crack size a, and time t is needed. Irwin stated that because of creep strain the initial crack lenght a_0 shall be corrected to the effective crack length a_{eff}:

$$a_{eff} = a_0 + \beta_0 r_c \tag{1.41}$$

where r_c is the creep zone size of Eq. (1.31) and β_0 is a scaling factor that in creep regime is equal to $1/3$ if $\vartheta = 90°$. The creep load-line deflection V_c is represented by the difference between the total load-line deflection V_t and the instantaneous deflection V_0 given by the application of the load. It can be expressed as a function of the elastic compliance C_i of the cracked body:

$$V_c = V_t - V_0 = P\frac{dC_i}{da}\beta_0 r_c \tag{1.42}$$

The elastic compliance is then related to the applied stress intensity factor K:

$$\frac{K}{P}BW^{1/2} = F\left(\frac{a}{W}\right) = \left(\frac{1}{2}\frac{d(C_iBE)}{d(a/W)}\right)^{1/2} \tag{1.43}$$

where F is the shape function that depends on the crack size and the cracked body geometry. Equation (1.43) can be rewritten:

$$\frac{dC_i}{da} = \frac{2BK^2}{EP^2}(1-\nu^2) \tag{1.44}$$

By substituting Eq. (1.31) and (1.44) into Eq. (1.42) and differentiating it is possible to define the creep load-line deflection rate $\dot{V}_c$:

$$\dot{V}_c = \frac{4\alpha_i(1-\nu^2)}{E(n-1)}\beta_0 F_{cr}\left(\frac{P}{B}\right)^3 \frac{F^4}{W^2}(EA)^{\frac{2}{n-1}} \cdot t^{-\frac{n-3}{n-1}} \tag{1.45}$$

where

$$\alpha_i = \frac{1}{2\pi}\left(\frac{(n+1)^2}{2n\alpha_n^{n+1}}\right)^{\frac{2}{n-1}} \tag{1.46}$$

and the shape function F is expressed as:

$$F\left(\frac{a}{W}\right) = \frac{K}{P}BW^{1/2} \tag{1.47}$$

Equation (1.45) can be rewritten as:

$$\dot{V}_c = \Phi\left(\frac{a}{W}, t\right)\left(\frac{P}{B}\right)^3 \tag{1.48}$$

where

$$\Phi = \frac{4\alpha_i(1-\nu^2)}{E(n-1)}\beta_0 F_{cr}\frac{F^4}{W}(EA)^{\frac{2}{n-1}} t^{-\frac{n-3}{n-1}} \tag{1.49}$$

Thanks to the load-line deflection rate definition of Eq. (1.48) it is now possible to update Eq. (1.40) in SSC and evaluate the crack tip parameter $(C_t)_{ssc}$ through some simple substitutions:

$$\begin{aligned}
(C_t)_{ssc} &= -\frac{1}{B}\frac{\partial \dot{U}_t}{\partial a} = \frac{1}{Bda}B\left[\int_0^{\dot{V}_c}\left(\frac{\dot{V}_c}{\Phi}\right)^{1/3} d\dot{V}_c - \int_0^{\dot{V}_c}\left(\frac{\dot{V}_c}{\Phi + \frac{\partial \Phi}{\partial a}da}\right)^{1/3} d\dot{V}_c\right] \\
&= \frac{1}{da}\int_0^{\dot{V}_c}\left[1 - \left(1 + \frac{1}{\Phi}\frac{\partial \Phi}{\partial a}da\right)^{-1/3}\right]\left(\frac{\dot{V}_c}{\Phi}\right)^{1/3} d\dot{V}_c \\
&= \frac{1}{da}\int_0^{\dot{V}_c}\frac{1}{3\Phi}\frac{\partial \Phi}{\partial a}da\left(\frac{\dot{V}_c}{\Phi}\right)^{1/3} d\dot{V}_c \\
&= \frac{1}{3\Phi}\frac{\partial \Phi}{\partial a}\frac{3}{4}(\dot{V}_c)^{4/3}\left(\frac{1}{\Phi}\right)^{1/3}
\end{aligned} \tag{1.50}$$

Equation (1.48) can be rearranged as following:

$$\begin{aligned} \tfrac{1}{\Phi} &= \tfrac{1}{\dot{V}_c}\left(\tfrac{P}{B}\right)^3 \\ \left(\tfrac{1}{\Phi}\right)^{1/3} &= \left(\tfrac{1}{\dot{V}_c}\right)^{1/3}\left(\tfrac{P}{B}\right) \end{aligned} \tag{1.51}$$

and replaced in Eq. (1.50):

$$(C_t)_{ssc} = \frac{P\dot{V}_c}{4B}\frac{1}{\Phi}\frac{\partial\Phi}{\partial a} \tag{1.52}$$

The term $1/\Phi \cdot \partial\Phi/\partial a$ is calculated by accounting that:

$$\Phi = \Phi\left(\frac{a}{W}\right) \rightarrow \frac{\partial\Phi}{\partial a} = \frac{1}{W}\frac{\partial\Phi}{\partial\left(\frac{a}{W}\right)} \tag{1.53}$$

Thus it is possible to evaluate $1/\Phi \cdot \partial\Phi/\partial a$:

$$\frac{\partial\Phi}{\partial a} = \frac{4}{W}\frac{F'}{F} \tag{1.54}$$

with $F' = dF/d(a/W)$, and substitute it to Eq. (1.52):

$$(C_t)_{ssc} = \frac{P\dot{V}_c}{BW}\frac{F'}{F} \tag{1.55}$$

It is now possible to express the crack tip parameter $(C_t)_{ssc}$ as a function of the creep zone size by deriving and substituting Eq. (1.42) into Eq. (1.55)

$$(C_t)_{ssc} = \frac{P^2}{BW}\frac{F'}{F}\frac{dC_i}{da}\beta_0\dot{r}_c = \frac{2K^2(1-\nu^2)}{EW}\beta_0\frac{F'}{F}\dot{r}_c \tag{1.56}$$

or by relating it to Eq. (1.45):

$$\begin{aligned} (C_t)_{ssc} &= \tfrac{P}{BW}\tfrac{F'}{F}\tfrac{4\alpha_i(1-\nu^2)}{E(n-1)}\beta_0 F_{cr}\left(\tfrac{P}{B}\right)^3\tfrac{F^4}{W^2}(EA)^{\frac{2}{n-1}}t^{-\frac{n-3}{n-1}} \\ &= \tfrac{4\alpha_i(1-\nu^2)}{E(n-1)}\beta_0 F_{cr}\tfrac{K^4}{W}(EA)^{\frac{2}{n-1}}\tfrac{F'}{F}t^{-\frac{n-3}{n-1}} \end{aligned} \tag{1.57}$$

Equation (1.56) relates the $(C_t)_{ssc}$ parameter to the creep zone size evolution $\dot{r}_c$ validating its use as a crack tip parameter. Equation (1.57) instead suggests that $(C_t)_{ssc}$ can be determined for every specimen geometry for which a stress intensity factor K is defined. The $(C_t)_{ssc}$ parameter is valid just for SSC regime although Bassani et al. [8] and Saxena [48] extended it to EC conditions. In this case the crack tip parameter is C_t and at high times t tends to C^*:

$$C_t = (C_t)_{ssc} + C^* \tag{1.58}$$

By recognizing that:

$$\dot{V}_c \approx \dot{V}_{ssc} + \dot{V}_{ss} \tag{1.59}$$

and that the generic expression of C^* based on Eq. (1.14) is updated depending on the term η that differs for every geometry:

$$C^* = \frac{P\dot{V}_{ss}}{BW}\eta\left(\frac{a}{W}, n\right) \tag{1.60}$$

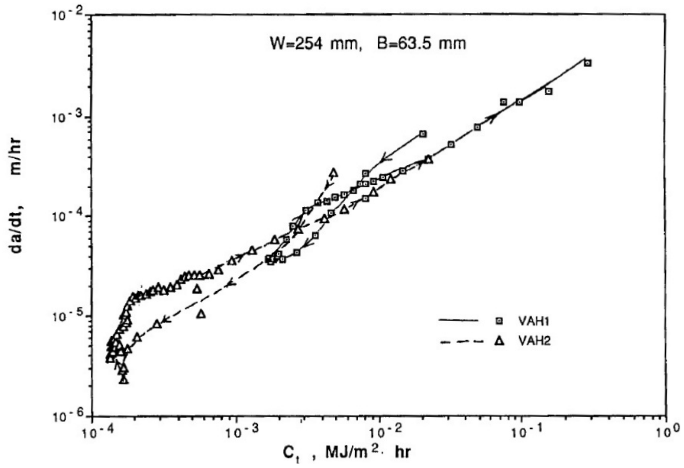

Figure 1.13: *Crack propagation rate as a function of the C_t parameter for large C(T) specimens [3].*

Saxena [47] rewrote Eq. (1.58)

$$C_t = (C_t)_{ssc} + C^* = \frac{P\dot{V}_c}{BW}\frac{F'}{F} - C^*\left(\frac{F'}{\eta F} - 1\right) \tag{1.61}$$

This last expression of C_t covers every range of creep conditions from SSC to EC as demonstrated by Saxena et al. [3] that experimentally calculated the C_t parameter in large size C(T) specimens. Using large specimens increases the crack propagation that happens during SSC and EC conditions. Figure 1.13 shows the trend of crack propagation rate that slows down at the beginning of the tests in full SSC conditions and starts to increase when approaching extensive creep conditions.

The C_t parameter is able to estimate the trend of crack propagation rates in both conditions validating once again its use as a crack tip parameter for CCG regime able to correlate the creep crack growth rate in SSC and TC regimes, as well as in EC regime according to:

$$\frac{da}{dt} = D'C_t^{\phi'} \tag{1.62}$$

with D' and ϕ' constants of the material.

1.2 Creep-Fatigue Crack Growth

Until here the most diffused CCG parameters have been presented and analyzed demonstrating their correlation to the crack growth rates for known geometries, like testing specimens, as well as complex geometries, like components. These parameters are able to estimate the residual life of a component that is subject to high temperature and a sustained load for a long period of time. However in power generation industry, dispatching priorities demands for higher flexibility that, in plant components context results in critical operating conditions. Repetitive start-ups cause a cyclic load, introducing a fatigue damage which cannot be described by the crack tip parameters of Sec. 1.1. In fact under these conditions each cycle consists in a rise phase, where the load is applied, followed by an hold phase (hold time t_h), with sustained load, and a decay phase, where the load is brought to its minimum. The crack tip is characterized by elastic, plastic, creep, and cyclic plastic zones (Fig. 1.14) that change with time at every fatigue cycle causing creep-fatigue crack growth (CFCG). The plastic zone is expected to grow together with crack propagation due to stress increasing. The creep zone is also expected to increase together with time. The cyclic plastic zone is instead expected to stabilize, after an amount of fatigue cycles. The size and the evolution of these zones depends on the material creep and cyclic plasticity resistance. It might be worth noting

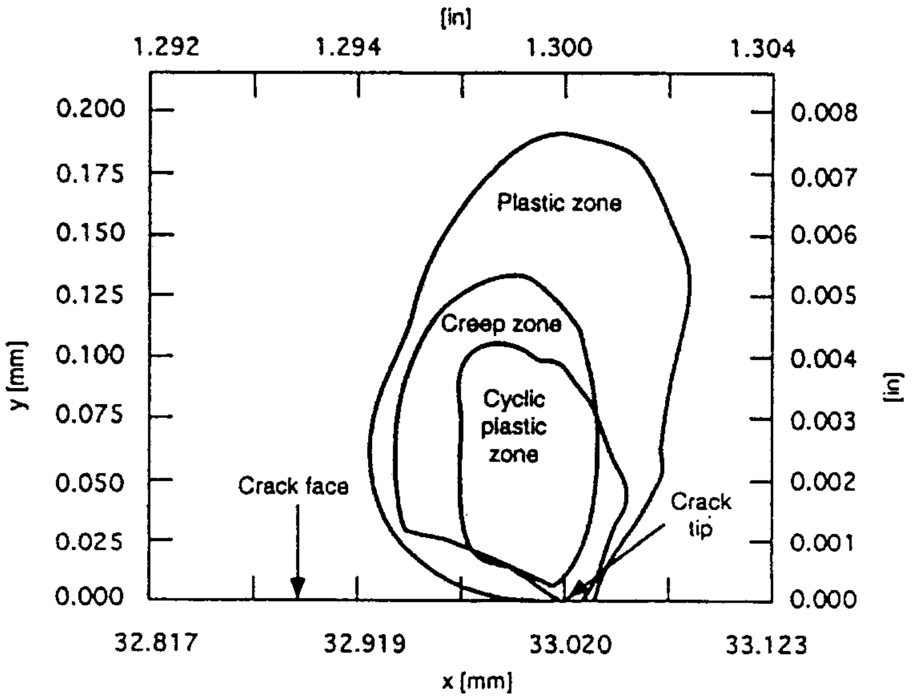

Figure 1.14: *Numerical estimation of the elastic, plastic, creep, and cyclic plastic zones during the third cycle of a creep-fatigue test [50].*

that during a CFCG test three main situations may verify:

- The creep strain is not reversed by the fatigue cycle. This situation corresponds to Fig. 1.15a) where the creep zone is more relevant than the cyclic plastic zone. At the beginning of a new hold cycle the C_t parameter starts from the value reached at the end of the previous hold cycle demonstrating that creep strain is not reversed by the fatigue cycle. This is typical of materials with high cyclic yield strength or tests at very long hold times t_h.

- The creep strain in completely reversed by the fatigue cycle. This situation corresponds to Fig. 1.15b) where the cyclic plastic zone is dominant with respect to the creep zone. In this case at the beginning of each new hold cycle the C_t parameter starts from the value that was observed during the beginning of the first hold cycle showing that fatigue cycles are reversing the creep strain.
- Creep zone and cyclic plastic zone are comparable and therefore creep strain may be partially reversed during the unloading-reloading cycle. As expected, most of the materials operate under this condition.

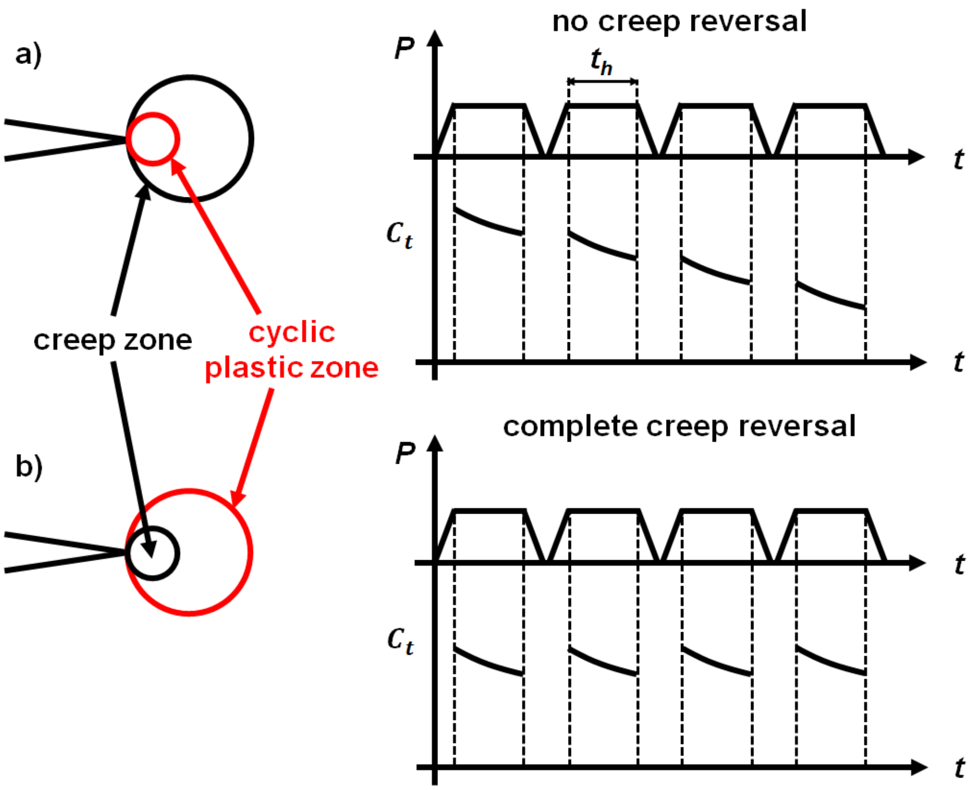

Figure 1.15: *Schematic diagram of the interactions between the creep zone and the cyclic plastic zone in case of no creep reversal a) and complete creep reversal b)*

1.2.1 Crack tip parameter in CFCG regime

To characterize the crack growth in the creep-fatigue regime, Saxena and Gieseke [4] suggested to use an average value of the crack tip parameter C_t during a N^{th} fatigue cycle defining the $(C_t)_{avg}$ parameter:

$$(C_t)_{avg} = \frac{1}{t_h} \int_{t(N)}^{t(N)+t_h} C_t dt \tag{1.63}$$

that accounts for the relevant phenomenon, that is the interaction between the creep damage accumulation at the crack tip and the subsequent effect of the fatigue cycle. Equation (1.63) can be rewritten, for the two ideal behaviors of the material named no creep reversal and complete creep reversal, as Eq. (1.64a and b) respectively:

$$(C_t)_{avg} = \frac{1}{t_h}\int_{(N-1)t_h}^{N(t_h)} C_t \quad dt \tag{1.64a}$$

$$(C_t)_{avg} = \frac{1}{t_h}\int_{0}^{t_h} C_t \quad dt \tag{1.64b}$$

$(C_t)_{avg}$ estimation in specimens

Yoon et al. [36] adapted the C_t definition of Eq. (1.61) to calculate $(C_t)_{avg}$ in C(T) specimens:

$$(C_t)_{avg} = \frac{\Delta P \Delta V_c}{BWt_h}\frac{F'}{F} - C^*\left(\frac{F'}{F\eta} - 1\right) \tag{1.65}$$

where ΔP and ΔV_c are the load and load-line deflection range during the cycle.
Thanks to Eq. (1.65) the $(C_t)_{avg}$ crack tip parameter can be easily determined through the load-line deflection in experimental creep-fatigue tests, providing a creep-fatigue crack growth rate for the tested material as:

$$\left(\frac{da}{dt}\right)_{avg} = D''(C_t)_{avg}^{\phi''} \tag{1.66}$$

where D'' and ϕ'' are material constants.

$(C_t)_{avg}$ analytical estimation

Under the hypotheses of instantaneous cyclic plasticity and secondary creep behavior and in plane strain conditions it is also possible an analytical evaluation of the $(C_t)_{avg}$ parameter for both conditions of complete creep reversal and no creep reversal. For complete creep reversal, Saxena and Gieseke [4] combined Eq. (1.64) with the C_t definition of Eq. (1.57) and (1.58):

$$\begin{aligned}(C_t)_{avg} &= \tfrac{1}{t_h}\int_0^{t_h}\left(\left[\tfrac{4\alpha_i(1-\nu^2)}{E(n-1)}\beta_0 F_{cr}\tfrac{\Delta K^4}{W}(EA)^{\frac{2}{n-1}}\left(\tfrac{F'}{F}\right)t^{-\frac{n-3}{n-1}}\right] + C^*\right)dt \\ &= \tfrac{1}{t_h}\tfrac{4\alpha_i(1-\nu^2)}{E}\beta_0 F_{cr}\tfrac{\Delta K^4}{W}(EA)^{\frac{2}{n-1}}\left(\tfrac{F'}{F}\right)\left[\int_0^{t_h}\tfrac{1}{n-1}t^{-\frac{n-3}{n-1}}dt\right] + C^* \\ &= \tfrac{1}{t_h}\tfrac{4\alpha_i(1-\nu^2)}{E}\beta_0 F_{cr}\tfrac{\Delta K^4}{W}(EA)^{\frac{2}{n-1}}\left(\tfrac{F'}{F}\right)\left|\tfrac{1}{n-1}\tfrac{t^{1-\frac{n-3}{n-1}}}{1-\frac{n-3}{n-1}}\right|_0^{t_h} + C^* \\ &= \tfrac{1}{t_h}\tfrac{4\alpha_i(1-\nu^2)}{E}\beta_0 F_{cr}\tfrac{\Delta K^4}{W}(EA)^{\frac{2}{n-1}}\left(\tfrac{F'}{F}\right)\tfrac{1}{2}t_h t_h^{-\frac{n-3}{n-1}} + C^* \\ &= \tfrac{2\alpha_i\beta_0(1-\nu^2)}{E}F_{cr}\tfrac{\Delta K^4}{W}\tfrac{F'}{F}(EA)^{\frac{2}{n-1}}t_h^{-\frac{n-3}{n-1}} + C^*\end{aligned} \tag{1.67}$$

where ΔK is the stress intensity factor range between a cycle.
When the fatigue cycle is not enough to reverse the creep strain $(C_t)_{avg}$ can be evaluated

with the same expression of Eq. (1.57) and (1.58) with the only difference that the time t is replaced by the effective time of permanence at the maximum load Nt_h:

$$(C_t)_{avg} = \frac{4\alpha_i(1-\nu^2)}{E(n-1)}\beta_0 F_{cr}\frac{K^4}{W}(EA)^{\frac{2}{n-1}}\left(\frac{F'}{F}\right)(Nt_h)^{-\frac{n-3}{n-1}} + C^* \tag{1.68}$$

In his PhD thesis, Grover [27] found a correlation between the quantity of reversed creep and the creep reversal parameter C_R defined as the ratio between the load-line deflection variation calculated at the end of one hold cycle and the beginning of the next hold cycle ΔV_r, and the the load-line deflection measured during hold time ΔV_c with reference to Fig. 1.16:

$$C_R = \frac{\Delta V_r}{\Delta V_c} \tag{1.69}$$

If $C_R = 1$, $\Delta V_r = \Delta V_c$ representing the condition of complete creep reversal while if

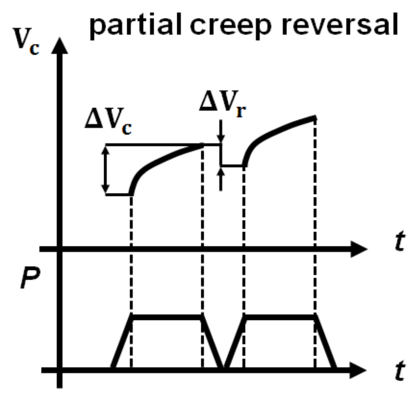

Figure 1.16: *Schematic diagram of the creep reversal parameter C_R.*

$C_R = 0$, $\Delta V_r = 0$ representing the condition of no creep reversal. Since with the creep reversal parameter an intermediate situation between Eq. (1.67) and (1.68) is analyzed, $(C_t)_{avg}$ was redefined according to:

$$(C_t)_{avg} = [1 - C_R]\frac{1}{t_h}\int_{(N-1)t_h}^{Nt_h} C_t dt + C_R\frac{1}{t_h}\int_0^{t_h} C_t dt \tag{1.70}$$

That if substituted to Eq. (1.57) and (1.58) becomes:

$$\begin{aligned}(C_t)_{avg} = {} & \frac{2\alpha_i\beta_0(1-\nu^2)}{EW}F_{cr}\Delta K^4\frac{F'}{F}(EA)^{\frac{2}{n-1}} \\ & \left[C_R + \frac{2(1-C_R)N^{-\frac{n-3}{n-1}}}{n-1}\right]t_h^{-\frac{n-3}{n-1}} + C^*\end{aligned} \tag{1.71}$$

The creep reversal parameter C_R can also be determined analytically by observing that the load-line deflection variations ΔV_r and ΔV_c are related to the size of the cyclic plastic zone r_{cp} and the creep zone r_c respectively. C_R can now be expressed as:

$$C_R = P_R\frac{r_{cp}}{r_c} \tag{1.72}$$

where r_c is defined according to Adefris [40] Eq. (1.33), P_R is the creep reversal constant that can be fitted from experimental values of C_R and r_{cp} is defined as:

$$r_{cp} = \frac{1}{\xi_{cp}} \frac{m_{cp}+1}{m_{cp}-1} \left(\frac{(1-R)K}{2\sigma_{0cp}} \right)^2 \tag{1.73}$$

where m_{cp} is the exponent of the cyclic plastic law, σ_{0cp} is the cyclic plastic yield strength and ξ_{cp} is a coefficient that has a value of 2π in plane stress and 6ϕ in plane strain. By combining Eq. (1.72) with Eq. (1.33) and (1.73) and by observing that $\sigma_{0cp}/0.002 = E$, C_R can be rewritten as:

$$C_R = P_R \frac{1}{\xi_{cp}\hat{r}_c} \frac{m_{cp}+1}{m_{cp}-1} \frac{.002^{\frac{n+1}{n}} E}{[(n+1)ANt_h]^{1/n}} \frac{I_n(1-R)^2}{4\sigma_{0cp}^2(1-\nu^2)} \tag{1.74}$$

The analytical calculation of C_R joint with the analytical calculation of $(C_t)_{avg}$ parameter (Eq. (1.71)) allows the application of the experimental creep-fatigue correlation given in Eq. (1.66) to assess CFCG in components.

1.3 Creep-Fatigue Crack Growth Rate for Components

The early approaches to model CFCG in full-scale components were mainly based on the simple superposition of the creep damage, characterized by the C^* parameter, and the fatigue damage [32]:

$$\frac{da}{dN} = \left(\frac{da}{dN} \right)_{cycle} + t_h D (C^*)^{\phi} \tag{1.75}$$

where $(da/dN)_{cycle}$ is the crack propagation associated to fatigue, that is defined according to the Paris-Erdogan law [41]:

$$\left(\frac{da}{dN} \right)_{cycle} = C \Delta K^m \tag{1.76}$$

with C and m material constants obtained from FCG tests at constant load. The limitation of this approach is given by the fact that the C^* parameter is a stabilized value of the $C(t)$ integral, under extensive creep conditions, when the creep zone size is dominant with respect to the elastic and plastic zones resulting in a lack of interaction effects between the creep and fatigue damages. However, as previously discussed, during short hold times, this particular condition may not occur. To overcome this issue Viswanathan [52] by introducing a non-linear power law dependence of crack growth rate on hold time:

$$\frac{da}{dN} = \left(\frac{da}{dN} \right)_{cycle} + D_v K^{2\phi} t_h^{1-\phi} + D (C^*)^{\phi} t_h \tag{1.77}$$

where D_v is a material constant obtained from experimental CFCG tests. Although this approach is expected to be more accurate than the one of Eq. (1.75), it does include any contribute that accounts for the evolution of the creep zone size.
To address this problem, a state-of-the-art approach to predict CFCG rate in components provides a damage partitioning analysis where the crack propagation per cycle is split between fatigue and time-dependent damage according to Eq. (1.78):

$$\frac{da}{dN} = \left(\frac{da}{dN}\right)_{cycle} + \left(\frac{da}{dN}\right)_{time} \tag{1.78}$$

In this Equation, the crack propagation due to CCG is modeled instead through the $(C_t)_{avg}$ parameter that thanks to the power law of Eq. (1.66) is able to describe the average crack propagation rate $(da/dt)_{avg}$ during a cycle. Equation (1.78) can be rewritten by integrating the creep contribution on the hold time t_h.

$$\frac{da}{dN} = C\Delta K^m + \int_0^{t_h} D'' \left[(C_t)_{avg}\right]^{\phi''} dt \tag{1.79}$$

With this equation the crack propagation per cycle is expressed as a superposition between a pure fatigue contribution and an additional contribution that includes the effects of creep and creep-fatigue interaction. The interaction between creep and fatigue can be modeled under the hypotheses of complete and no creep reversal or, as will be proposed in Ch. 3, under the hypothesis of partial creep reversal by means of the creep reversal parameter C_R experimentally determined from CFCG tests on C(T) specimens and used for $(C_t)_{avg}$ calculation.

1.4 Summary

This Chapter deals with a comprehensive review of the crack tip parameters that describe CCG and CFCG in testing specimens and components. After a brief introduction about the creep damage in cracked components, the EPFM concept of J integral is extended to account for time dependent creep strains defining the new integral C^* valid for extensive creep conditions. The C^* integral is path independent, has a strain energy interpretation and is related to the HRR stress fields. It is easily estimated with a semi-empirical method that analyze the load-line deflection records of testing specimens. It can also be determined for complex geometries by means of numerical simulations and has been widely accepted as a crack tip parameter to correlate the creep crack growth rate in EC conditions.
In SSC and TC conditions, Bassani and McClintock [7] introduced the $C(t)$ integral with an analogous expression of C^* evaluated at a contour strictly close to the crack tip but, unfortunately, it can not be estimated at the load-line and it can not be used to

correlate creep crack growth rates in SSC conditions. Saxena [49], solved this issue by defining a new crack tip parameter C_t that, by definition, tends to C^* in EC conditions and, in addition to this, is measurable at the load-line also in SSC and TC conditions. With this prospective, the crack tip parameter C_t is able to correlate creep crack growth rates in every creep conditions. In case of complex geometries, an analytical definition of the C_t is given by relating the load-line deflection rate $\dot{V}_c$ to the rate of expansion of the creep zone radius r_c.

In CFCG conditions at sufficient short hold times, the steady-state creep may never be reached. Since the creep zone size is in continuous competition with the cyclic plastic zone, by integrating the C_t parameter during the hold time t_h, it is possible to determine a new crack tip parameter $(C_t)_{avg}$ that governs the average crack propagation rate during the fatigue cycles. $(C_t)_{avg}$ accounts for the interaction given by the creep damage accumulation at the crack tip and the fatigue damage, correlating the average crack propagation rates. As per C_t parameter, also $(C_t)_{avg}$ can be analytically expressed under the hypotheses of complete or no reverse of the creep strains due to cyclic plasticity. In case of partial reverse of creep strains, CFCG tests allow the estimation of a creep reversal parameter C_R defined by Grover [27] that accounts for the interactions between the creep and the cyclic plastic zones leading to a new analytical estimation of the $(C_t)_{avg}$ based on this material property. Since the analytical calculation of the creep reversal parameter C_R allows the estimation of a more accurate correlation between the average crack growth rate and the $(C_t)_{avg}$ parameter, the formulations to assess CFCG in components have been also reported.

CHAPTER 2

Material Properties and Experimental Work

As discussed in Ch. 1 during CCG and CFCG regime, the crack tip parameters are strictly dependent on the elastic, plastic, creep, and cyclic plastic zones and their evolution with time.
This Chapter starts with a description of the P91 steel investigated material, and its elastic-plastic and creep properties. Afterwards, the extended experimental campaign of CCG and CFCG tests performed to investigate the crack propagation rate correlation with crack tip parameters in creep and creep-fatigue conditions, is reported.
Since the state-of-the-art approach to model CFCG in components is given by superposition of fatigue and time dependent damage, FCG tests were necessary to identify the Paris-Erdogan law coefficients that describe high temperature crack growth associated to fatigue only.
This chapter ends with the application and comparison of different methods to evaluate the J_{IC} parameter in high temperature fracture toughness tests. These tests have been necessary to investigate the resistance of P91 at high temperature when the load level is high enough to cause plastic collapse prior to creep damage.
All the tests presented in this work are based on different specimen geometries that were directly extracted from an actual pipe reserved for the occasion.

2.1 P91 grade steel

The material analyzed in this work is a single batch of modified P91 grade steel manufactured by Tenaris for applications at the maximum temperature of 600 °C. P91 is a standard material for power industry due to the combination of its good mechanical and creep resistance properties that make it a good candidate in power generation applications, where high temperatures and stresses represent a critical operating condition. Another important aspect of P91 is that its resistance characteristics are maintained over time because of a high oxidation temperature limit that allows the design of lower thickness components. The typical chemical composition of a P91 steel is reported in Tab. 2.1. Its high Chromium content (between 8 and 9.5 %) increases the resistance

Table 2.1: *P91 standard chemical composition in % [1].*

C	Si	Mn	P	S	Al	Cr	Mo	Ni	V	N	others
0.08-0.12	0.2-0.5	0.3-0.6	$\leq$0.02	$\leq$0.01	$\leq$0.04	8-9.5	0.85-1.05	$\leq$0.4	0.18-0.25	0.03-0.07	Nb 0.06-0.1

to static loads and oxidation while the presence of Molybdenum increases the creep resistance. A small percentage of Nickel and Manganese is included in the alloy to improve its hardenability. Very important in P91 production is the thermal treatments of normalizing and tempering that significantly affect the microstructure that is mainly characterized by martensite. The analyzed material is subject to a specific thermal treatment that was designed by Tenaris in order to increase the creep resistance without compromising its high temperature elastic-plastic properties. The heat treatment, and the resulting microstructure, are not reported in the present thesis for confidentiality agreement.

High temperature tensile tests at 600 °C have been performed by Tenaris according to the applicable ASTM E8 standard [20]. The geometry used in this test is shown in Fig. 2.1. The gauge lenght is 50 mm and the diameter is 10 mm. The stress-strain curve is reported in Fig. 2.2 together with the elastic modulus E and the yield strength σ_0. The viscous behavior was characterized by means of uniaxial creep tests performed at 600 °C by Tenaris according to the ASTM E139 standard [16], on the same batch of material used in this thesis for the experimental campaign. The specimen geometry is a cylindrical specimen, similar to the one adopted for tensile tests (2.1) with the exception of a couple of ribs for extensometer accomodation. The matrix of the uniaxial creep tests is reported in Tab. 2.2 together with the rupture times t_R and the minimum creep strain rates $\dot{\varepsilon}_{ss}$. Uniaxial creep curves at high and low stresses are shown in Fig. 2.3 (a) and (b) respectively. From the creep strain rate curves of Fig. 2.4 (a) and (b) it was possible to analyze the minimum creep strain rate during steady-state $\dot{\varepsilon}_{ss}$ as a func-

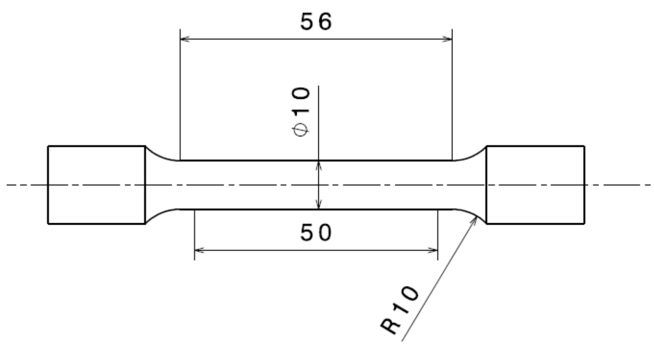

Figure 2.1: *Schematic draw of the cylindrical specimen used in tensile tests.*

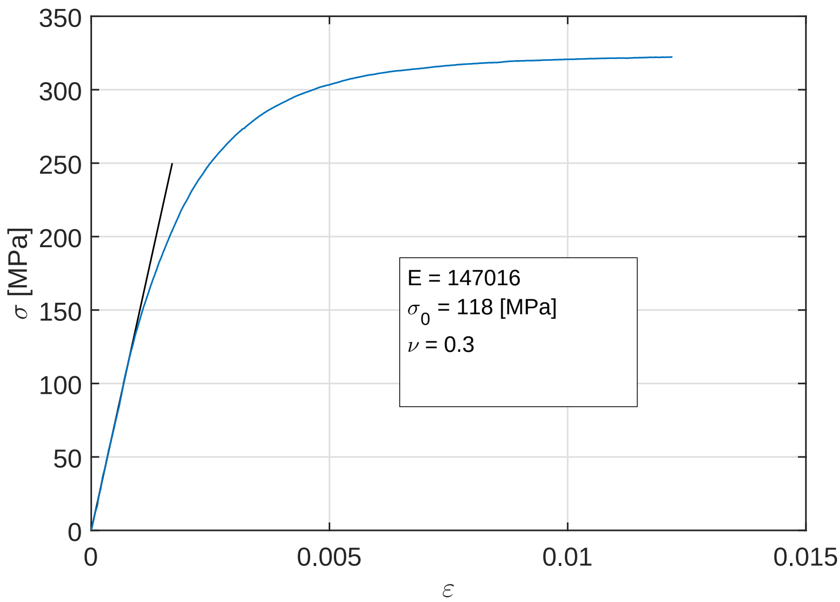

Figure 2.2: *Stress vs. strain curve for P91 at 600 °C.*

Table 2.2: *Creep test matrix of P91 at 600 °C.*

σ [MPa]	t_R [h]	$\dot{\varepsilon}_{ss}$ [1/h]
90	104100	1.727E-7
100	66410	3.819E-7
110	38500	5.457E-7
120	18380	1.132E-6
130	5238	4.946E-6
160	635	6.264E-5

tion of the applied stress σ. The creep tests of Fig. 2.4 (a) and (b) has been combined with an additional dataset provided by Tenaris, related to different batches of the same P91 material, in order to fit the Norton law of Eq. (1.1) by means of a least squares minimization algorithm (Fig. 2.5). The pairs of A and n constants determined at low

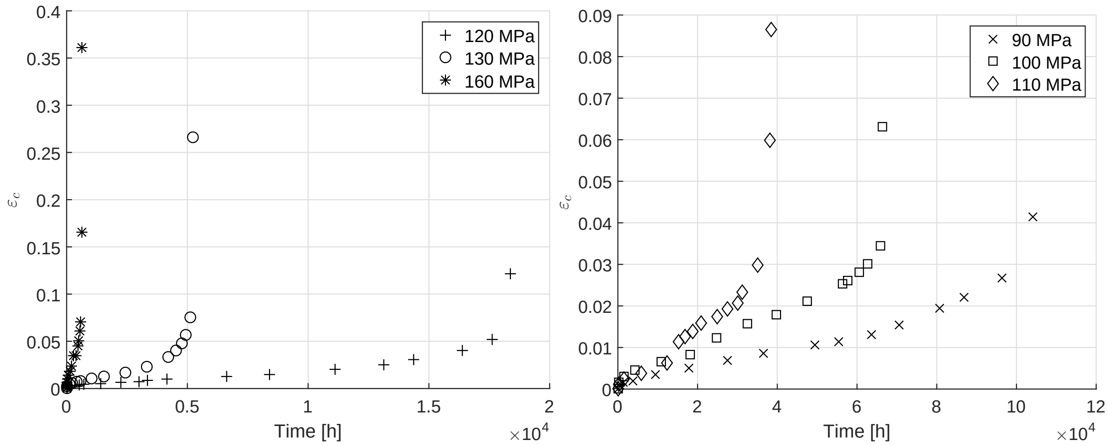

(a) *High stresses.* **(b)** *Low stresses.*

Figure 2.3: *Uniaxial creep curves of P91 at 600 °C.*

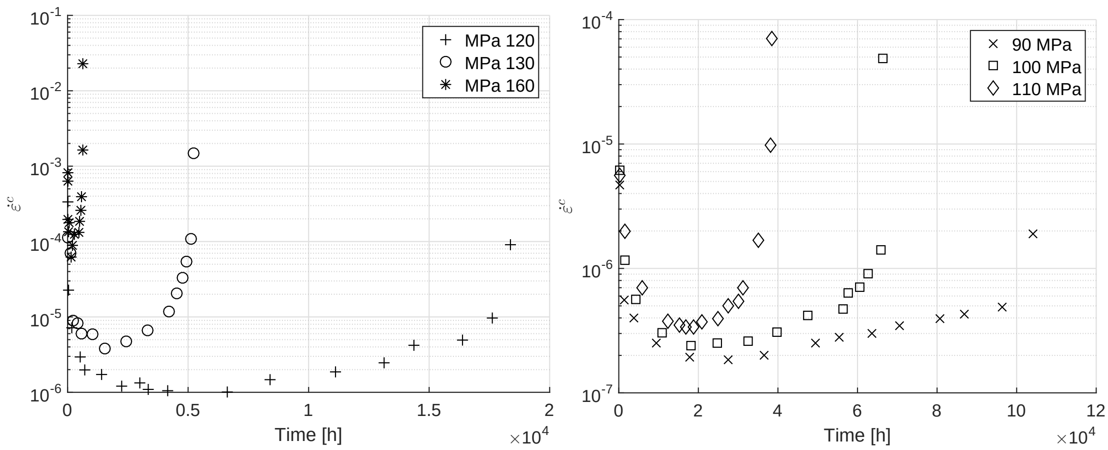

(a) *High stresses.* **(b)** *Low stresses.*

Figure 2.4: *Creep strain rate evolution with time of P91 at 600 °C.*

Table 2.3: *Material constants for P91 at 600 °C.*

	A $[MPa^{-n}h^{-1}]$	n
$\sigma < 121MPa$	2.71e-014	3.69
$\sigma \geq 121MPa$	2.18e-039	15.71

and high stresses are reported in Tab. 2.3. The creep resistance in terms of rupture time for P91 may be defined according to the Larson-Miller parameter P_{LM}:

$$P_{LM} = T \cdot (C_0 + \log t_R) \tag{2.1}$$

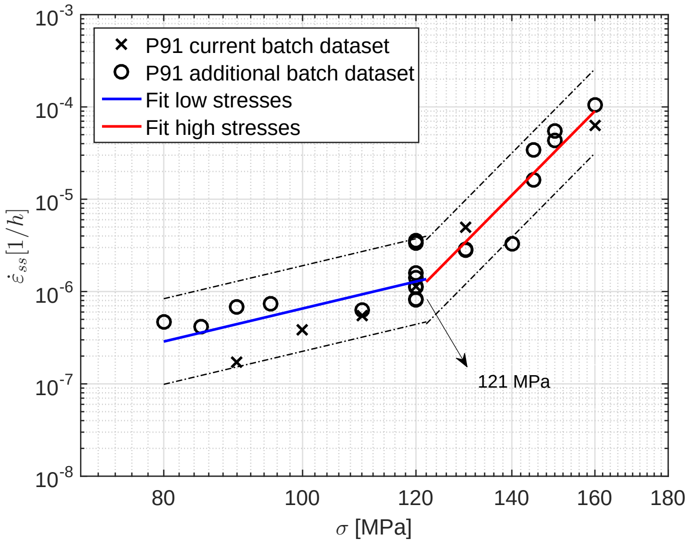

Figure 2.5: *Norton law of P91 at 600° C.*

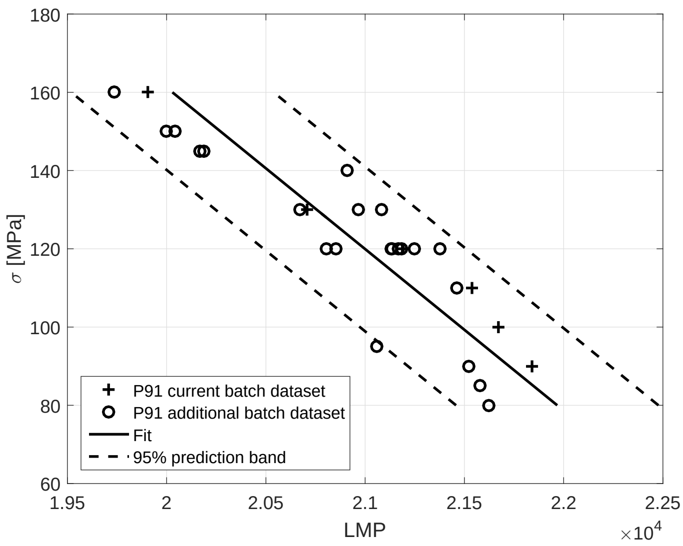

Figure 2.6: *Larson Miller Parameter.*

where T is the temperature expressed in $^{\circ}K$, t_R is the rupture time of creep tests in hours and C_0 is a constant ($C_0 = 20$ for standard materials). If the nominal stress of the creep tests is plotted in logarithmic scale versus the obtained Larson-Miller parameter a linear trend can be observed as demonstrated in Fig. 2.6 for the same tests of Fig. 2.5. The Norton law and the relationship between Larson-Miller parameter and stress will be fundamental to transpose the P91 data, from specimen to component geometry in the crack assessment strategies for pressurized pipes presented in Ch. 3, but to account for the presence of defects, an extensive experimental campaign including: CCG, CFCG, FCG, and J_{IC} tests has been performed in the framework of the present thesis and reported in the following sections.

2.2 CCG tests [22]

Creep crack growth tests was the first series of tests performed to investigate the behavior of the P91 material in presence of defect. The aims of these tests is:

- to investigate the initiation of the creep crack propagation and the crack propagation rate as a function of the nominal intensity factor at the beginning of the test;
- to obtain experimental correlation between the crack propagation rate and the crack tip parameters for extensive creep (Eq. (1.14)) and for small-scale and transition creep (Eq. (1.58)). This relationship is intrinsic of the material and does not depend on the analyzed geometry, becoming fundamental in the crack propagation assessment of pipe components according to both the classical approach of BS 7910 [12] and the concept of C_t parameter (1.1.2).

All the CCG tests reported in this work, have been performed at 600 °C according to the applicable ASTM E1457-15 standard [6]. The compact tension C(T) specimen geometry of Fig. 2.7 was designed to easily accommodate the leads of the direct current potential drop (PD) measurement system that was used, to determine the crack propagation rates during the tests.

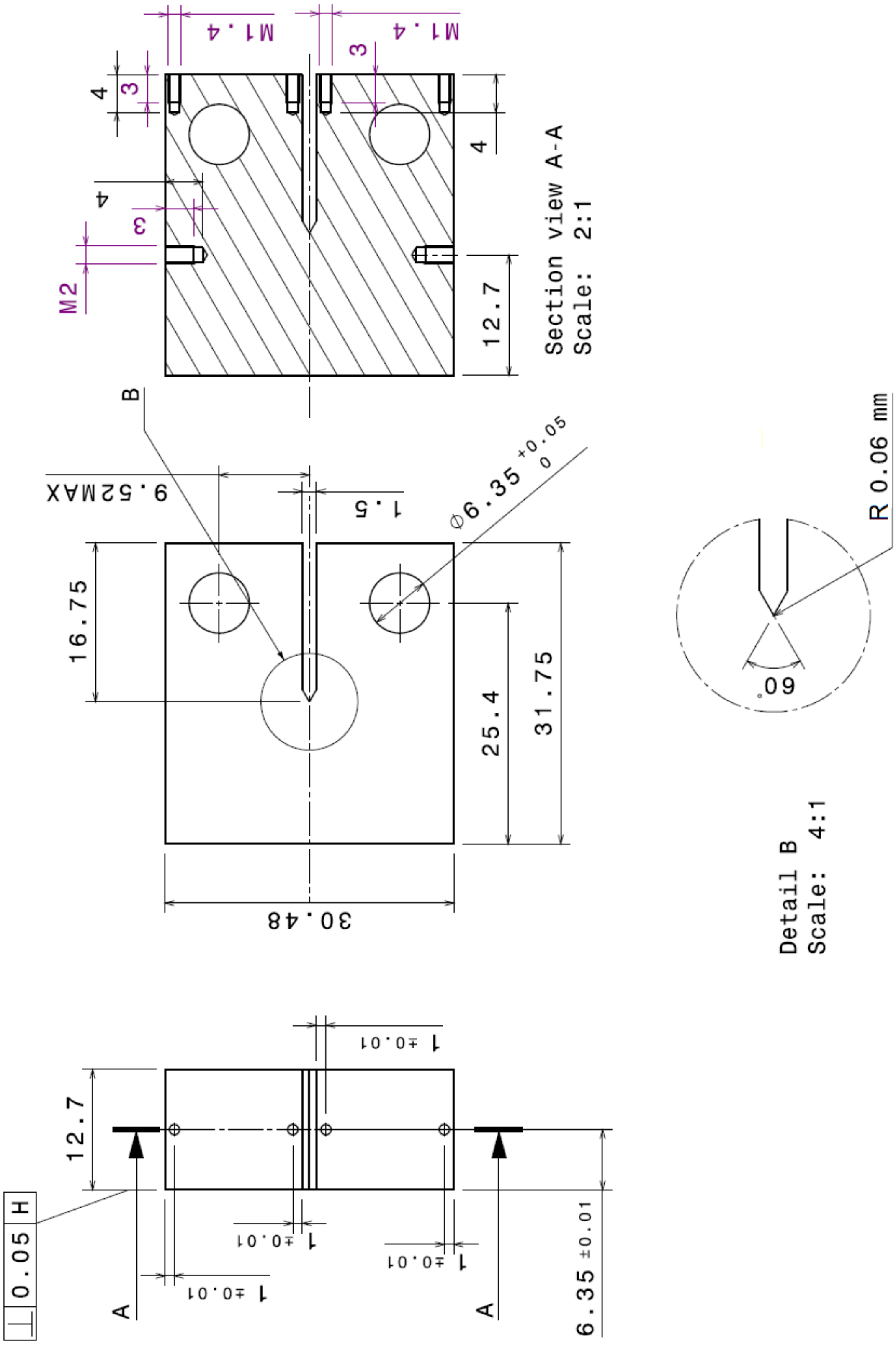

Figure 2.7: *C(T) specimen geometry with potential drop measurement arrangement.*

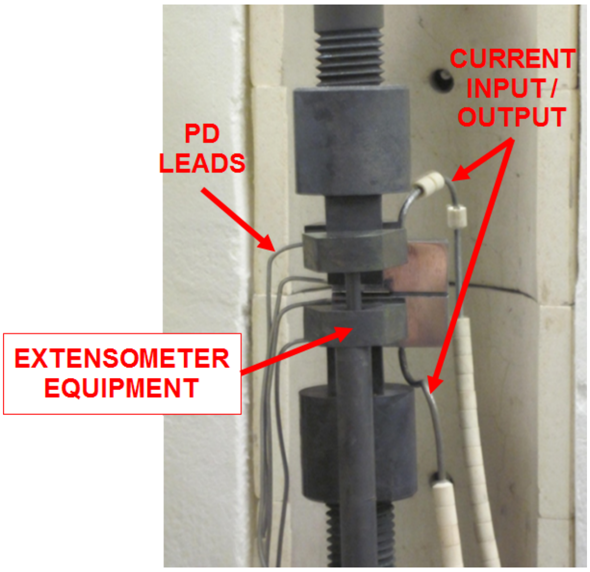

Figure 2.8: *CCG tests setup.*

2.2.1 CCG Experimental Tests

All CCG tests were performed on the creep testing machine SATEC JE 1016 that features a maximum capacity of 12000 N. The load is applied by means dead weights through a leverage system. The C(T) specimen (Fig. 2.8) is enclosed in a three controlled zones furnace SATEC SF-17 2230 that can reach a maximum temperature of 1200 $^{\circ}C$. The furnace control is able to guarantee a temperature fluctuation of $\pm 2^{\circ}C$ with respect to the nominal test temperature. This range is constantly monitored through a thermocouple located in proximity of the specimen notch. The C(T) geometry of Fig. 2.7 is designed to allows PD crack size measurements. As shown in Fig. 2.8 two holes in the upper and lower surface hold the leads that distribute current to the specimen. Four holes located in the front face of the C(T) specimen hold the leads that measure the potential drop in two different zones, remote and local with respect to the crack tip. A PD calibration curve for this specific geometry was found in the work of Belloni et al. [9]. The specimen is fixed to the testing machine by two pin holes that allow rotations. At these points, the load-line displacement was measured by means of an extensometer properly connected by a dedicated equipment.

A typical creep crack life can be divided in two main parts:

- initiation of crack propagation (CCI) and
- creep crack growth (CCG)

CCI comprehends the amount of time needed after the application of the load, to reach a creep crack growth of $\Delta a_c = 0.2$ mm. During CCI the specimen is in SSC and TC

conditions. The value of 0.2 mm is defined according to the size of the tested C(T) specimens (in this case $B = 1/2''$). The time needed to reach 0.2 mm of creep crack, is called initiation time t_i and is used in the components assessment codes to identify CCI. In order to produce reliable CCI times, a sharp notch is needed. For this reason, each specimen was fatigue pre-cracked at room temperature on a servo-hydraulic machine with a load ratio $R = 0.1$ and a maximum load that produces a lower stress intensity factor than the one that is going to be tested. After a fatigue pre-crack of 1.7 mm was reached, side grooves were machined, in order to guarantee a straight crack front in the crack size measurements post test. With this procedure the specimen thickness B was reduced of 20% to the net section thickness $B_n = 20\%B \approx 10.1$ mm. The specimen is now ready for testing.
After the test temperature is reached and maintained for 1 h, the initial stress intensity factor K_0 is applied through dead weights. During the test, temperature on the specimen, load-line displacement and PD measurements are acquired simultaneously thanks to a dedicated Labview program. In order to achieve reliable crack estimations, the PD technique was not based on single readings but on the average of multiple readings when the current is circulating in the specimen. Each average reading is always compared in relation with the average of multiple readings without active current in the specimen.
A CCG test ends when the crack propagation reaches 0.7 a/W or when crack propagation and load-line displacement measurements show that the beginning of the tertiary stage of crack growth is reached and the specimen is about to fail. At the end of the test the specimen is brittle broken in liquid nitrogen to avoid any further plastic deformation. As per ASTM E1457-15 standard [6], the CCG test is valid only after the initial crack front a_0 and the final creep crack propagation Δa_c front, evaluated at nine equally spaced points, pass several requirements. Starting from a valid CCG test, it is possible to estimate initiation time and the steady-state crack tip parameter C^* based on the experimental data, in order to find its relationship with the crack propagation rate (da/dt) (Fig. 2.9). Table 2.4 summarizes all the test data performed on P91 at 600 $^{\circ}C$ including the value of the nominal stress intensity factor at the beginning of the test (K_0), the value of the crack length at the beginning of the test (a_0) and the main results of each test: the transition time t_T, the time for CCI t_i, the creep crack propagation at the end of the test Δa_c, and the time to rupture t_R.

2.2.2 CCG Test Results

The results expressed in terms of crack propagation as a function of time are shown in Fig. 2.10 and in terms of load-line displacement in Fig 2.11. As expected, tests

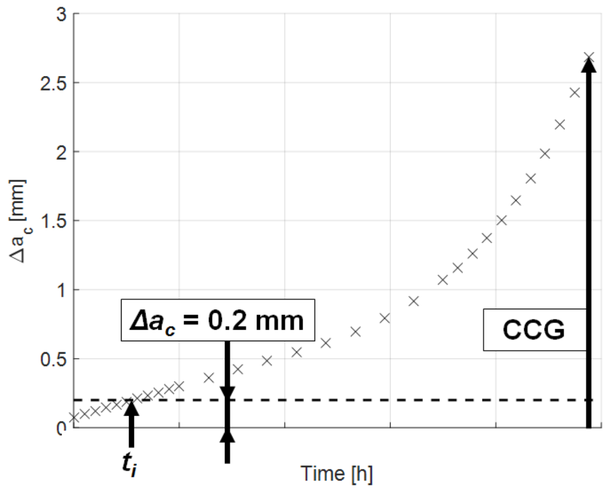

Figure 2.9: *Schematic representation of the initiation data for specimen P91-10.*

Table 2.4: *CCG test data matrix.*

Specimen	P [N]	K_0 [MPa $\sqrt{\text{m}}$]	a_0 [mm]	t_T [h]	t_i [h]	Δa_c [mm]	t_R [h]
P91-05	5607	28	12.13	1		2.82	
P91-08	4373	22.4	12.2	4		2.23	
P91-02	3818	19.2	12.19	11		1.47	
P91-10	2982	14.9	12.1	35		2.8	

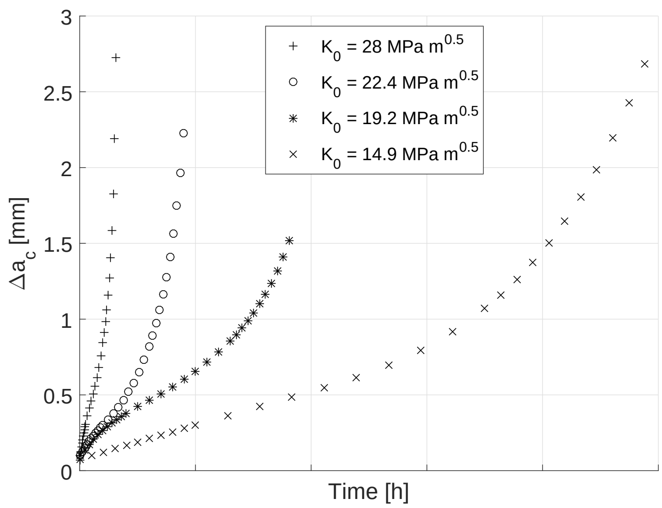

Figure 2.10: *Creep crack propagation as a function of the test time for P91 at 600 °C.*

performed at lower initial stress intensity factor last longer. CCI data can be plotted as the stress intensity factor K_{Ii} evaluated at the initiation time t_i, i.e. when the creep crack propagation Δa_c reaches 0.2 mm. The stress intensity factor solution used to

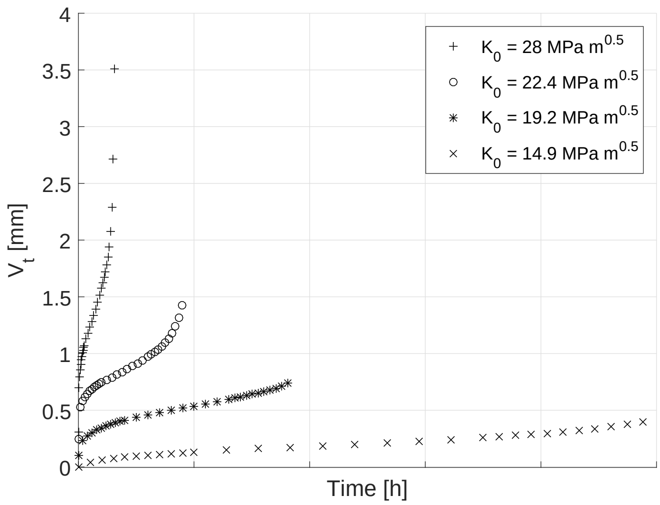

Figure 2.11: *Load-line displacement during the CCG tests.*

Table 2.5: *Coefficients of Eq.* (2.4) *of P91 at 600 °C.*

$M[MPa\sqrt{m}h^{-p}]$	p

calculate K_{Ii} for C(T) specimens is the one reported in Eq. (2.2)

$$K = \frac{P}{(BB_n)^{0.5}W^{1/2}}F \tag{2.2}$$

where F is the shape function that for C(T) specimens is defined as:

$$F = \left[\frac{2+a/W}{(1-a/W)^{3/2}}\right](0.886 + 4.64(a/W) - 13.32(a/W)^2 + 14.72(a/W)^3 \\ -5.6(a/W)^4) \tag{2.3}$$

The trend shown in Fig. 2.12 was fitted to the power law of Eq. (2.4) and will be used in Ch. 3 for CCI assessment of pipe components.

$$K_{Ii} = Mt_i^p \tag{2.4}$$

The coefficients obtained by this fitting procedure are reported in Tab. 2.5. The crack propagation rate exhibits the same behavior in all load conditions. In fact during CCI it slowly decrease reaching its minimum until the beginning of EC conditions where it increases until the rupture time t_R. Moreover the minimum crack propagation rate decreases for lower initial stress intensity factors. The plot of total load-line displacement V_t of Fig. 2.11 confirms this trend.

As previously anticipated, after the tests, the specimens were brittle broken in liquid nitrogen in order to observe the pre-crack and final crack fronts by means of optical

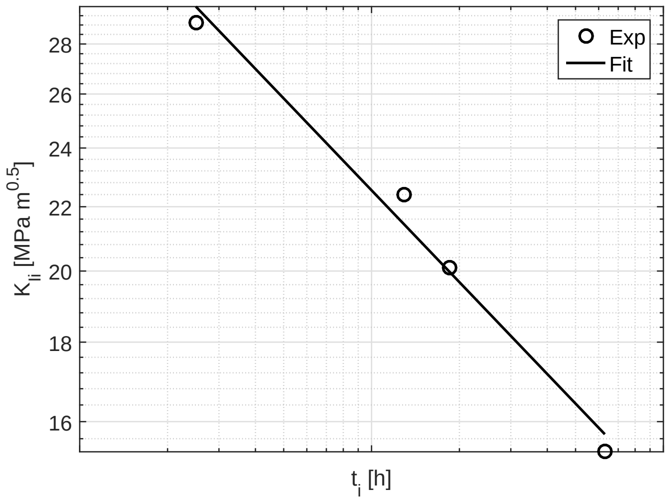

Figure 2.12: *Stress intensity factor at initiation as a function of initiation time.*

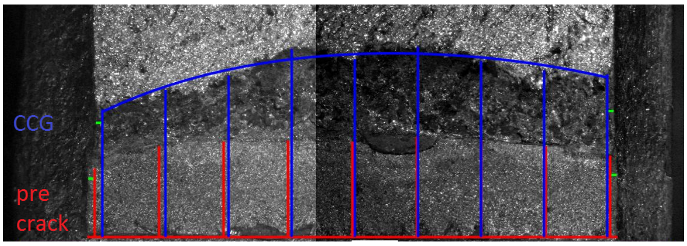

Figure 2.13: *Application of the ASTM E1457 [6] crack validity criteria.*

microscopy and to perform the crack validity criteria provided by ASTM E1457 [6] that determine if the validity of the CCG test, on the basis of nine equidistant point measurements along the crack front (Fig. 2.13). Each specimen passed the ASTM E1457 [6] crack validity criteria (Fig. 2.14) and thus it was possible to analyze the experimental data to estimate the CCG crack tip parameters. The steady-state creep crack tip parameter C^* can be calculated only:

- when the ratio between the creep LLD rate $\dot{V}_c$ and the total LLD rate $\dot{V}_t$ is greater than 0.5
- at times greater than the transition time t_T as defined from Eq. (1.34)
- at times greater than the time to CCI t_i.

Under the hypothesis that the LLD rate given by monotonic plasticity is negligible, $\dot{V}_c$ can be isolated from $\dot{V}_t$ by defining the instantaneous elastic LLD rate $\dot{V}_0$ in relation to the crack propagation rate and the stress intensity factor K:

$$\dot{V}_0 = \frac{da}{dt}\frac{B_n}{P}\left(\frac{2K^2}{E'}\right) \tag{2.5}$$

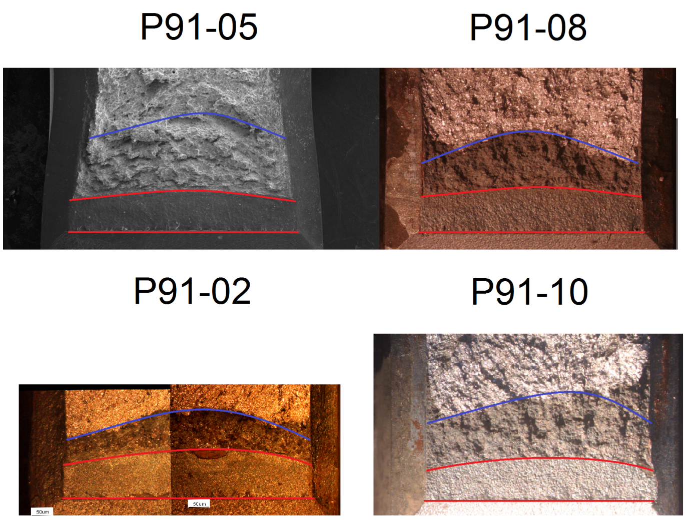

Figure 2.14: *Pre-crack (red) and final crack fronts (blue) after specimen break in liquid nitrogen.*

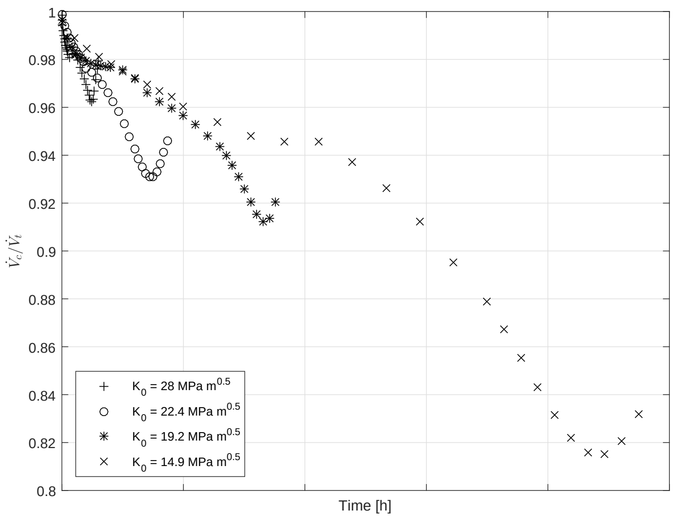

Figure 2.15: *Ratio between creep and total LLD rate.*

where E' is equal to E and $E/(1-\nu^2)$ in plane stress and plane strain conditions respectively. The LLD rate given by creep deformation is obtained by using Eq. (1.42). The ratio between creep and total LLD rate of Fig. 2.15 is always greater than 0.5 validating, according to the ASTM E1457 standard [6], the use of C^* as a crack tip parameter. As reported in Tab. 2.4, the initiation time t_i represents the threshold for the estimation of the C^* parameter, as it is always greater than the corresponding transition time t_T. The C^* parameter can now be estimated, after CCI, by using a modified version of Eq. (1.14) that accounts for side grooved specimens:

$$C^* = \frac{P\dot{V}_t}{B_n(W-a)} H^{LLD} \eta^{LLD} \tag{2.6}$$

Table 2.6: *tab:EtaLLD.*

a/W	η^{LLD}
0.35	1.89
0.40	2.07
0.45	2.20
0.50	2.20
0.60	2.20
0.70	2.20

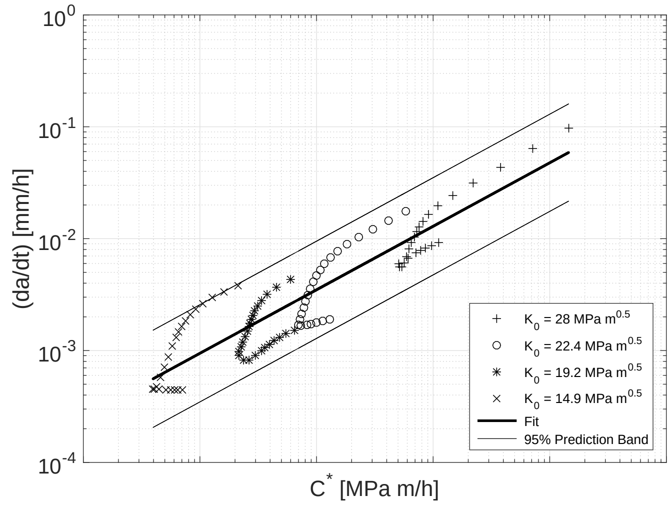

Figure 2.16: *Crack propagation rate as a function of the C^* parameter obtained experimentally.*

where H^{LLD} is a function of the Norton law exponent (for C(T) specimens $H^{LLD} = n/(n+1)$) and η^{LLD} is a function of the crack size a/W as reported in Tab. 2.6 for C(T) specimens.

The crack propagation rate is plotted in Fig. 2.16 as a function of the experimental values of C^* for all the tests. As expected, the lower the applied loads are, the lower the crack propagation and LLD rates are resulting in lower estimations of C^*. It might be worth noting that even if data prior initiation time have been cut out, the relationship between (da/dt) and C^* at the beginning of the test is not unique. This behavior can be attributed to the fact that the examined material is interested by a long small-scale creep phase characterized by a dominant primary creep strain that extends beyond the initiation times. However in EC conditions, the data points lie on a line. Thus, the power law fit of Eq. (1.19) was used to interpolate the crack propagation rate with the C^* parameter. The results of this fit are shown in Fig. 2.16 as the thick continuous line together with the 95% prediction bounds. Material constants for the fit and the 95% bands are reported in Tab. 2.7.

Table 2.7: *Coefficients of Eq.* (1.19) *for P91 at 600 °C.*

	D $[mm/(MPam)^{\phi}h^{\phi-1}]$	ϕ
Fit		
Upper bound		
Lower bound		

Moving to the C_t parameter valid for SSC, TC, and EC conditions of Eq. (1.61), this equation, modified in order to account for side grooves of C(T) specimens, becomes:

$$\frac{P\dot{V}_c}{(BB_n)^{0.5}W}\frac{F'}{F} - C^* \left(\frac{F'}{\eta F} - 1\right) \tag{2.7}$$

where the term F'/F was taken from the CFCG testing ASTM E2760-10 standard [18]:

$$\begin{aligned} \frac{F'}{F} &= \left[\frac{1}{2+a/W} + \frac{3}{2(1-a/W)}\right] + \\ &+ \left[\frac{4.64 - 26.64(a/W) + 44.16(a/W)^2 - 22.4(a/W)^3}{0.886 + 4.64(a/W) - 13.32(a/W)^2 + 14.72(a/W)^3 - 5.6(a/W)^4}\right] \end{aligned} \tag{2.8}$$

and the term η can be expressed for C(T) specimens with creep exponent $n = 10$, an average condition between the high and low stresses Norton law constants of Tab. 2.3, as a function of the crack size a/W as shown in Tab. 2.8: The η values of Tab. 2.8 have

Table 2.8: *η values for C(T) specimen with $n = 10$.*

a/W	$\eta(a/W, n = 10)$
0.4	3.504
0.5	4.111
0.6	5.020
0.7	6.536
0.8	9.563

been extended to intermediate a/W values thanks to a 4th grade polynomial fit.
The obtained C_t values are plotted in Fig. 2.17 with the crack propagation rates. As shown, at the beginning of the test, the relationship between (da/dt) and C_t is not unique. This can be explained considering that the C_t parameter is defined under the hypothesis that no crack propagation occurs during small-scale creep but, for the investigated material, as previously observed in the C^* parameter estimation, this phase (SSC) extends longer than the initiation time. Results were fitted to the power law of Eq. (1.62). The D' and ϕ' values for the fit and upper/lower prediction bands are reported in Tab. 2.9 according to the experimental results.

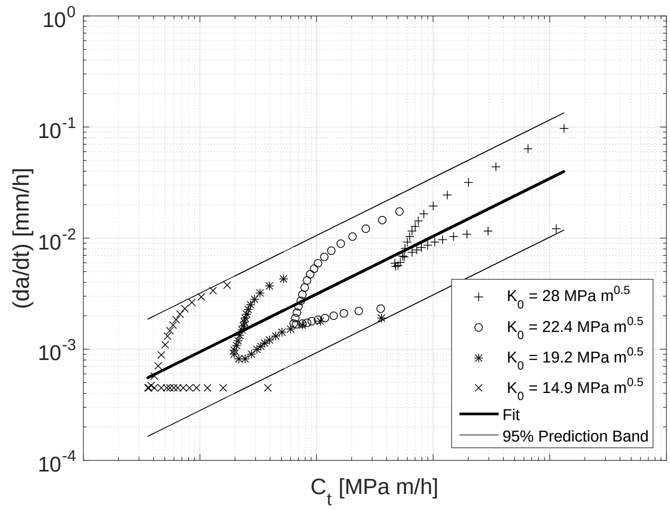

Figure 2.17: *Crack propagation rate as a function of the crack tip C_t parameter valid for SSC, TC, and EC conditions.*

Table 2.9: *Coefficients of Eq.* (1.62) *for P91 at 600 °C.*

	D' $[mm/(MPam)^{\phi'}h^{\phi'-1}]$	ϕ'
Fit		
Upper bound		
Lower bound		

2.3 CFCG Tests [22]

In the late years, CFCG tests are starting to play an important role in material characterization in presence of defects. The aim of this series of tests is to investigate the interaction phenomena between the fatigue damage experienced by the material during the load and unload cycle at high temperature, and the creep damage experienced by the material during the hold time under sustained load at high temperature.
In particular, the focus is on the effects of initial nominal stress intensity factor, as well as on the effects of the hold time period in the range 0.1-10 h, of interest for the application of the investigated material. All the CFCG tests presented in this work have been carried out at 600 °C according to the applicable ASTM E2760-10 standard [18]. The same C(T) specimen configuration of CCG tests (Fig. 2.7) was tested in order to avoid any effect of geometry in the experimental results.

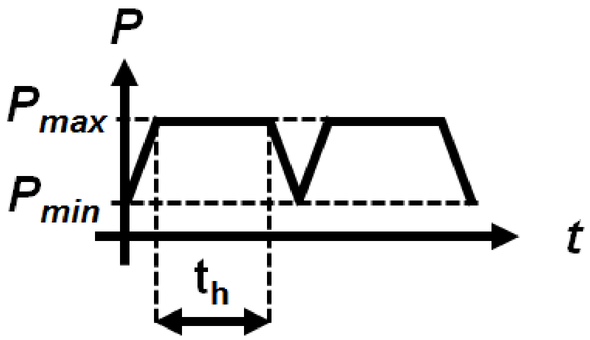

Figure 2.18: *Trapezoidal shaped load of CFCG tests.*

2.3.1 CFCG Experimental Tests

Most of CFCG tests were performed on the same CCG testing machine SATEC JE 1016 that was modified for the occasion. A brushless motor designed to balance the leverage system was used to apply and remove the load to the specimen at the end of a predefined hold time t_h. The total load was then split in two parts. One part is always applied to the train load in order to obtain a load ratio $R > 0$, while the remaining part is applied and released according to the trapezoidal shaped load of Fig. 2.18.

As for CCG tests, room temperature pre-crack is required in order to obtain a sharp starter crack, and all C(T) specimens have been side grooved to obtain a straight crack propagation necessary for crack validation measurements. The test procedure applied to CFCG tests is similar to the one previously described for CCG tests. Crack propagation rates have been calculated from direct current PD measurements, one time for cycle at the beginning of each hold phase. The LLD was acquired several times per cycle during the load hold phase, in order to obtain the creep load-line deflection variation ΔV_c according to Fig. 1.16. For comparison, specimen P91-26 was tested on a servo-hydraulic testing machine. In these case, the C(T) dimensions of this specimen are shown in Fig. 2.33, and the crack propagation rate was recorded by means of elastic compliance.

The CFCG test matrix is reported in Tab. 2.10 comprehending: the nominal stress intensity factor range ΔK_0 at the beginning of the test, the maximum stress intensity factor at the beginning of the test $K_{max,0}$ the initial crack size a_0, the final crack size a_f, the creep-fatigue crack propagation Δa_{cf}, and the rupture time t_R. As shown, a load ratio $R = 0.1$ was studied at different values of initial stress intensity factor ranges ΔK_0 at different hold times t_h.

Table 2.10: *Creep-fatigue crack growth tests matrix.*

Specimen	R	P [N]	t_h [h]	ΔK_0 [MPa m$^{0.5}$]	$K_{max,0}$ [MPa m$^{0.5}$]	a_0 [mm]	a_f [mm]	Δa_{cf} [mm]	t_R [h]
P91-26	0.1	8714	0.1	22.6	25.11	7.99	9.49	1.50	
P91-06	0.1	4750	0.1	21.5	23.88	12.17	19.77	7.60	
P91-137-09	0.1	4435	1	21.2	23.55	12.64	13.23	0.59	
P91-137-10	0.1	4730	10	21.7	24.11	12.31	15.60	3.29	
P91-137-01	0.1	3615	1	16.4	18.22	12.22	14.91	2.69	
P91-07	0.1	3530	2	15.6	17.33	11.99	12.49	0.5	

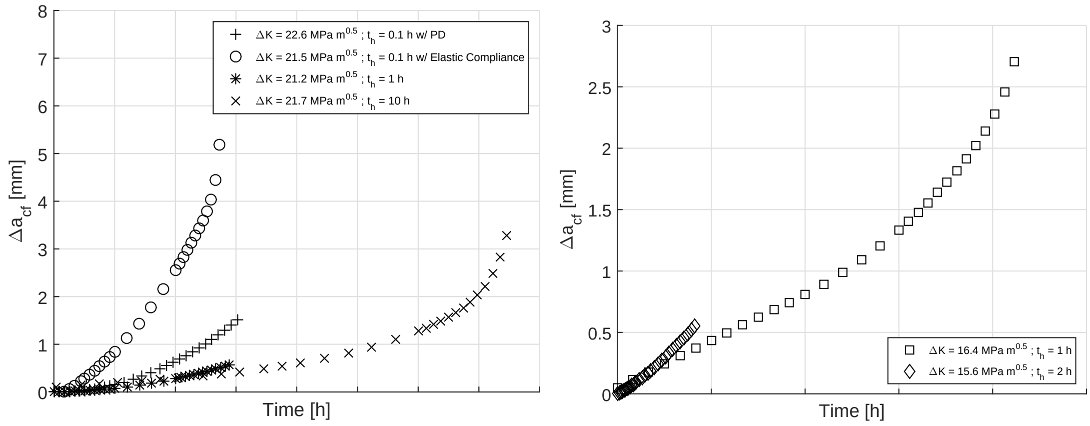

(a) *Nominal* $\Delta K_0 = 21\ MPam^{0.5}$.

(b) *Nominal* $\Delta K_0 = 16\ MPam^{0.5}$.

Figure 2.19: *Crack propagation of CFCG tests of P91 at 600 °C.*

2.3.2 CFCG Test Results

Figure 2.19 (a) reports CFCG tests performed at a maximum initial nominal value of stress intensity factor $K_{max,0}$ equal to 23.3 and $\Delta K_0 = 21$, with different hold times ranging from 0.1 h and 10 h. The results show the effect of the increasing hold time that reduces the crack propagation rate significantly. Moreover, The test with hold time equal to 0.1 h is the one performed for comparison on a servo-hydraulic testing machine, where the crack propagation was monitored by means of the elastic compliance method. It can be observed a significant difficulty in estimating the crack propagation by means of compliance method for low values of crack length ($< 0.5mm$) that reflects in a different trend of the two curves in particular during the first stage of the crack propagation. Comparing the results of Fig. 2.19 (a) and (b) it can be observed that at the same values of hold time, the crack propagation rate decreases with the initial value of stress intensity factor amplitude.

After each test, specimens were brittle broken in liquid nitrogen for the five crack validation measurements as disposed by the ASTM E2760 standard [18] and as reported in Fig. 2.20 for specimen P91-07. The creep-fatigue crack fronts are shown in Fig.

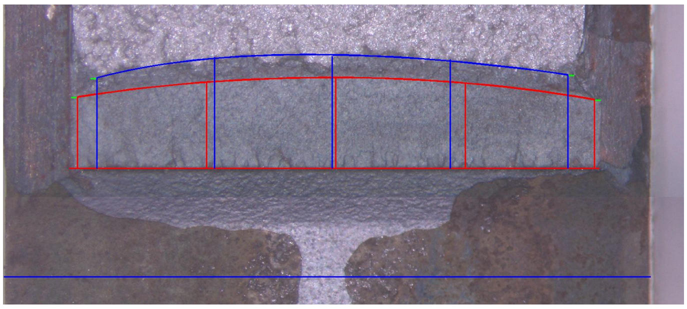

Figure 2.20: *Crack validity check on five point measurements on specimen P91-07.*

2.21 and resulted valid for all the tests. The crack tip paramter $(C_t)_{avg}$ was calculated

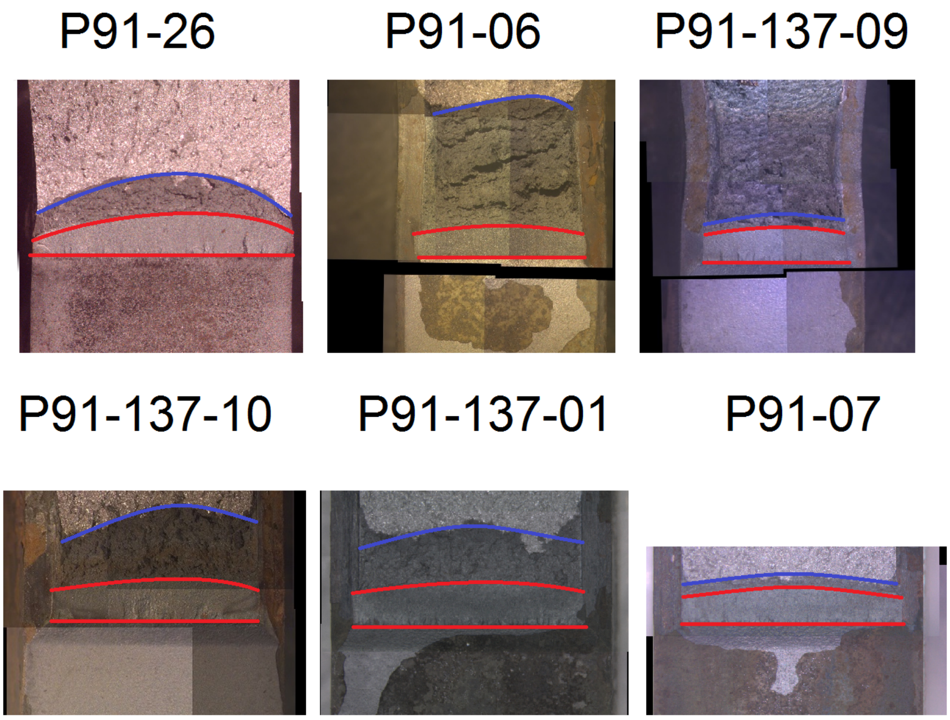

Figure 2.21: *Pre-crack and final crack fronts of the CFCG tests after liquid nitrogen failure.*

by measuring the load-line deflection rate during the hold time of each cycle. Equation (1.65) was modified according to ASTM standard [18] to account for side grooved C(T) specimens:

$$(C_t)_{avg} = \frac{\Delta P \Delta V_c}{(BB_n)^{1/2} W t_h} \frac{F'}{F} \tag{2.9}$$

The average crack propagation rate is shown as a function of the crack tip parameter in Fig. 2.22. However at low hold times of the order of 0.1 h the LLD change is reduced and therefore it does not allow a reliable $(C_t)_{avg}$ estimation. For specimens P91-06 and THOR-137-09 no reliable load-line deflection rates were measured thus it was not possible to evaluate the $(C_t)_{avg}$ parameter accurately and are not reported in Fig. 2.22. As for the previous CCG tests, a power law fit was performed to relate

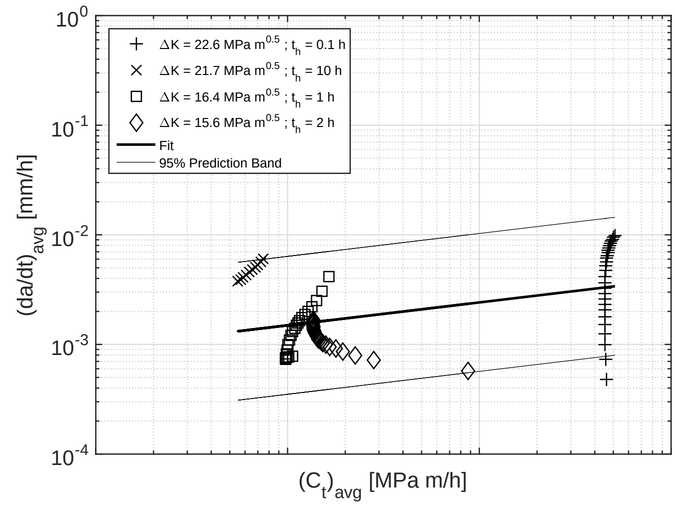

Figure 2.22: *Average crack propagation rate as a function of the $(C_t)_{avg}$ parameter for P91 steel at 600 °C at different initial stress intensity factor ranges and hold times.*

average crack propagation rate to the $(C_t)_{avg}$ parameter according to Eq. (1.66). The coefficients found during the fitting procedure are reported in Tab 2.11 together with the correspondent upper and lower 95% prediction band.

As previously discussed in Ch. 1, an analytical estimation of the $(C_t)_{avg}$ parameter is

Table 2.11: *Coefficients of Eq. (1.66) for P91 at 600 °C based on the numerical estimation of $(C_t)_{avg}$.*

	D'' $[mm/(MPam)^{\phi''} h^{\phi''-1}]$	ϕ''
Fit		
Upper bound		
Lower bound		

possible by using a Norton law based creep model that describes the evolution of the creep zone size during a CFCG test. Equation (1.67) defines the crack tip parameter under the hypothesis of complete creep reversal given by the fatigue cycles. $(C_t)_{avg}$ depends on the stress intensity factor range ΔK, the hold time t_h, the Norton creep law multiplier and exponent A and n, and the crack tip parameter in CCG conditions C^*. C^* was also obtained by means of Eq. (1.18a) that was derived from numerical simulations. If a C(T) specimen is studied the calibration function $h_1(a/W, n)$ has

Table 2.12: *h_1 calibration function for C(T) specimens with different crack sizes and creep exponent n.*

	n								
a/W	1	2	3	5	7	10	13	16	20
0.25	2.23	2.05	1.78	1.48	1.33	1.26	1.25	1.32	1.57
0.375	2.15	1.72	1.39	0.970	0.693	0.443	0.276	0.175	0.098
0.5	1.94	1.51	1.24	0.919	0.685	0.461	0.314	0.216	0.132
0.625	1.76	1.45	1.24	0.974	0.752	0.602	0.459	0.347	0.248
0.75	1.71	1.42	1.26	1.033	0.864	0.717	0.575	0.448	0.345
$\approx$1	1.57	1.45	1.35	1.18	1.08	0.95	0.85	0.73	0.630

the values of Tab. 2.12. The $(C_t)_{avg}$ parameter obtained with this approximation is shown in Fig. 2.23 The tests performed at $\Delta K_0 = 22.6$, 21.2, and 15.6 were stopped

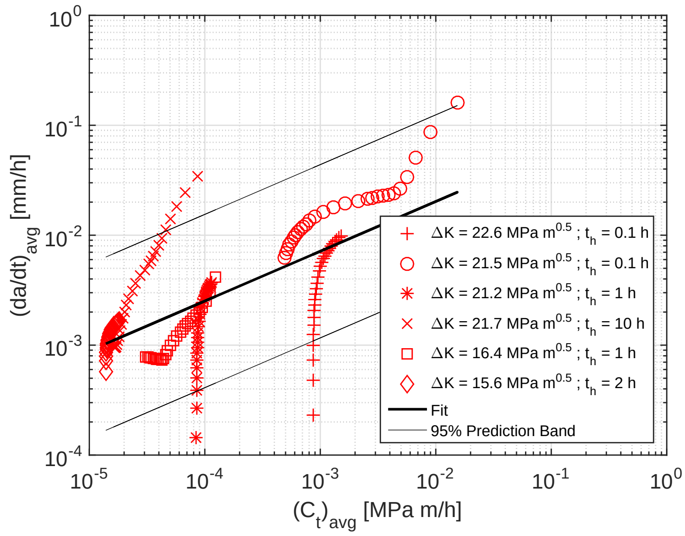

Figure 2.23: *$(da/dt)_{avg}$ as a function of the crack tip parameter $(C_t)_{avg}$ calculated analytically for P91 steel at 600 °C.*

at the beginning of the tertiary and last phase of the test without providing a sufficient crack growth rate increment. The power law fitting procedure was performed also on this analytical estimations on the $(C_t)_{avg}$ parameter obtaining the coefficients of Tab. 2.13. Until this step, the crack tip parameter suitable to represent CFCG was calculated

Table 2.13: *Coefficients of Eq.* (1.66) *for P91 at 600 °C based on the analytical estimation of $(C_t)_{avg}$.*

	D'' $[mm/(MPam)^{\phi''} h^{\phi''-1}]$	ϕ''
Fit	0.1631	0.4528
Upper bound	1.0014	0.4528
Lower bound	0.0266	0.4528

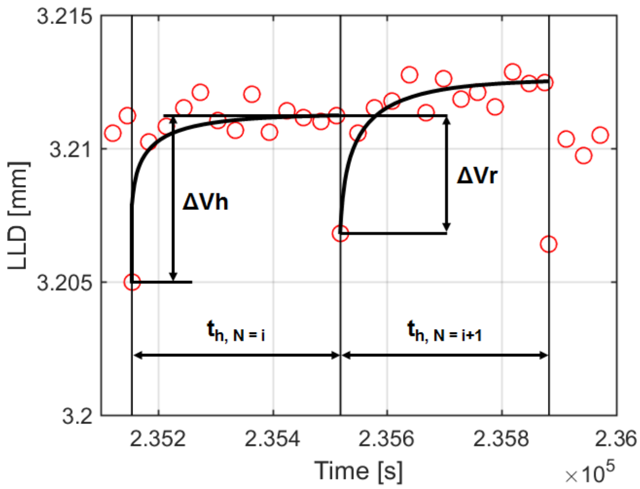

Figure 2.24: *Schematic diagram for ΔV_h and ΔV_r determination.*

Table 2.14: *Stabilized values of C_R.*

Test:		C_R
$\Delta K = 22.6$ MPa m$^{0.5}$	$t_h = .1$ h	
$\Delta K = 16.2$ MPa m$^{0.5}$	$t_h = 1$ h	
$\Delta K = 15.6$ MPa m$^{0.5}$	$t_h = 2$ h	
$\Delta K = 15.6$ MPa m$^{0.5}$	$t_h = 2$ h	
Average value		

experimentally, and analytically by means of Eq. (1.67) that assumes that all the creep strain is reversed during the load release after the hold time. In real applications, the creep strain reverse given by cyclic load is represented by a percentage of the creep strain. The experimentally defined creep reversal parameter C_R, studied by Grover and Saxena [28], is able to define how the cyclic load reinstate the crack tip stress field during the unloading portion of the trapezoidal fatigue load cycle. It is calculated from experimental load-line deflection of CFCG tests as the ratio between the load-line deflection range calculated between the end of the hold time of one cycle and the beginning of the hold time of the next cycle, and the load-line deflection during the hold time. A schematic representation of how it can be calculated is shown in Fig. 2.24 based on the experimental data of the CFCG test P91-26. The experimental values of C_R found by analysing the experimental load-line deflections is plotted in Fig. 2.25 as a function of the normalized test time together with its average value after the initial transition. The stabilized values of C_R are reported in Tab 2.14. An average value of C_R of was used in the following calculations. The crack tip parameter for creep-fatigue tests under the hypothesis of partial creep reversal may now

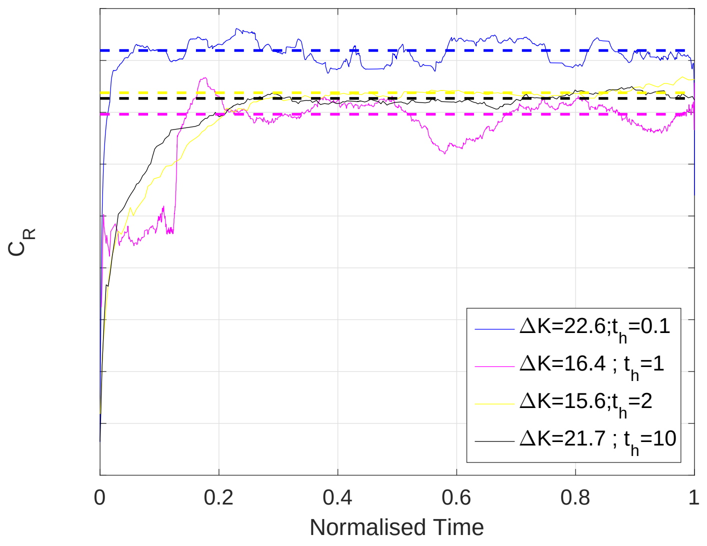

Figure 2.25: *Creep reversal parameter C_R as a function of normalized time for P91 at 600°C.*

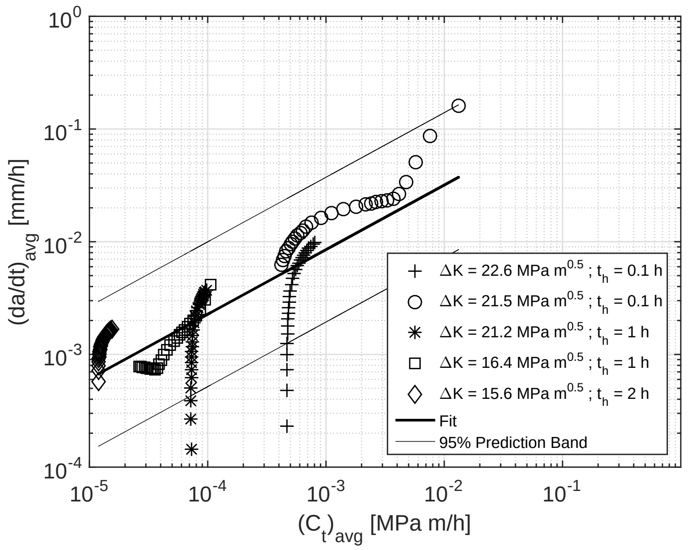

Figure 2.26: *Creep-fatigue average crack propagation rate as a function of the $(C_t)_{avg}$ parameter calculated by assuming the partial reverse of creep strains through the C_R parameter.*

be calculated according to Eq. (1.66) and related to the average CFCG rates as shown in Fig. 2.26. The linear relationship through the logarithmic values of $(da/dt)_{avg}$ and $(C_t)_{avg}$ is defined by a power law with the coefficients D'' and ϕ'' reported in Tab. 2.15. The results discussed in this Section represent the experimental characterization of the creep-fatigue behavior of the investigated material according to the new concept of $(C_t)_{avg}$ parameter (Eq. (1.65)), that accounts for continuous restart of the creep damage accumulation at the crack tip of the propagating crack under creep-fatigue regime.

Table 2.15: *Coefficients of Eq.* (1.66) *for P91 at 600 °C based on the analytical estimation of* $(C_t)_{avg}$ *through the creep reversal parameter* C_R.

	D'' $[mm/(MPam)^{\phi''}h^{\phi''-1}]$	ϕ''
Fit	0.4456	0.5731
Upper bound	1.9560	0.5731
Lower bound	0.1015	0.5731

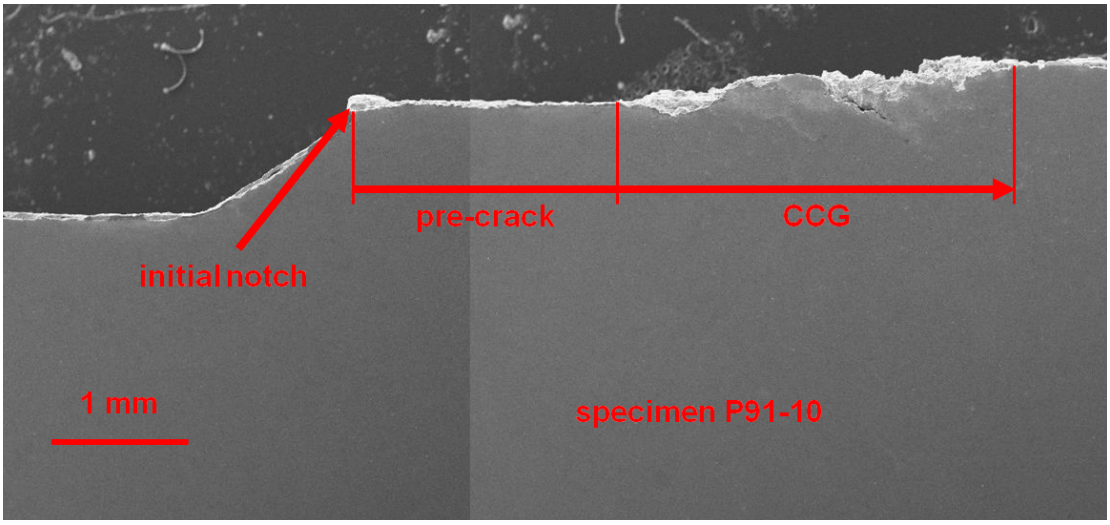

Figure 2.27: *Fracture surface of specimen P91-10 after CCG test at* $K_0 = 14.9$ *MPa m*$^{0.5}$.

2.4 Creep and Creep-Fatigue Damage at the Crack Tip

The C(T) specimens tested in CCG and CFCG conditions have been observed by means of scanning electron microscope (SEM) in order to characterize the evolution of the damage mechanisms. For this purpose, after brittle breaking in liquid nitrogen, one half of each specimen was sectioned at the midline section ($B/2$) using a micro miter saw that does not alter the damaged surface as shown in Fig. 2.27. The straight crack path associated to the room temperature pre-crack shows a trans-granular fracture while the irregular shape associated to CCG is given by inter-granular fracture typical of creep damage. The backscattering SEM image of Fig. 2.28 performed at $\Delta a_c = 1.8$ mm, below the crack surface, shows an high density of microvoids of different sizes. These microvoids are located at the grain boundaries, as observed in Fig. 2.29 and coalesce proportional to the creep strain. Microvoids coalescence starts originating microcracks (Fig. 2.30a) oriented $45°$ from the crack front. These microcracks, close to the crack tip where stresses are higher, lead to the formation of subcracks causing macro crack propagation (Fig. 2.30b). By observing the creep-fatigue fracture surfaces,

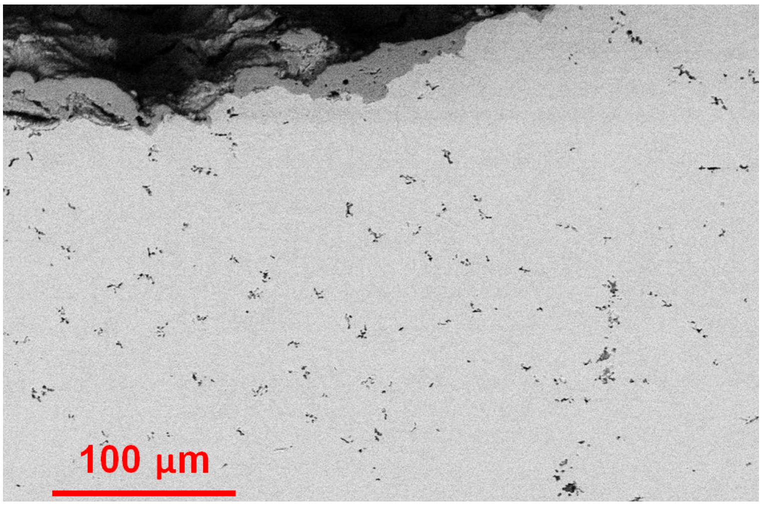

Figure 2.28: *Backscattering image of P91-10 at* $\Delta a_c = 1.8$ *mm.*

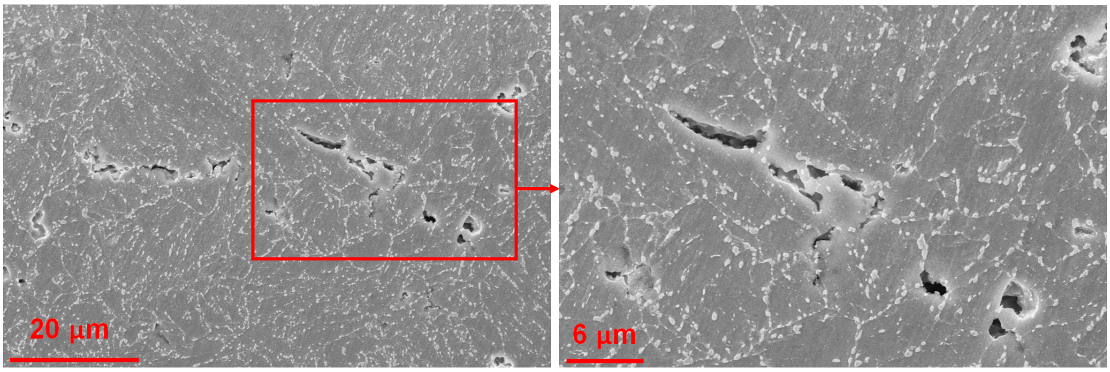

Figure 2.29: *SEM detail of microvoids on P91-10 specimen.*

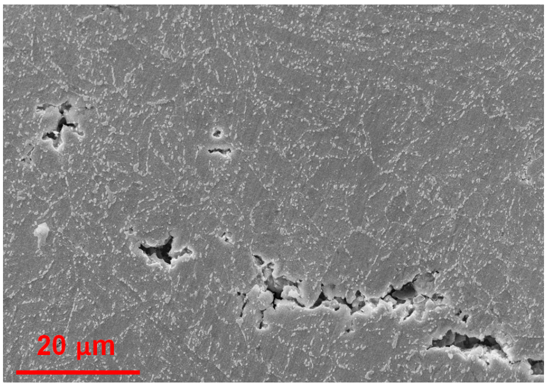

(a) *Microcrack.*

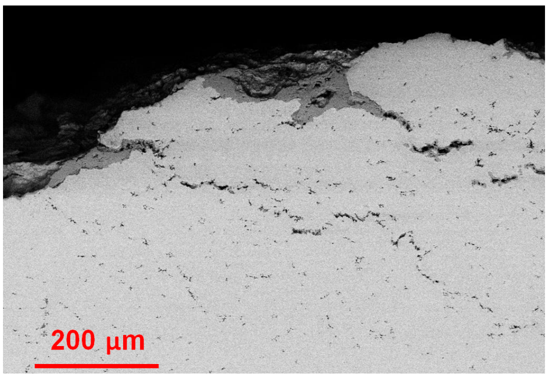

(b) *Subcracks.*

Figure 2.30: *Microcracks formation observed with SEM at the end of the creep crack propagation of test P91-10.*

it has been found that in short hold time tests ($t_h = 0.1$, 1 h) where fatigue is dominant, the crack path is characterized by higher peaks and valleys compared to the CFCG test

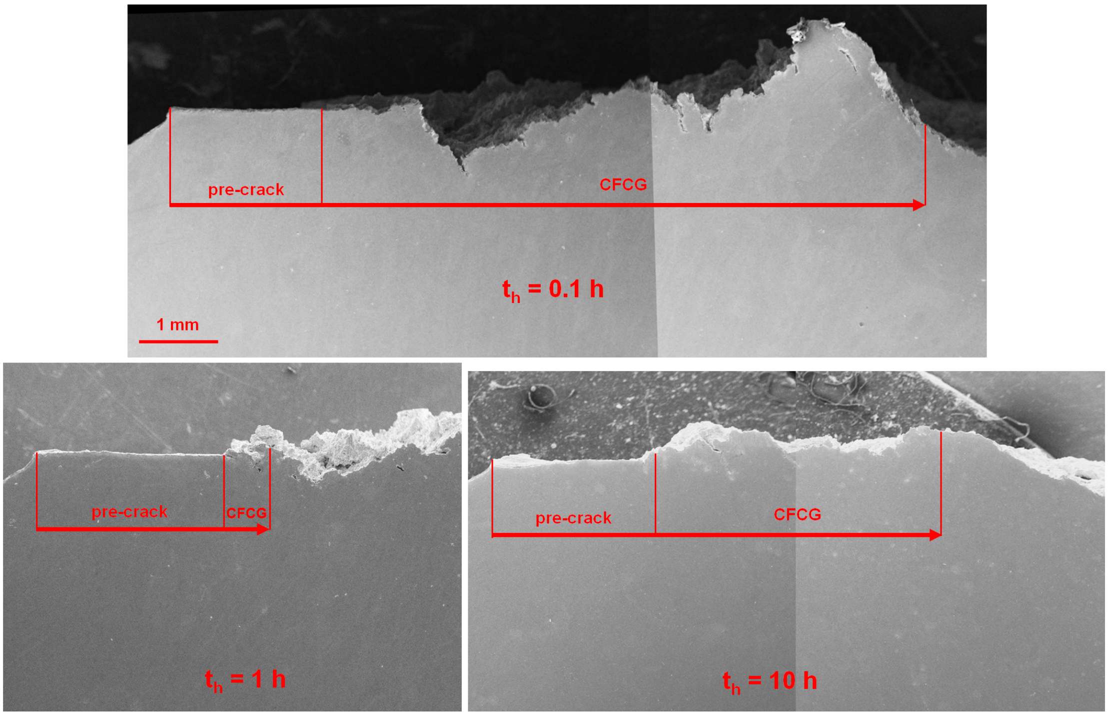

Figure 2.31: *Crack paths of CFCG tests performed on P91 at 600 °C.*

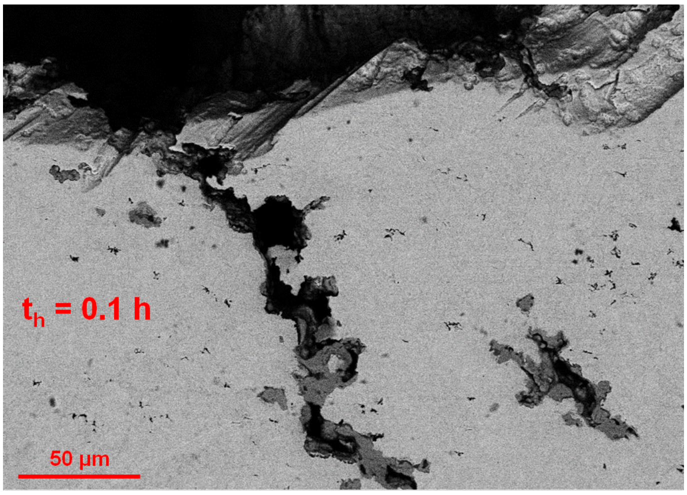

Figure 2.32: *Creep-fatigue fracture mechanisms by voids coalescence and microcracks formation.*

with 10 hours hold time as shown in Fig. 2.31. The mechanism of fracture observed from CFCG tests is the same of CCG tests, starting with void growth and coalescence followed by microcracks formation that, at long terms, origins the macrocrack (Fig. 2.32 The SEM observations suggest that in order to be able to predict creep and creep-fatigue damage correctly, a big effort must be spent to identify a suitable cavity growth theory that accounts for void coalescence and intergranular fracture.

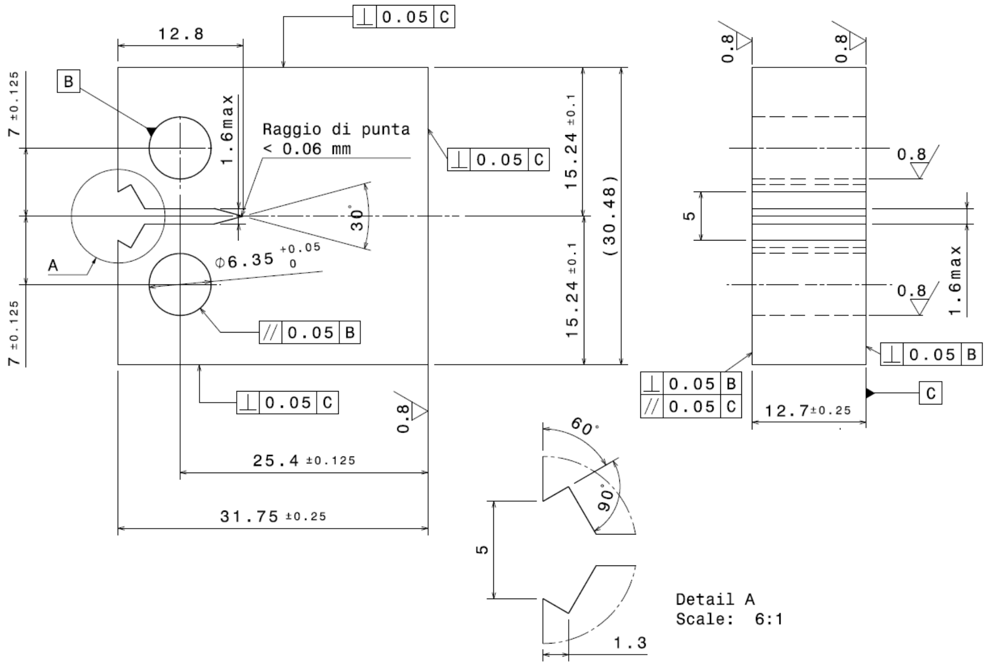

Figure 2.33: *Front face C(T) specimen used in FCG tests.*

2.5 FCG Tests [22]

Fatigue crack growth tests at high temperature were performed in order to be able to analyze the CFCG as a decomposition between pure fatigue and creep damages (Eq. (1.79). From this viewpoint, high and medium (10, 1 Hz) frequency fatigue tests are expected to exclude any stress relaxation allowing the estimation of the high temperature fatigue damage exclusively. All FCG tests have been carried out according to the ASTM E647 standard [19]. The constant load procedure is intended to estimate the coefficients of the Paris-Erdogan law of Eq. (1.76) at different load ratios R and frequencies f.

2.5.1 FCG Tests Experimental Setup

Since at high frequencies PD measurements are not possible, the C(T) specimen geometry presented in Sec. 2.2 has been modified in order to accommodate an high temperature extensometer for crack size determination by means of elastic compliance. The specimen geometry is shown in Fig. 2.33. All tests were performed on a MTS 793 servo-hydraulic testing machine and that supports a maximum load of 100 kN. In order to start the test with a sharp notch, all the specimens were room temperature precracked and the crack length was controlled by means of clip-on gage extensometer. After precracking, specimens were loaded on the testing machine inside a two controlled zones

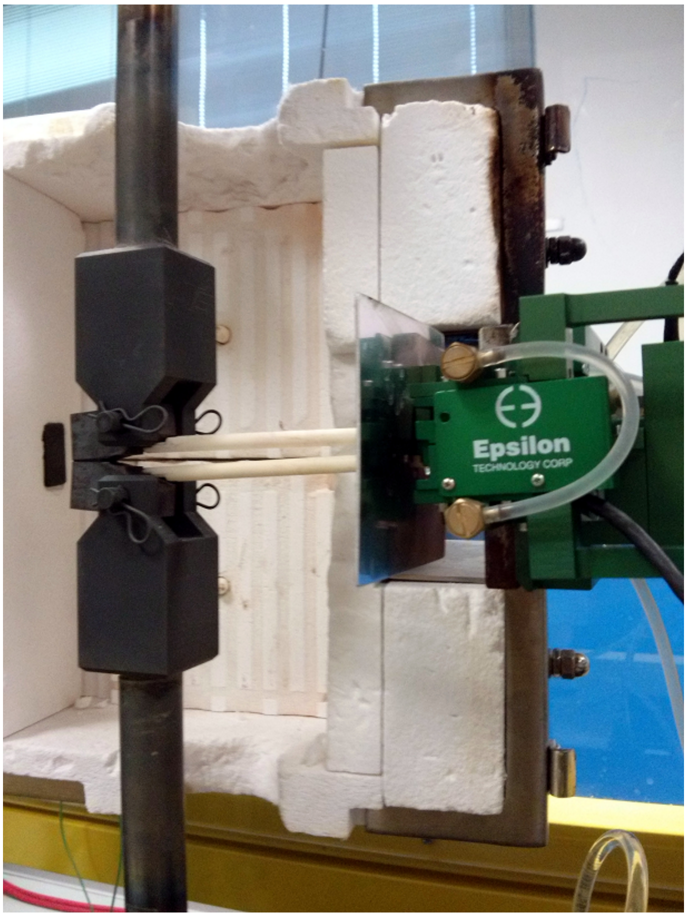

Figure 2.34: *FCG test setup showing furnace and HT extensometry.*

furnace that was heated until the temperature of 600 °C (Fig. 2.34). Because no thermocouples were used during the test, a temperature calibration was needed. For this reason six K type thermocouples were welded to both sides of a dummy specimen at low medium and high position. When the six thermocouples range of temperature was within ± 2°C from the set temperature the upper and lower temperature values of the oven were saved and used for the FCG tests. Prior beginning the test, the crack length given by elastic compliance was verified together with the elastic modulus. Tests were performed in load control. A sinusoidal shaped load wave was applied between a maximum and minimum value that remained constant until the end of the test. During fatigue load, elastic compliance, crack length, and cycle number were continuously monitored until the gauge length of the extensometer was reached. The test matrix for FCG tests is summarized in Tab. 2.16 indicating that two load ratios R =0.1 and 0.7 were studied as well as two frequencies $f = 1$ and 10 [Hz]. In Tab. 2.16 is also reported the initial stress intensity factor range ΔK_0, the maximum initial stress intensity factor $K_{max,0}$, the initial crack length a_0, and the fatigue crack propagation Δa_f. After each

Table 2.16: *FCG test matrix.*

Specimen	R	f [Hz]	ΔK_0 [MPa m$^{0.5}$]	$K_{max,0}$ [MPa m$^{0.5}$]	a_0 [mm]	Δa_f [mm]
P91-24	0.1	1	15	16.66	8.5	11.21
P91-22	0.1	10	15	16.66	8.37	11.55
P91-25	0.7	1	5	16.66	8.26	10.71
P91-23	0.7	10	5	16.66	8.59	10.98

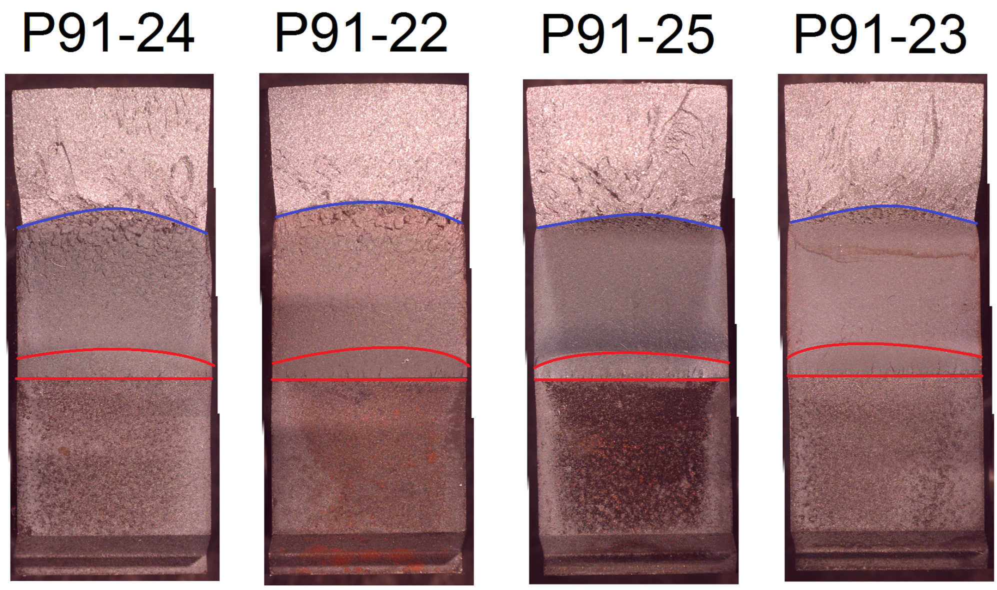

Figure 2.35: *Pre-crack (red) and final crack fronts (blue) of the FCG tests after liquid nitrogen failure.*

test the specimens were brittle broken in liquid nitrogen in order to check the initial and final crack front sizes as shown in Fig. 2.35

2.5.2 FCG Tests Results

The results in terms of crack propagation per cycle as a function of the applied stress intensity factor range are shown in Fig. 2.36 As expected tests performed at low frequency f = 1 Hz exhibit the highest crack propagation rates. This might be an indication that creep damage is already starting to affect the crack propagation negatively. The crack propagation per cycle is lower at higher load ratios even if specimen failure happens earlier. Since the experimental data plotted on a logarithmic scale provided a linear behavior, they were fitted to the Paris-Erdogan law of Eq. (1.76). The sets of constant of this fitting procedure at different load ratios and frequencies are summarized in Tab. 2.17. The constants obtained at high frequency are assumed to represent the pure high temperature fatigue behavior and thus will be used in the following application of

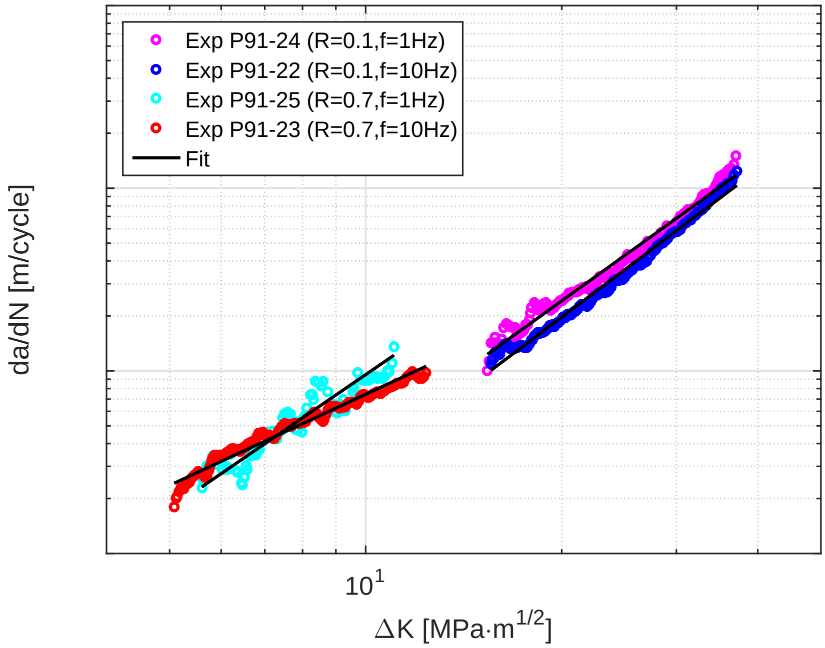

Figure 2.36: *FCG test results of P91 at 600 °C at different frequencies and load ratios.*

Table 2.17: *Paris-Erdogan law fit results.*

Specimen	C [$m^{1\text{-}m/2}$ MPa^{-m} N^{-1}]	m
P91-24		2.5647
P91-22		2.6831
P91-25		2.4430
P91-23		1.6559

the superposition model.

2.6 Superposition model for CFCG crack estimation.

The model discussed in Sec. 1.3 uses the concept of linear superposition of crack propagation due to creep and fatigue damages. The crack propagation during one cycle is then defined as the summation between the fatigue crack growth during one cycle depending on the Paris-Erdogan law and the creep-fatigue crack growth during the hold time that, is related to the crack tip parameter $(C_t)_{avg}$. Among the Paris-Erdogan law constants of Tab. 2.17, the one associated to test P91-22 were chosen to predict the CFCG tests. The reason of this choice stands in the higher frequency of this test ($f = 10$ Hz) that excludes any significant stress relaxation given by creep strains and the load ratio $R = 0.1$ equal to the CFCG tests that are going to be modelled. The model used to simulate the creep-fatigue portion of crack propagation depends on the power law fit

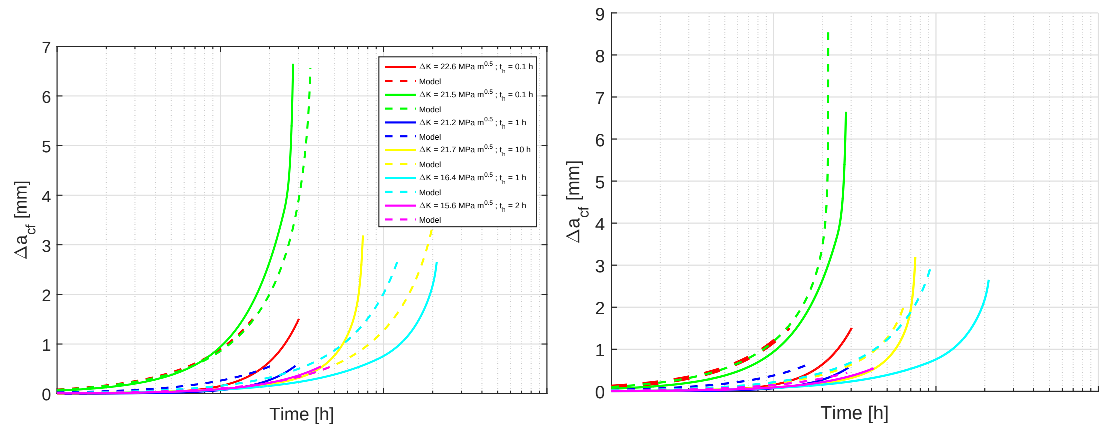

(a) *Complete creep reversal.*

(b) *Partial creep reversal.*

Figure 2.37: *Creep-fatigue crack propagation according to the superposition model.*

of Sec. 2.3.2. Due to the lack of reliable experimental load-line deflection records at short hold times, the fit constants used in the superposition model are the one reported in Tab. 2.11 that have been found by analysing Eq. (1.67). The crack propagation per cycle is defined according to the following equation:

$$\frac{da}{dN} = C\Delta K^m + t_h D'' \left((C_t)_{avg}\right)^{\phi''} \tag{2.10}$$

where $(C_t)_{avg}$ was calculated in two conditions, under the hypothesis of complete creep reversal according to Eq. (1.67) and under the hypothesis of partial creep reversal according to Eq. (1.71) with the creep reversal parameter C_R. The same test conditions of the CFCG specimens have been reproduced through a Matlab script that applies the superposition model. The results in terms of crack propagation as a function of time are shown in Fig. 2.37. As expected the creep-fatigue superposition model based on the assumption of complete creep reversal is less conservative than the one based on the creep reversal parameter C_R. In fact, at $\Delta K_0 = 21.5$, 21.7, and 15.6 $MPam^{0.5}$ overestimates the time to rupture while the superposition model based on the partial interaction between creep and fatigue always underestimates the time to failure. The superposition model has no mechanistic explanation though and this explain why its application is still under discussion. However used in combination with the $(C_t)_{avg}$ definition based on C_R it was able to provide conservative solutions at all the load conditions and thus its extension to model the residual life of pressurized pipes is now possible.

2.7 J_{IC} Tests

Fracture toughness tests have been performed in order to identify the plastic collapse limit of the P91 material at high temperature. The procedure applied to identify J_{IC} follows the indications contained in the ASTM E1820-11 standard [17]. This standard identifies two possible procedures: the resistance curve method and a basic procedure based on a multi-specimen approach. The resistance curve method turned out to be not reliable to identify J_{IC} at elevated temperatures. A basic procedure was applied in order to reduce the scatter in crack size measurement and consequently in J_{IC} estimations.

2.7.1 J_{IC} Tests Experimental Setup

The geometry used in J_{IC} experimental tests is represented by a C(T) specimen where the crack opening displacement (COD) is measured at the load-line as shown in Fig. 2.38. The C(T) specimens knife edges were modified from the original design with a 7 mm diameter hole in order to accommodate the extensometer without any tight fit. The basic procedure for measurement of fracture toughness provides room temperature pre-cracking in order to achieve a sufficient sharp initial notch. Since no thermocouples were used during the tests, a temperature calibration was performed with the same procedure already described in Sec. 2.5.1. In order to respect the standard requirements for initial and final crack length, side grooves were machined after pre-cracking. As first trial, the J_{IC} was calculated according to the multi-specimen approach. This procedures uses one specimen to define a complete resistance curve. A specimen is loaded at a constant load-line displacement rate until a predefined COD level. During this loading ramp, at determined COD levels, the specimen is unloaded and reloaded in order to evaluate the crack size through the elastic compliance method. Each unloading/reloading sequence represents a point in the J-Resistance curve. However this method has proved to provide unreliable results when 4 specimens were tested. The load-COD curve of Fig. 2.39a) and b) shows that at low COD rates, the specimen reaction to unloading and reloading phase is affected by stress relaxation without allowing a relevant crack estimation by means of elastic compliance. When crack propagation is not evaluated correctly, the J-Resistance curve exhibits a significant scatter that does not guarantee an accurate J_{IC} estimation. The basic procedure overcomes this issue by testing multiple specimens at different final COD levels. During this tests, the specimen is monotonic loaded until the end of the test. The COD rate during loading was 0.6 mm/min. After brittle break in liquid nitrogen, the initial and final crack sizes are measured at 9 points and used to evaluate the J-Δa data point. According to this procedure six specimens were tested until the final COD levels COD_f reported in Tab. 2.18

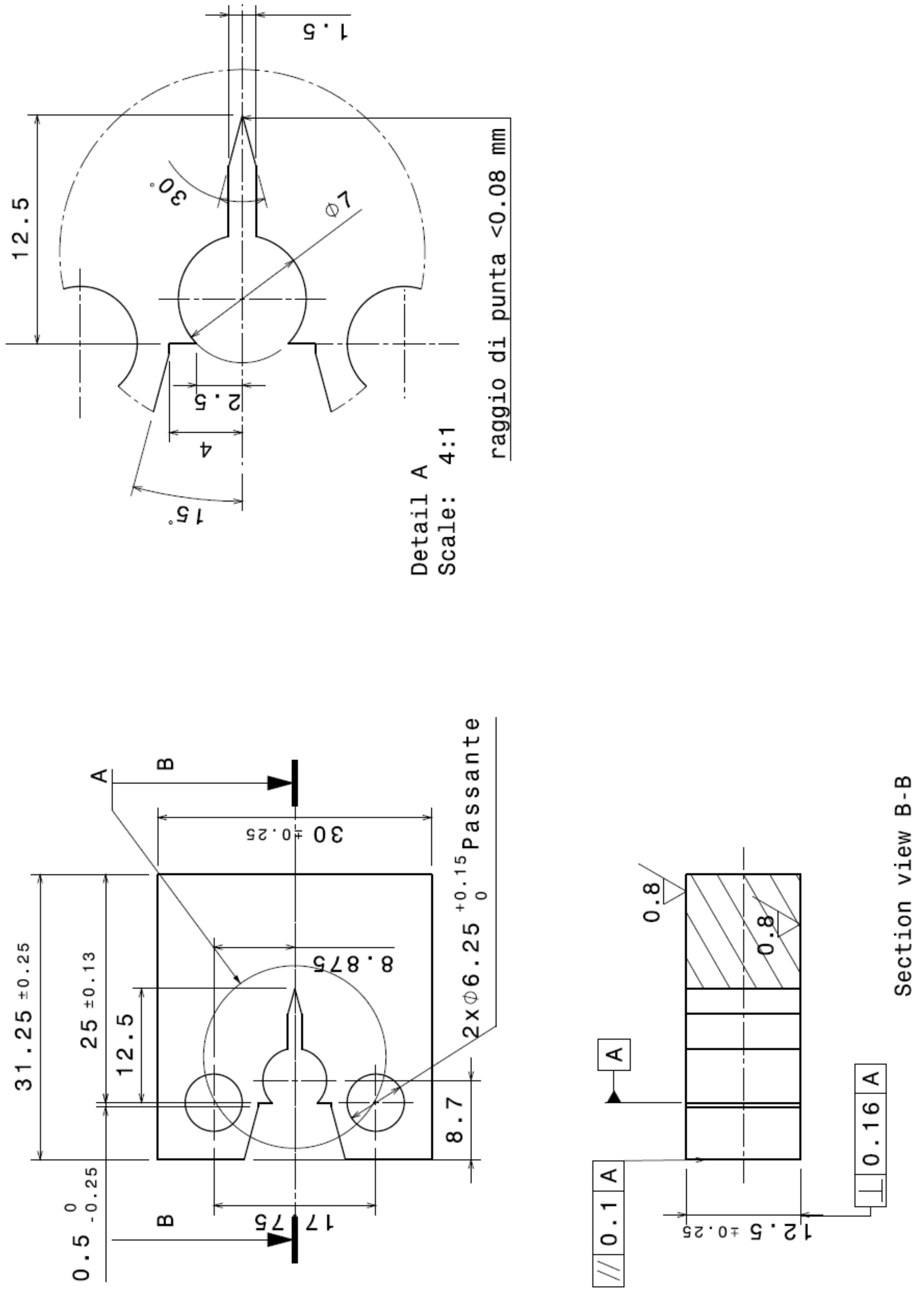

Figure 2.38: *C(T) specimen used for fracture toughness tests.*

together with the initial crack size a_0, the crack propagation during the test Δa and the final value of J. The initial and final crack sizes of Tab. 2.18 have been calculated according to the optical images of Fig. 2.40

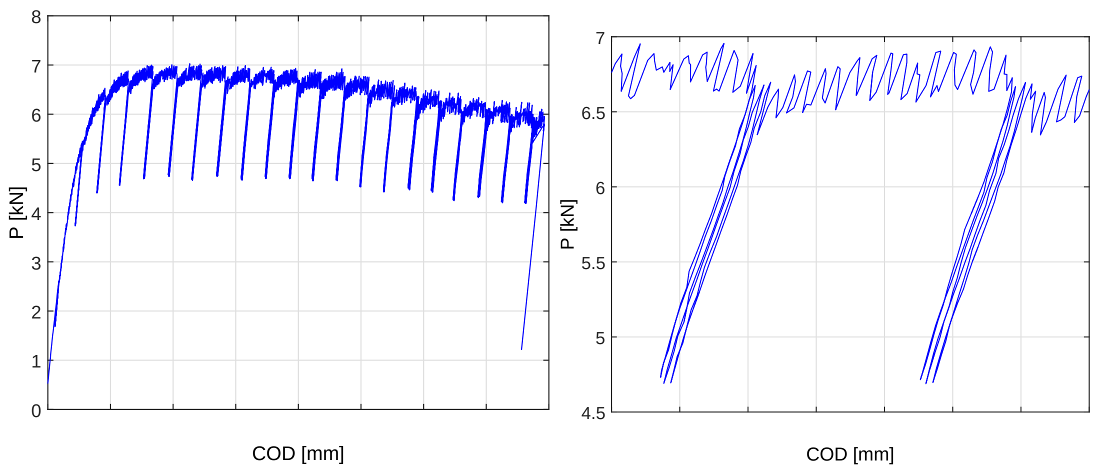

Figure 2.39: *Load vs. COD curve of one P91 C(T) specimen tested with the resistance curve method at 600 °C.*

Table 2.18: *J_{IC} tests matrix of P91 at 600 °C.*

Specimen	COD_f [mm]	a_0 [mm]	Δa [mm]	J [N/mm]
P91-J06	3.25	16.21	1.51	
P91-J04	3.00	14.70	1.30	
P91-J05	2.50	14.74	1.01	
P91-J01	2.00	14.73	0.71	
P91-J02	1.50	14.72	0.49	
P91-J03	1.00	14.72	0.23	

2.7.2 J_{IC} Test Results

The load vs. COD curves of all the J_{IC} tests performed according to the basic procedure are shown in Fig. 2.41. All tests exhibit a similar behavior without an excessive scatter in the measured load. The J integral is represented by a function of the area under the load-COD curve A_{pl} plus its elastic component J_{el} defined as:

$$J_{el} = \frac{K^2(1-\nu^2)}{E} \tag{2.11}$$

The obtained J integral is plotted as a function of the crack propagation obtained at the end of the test in Fig. 2.42. The data points highlighted by a plus marker have been used in the J fitting procedure as described in ASTM E1820 [17]. This procedure fits a power law to the J-Δa dataset:

$$J = C_2 \left(\frac{\Delta a}{k}\right)^{m_2} \tag{2.12}$$

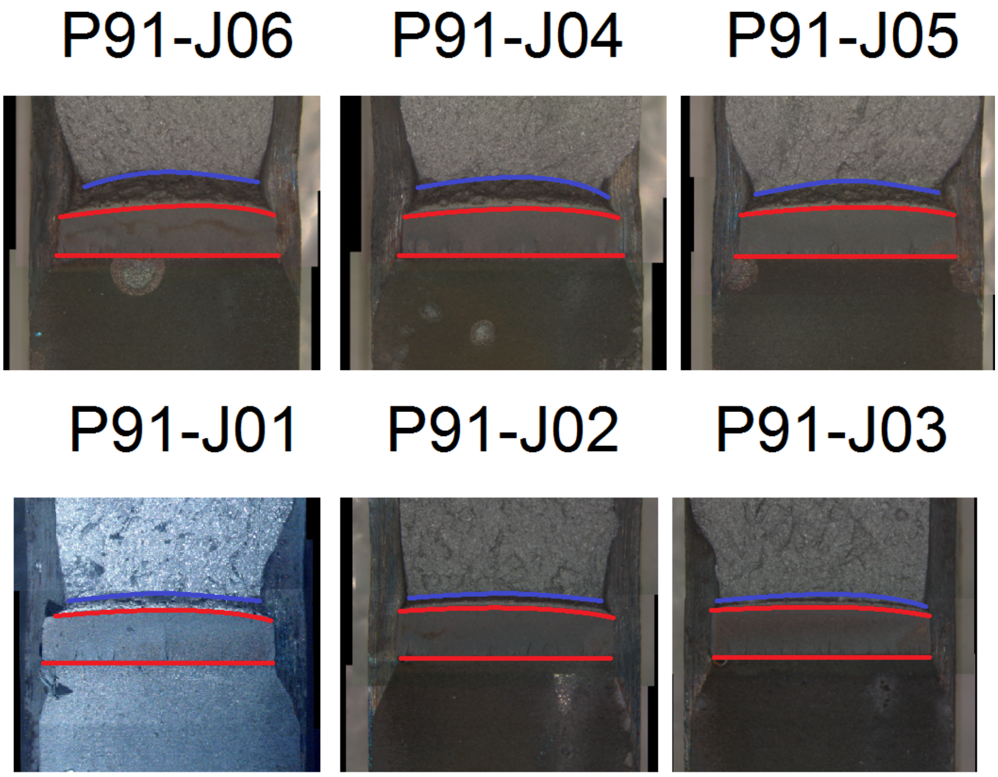

Figure 2.40: *Initial and final crack front size of C(T) specimens tested for fracture toughness according to the basic procedure.*

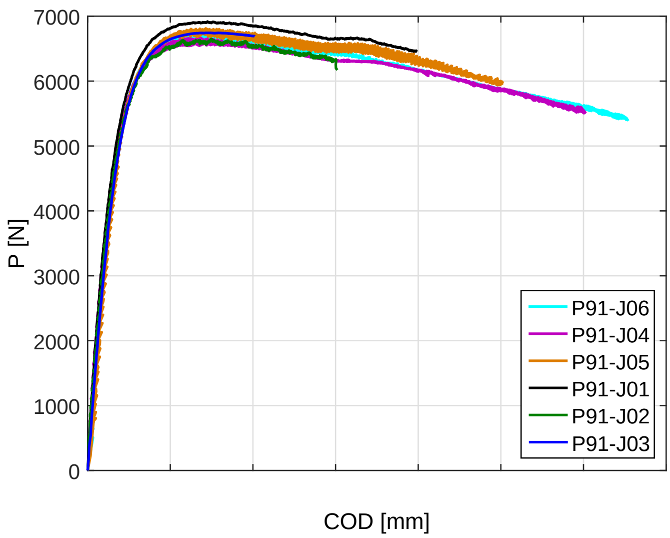

Figure 2.41: *Load vs. COD curves of P91 tested at 600 °C.*

with $k = 1$ mm. The results obtained during this fitting procedure are reported in Tab. 2.19. The interception between the fit shown in Fig. 2.42 and the green 0.2 mm offset line gives the value of $J_{IC} =$ [N/mm] that corresponds to a stress intensity factor $K_{IC} =$ MPa m $^{0.5}$.

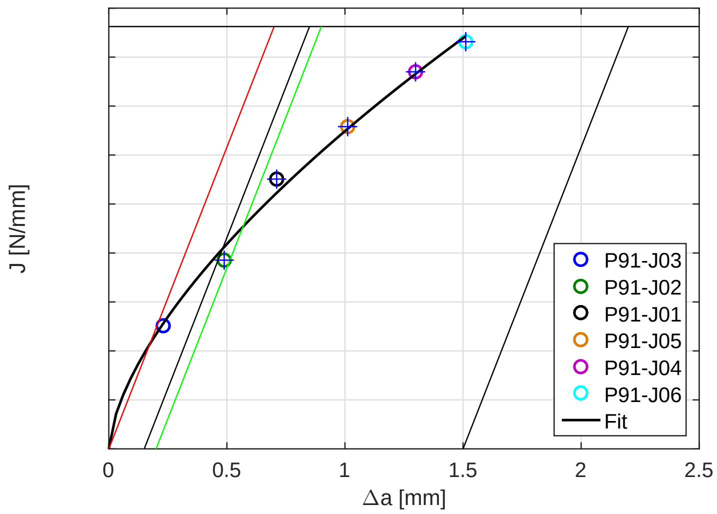

Figure 2.42: *J integral as a function of the crack propagation during the tests for P91 at 600 °C.*

Table 2.19: *J-Δa fit coefficients.*

C_2 [N/mm]	m_2

2.7.3 Numerical Validation with Key-Curve Method

The J_{IC} value obtained with experimental fracture toughness tests has been verified by investigating a numerical technique called Key curve method that was developed by Joyce et al. [33]. This method assumes that the load P in a fracture toughness test is a function of crack size a/W and COD COD/W:

$$P = f\left(\frac{a}{W}, \frac{COD}{W}\right) \tag{2.13}$$

The function $f(a/W, COD/W)$ is the key curve and can be determined numerically and experimentally. The numerical key curve method is illustrated in Fig. 2.43 where several load-COD curves obtained by numerical simulations at different stationary crack sizes intercept an experimental test record. These intersections can be used to estimate the crack size at a determined load P of the experimental data. With this procedure, starting from one test a complete J-Resistance curve can be extrapolated. With this aim, a numerical plane model of the C(T) specimen was studied with the FE software Abaqus. Because of symmetry only half of the specimen was studied as in Fig. 2.44. The elastic-plastic properties of Sec. 2.1 were applied to the model as well as a mesh of quadratic plane strain elements. Close to the crack tip, the mesh was refined to an average element size $L_{el} = 50\mu m$ according to Fig. 2.45. Different initial crack sizes were studied and compared with the experimental data as illustrated in Fig.

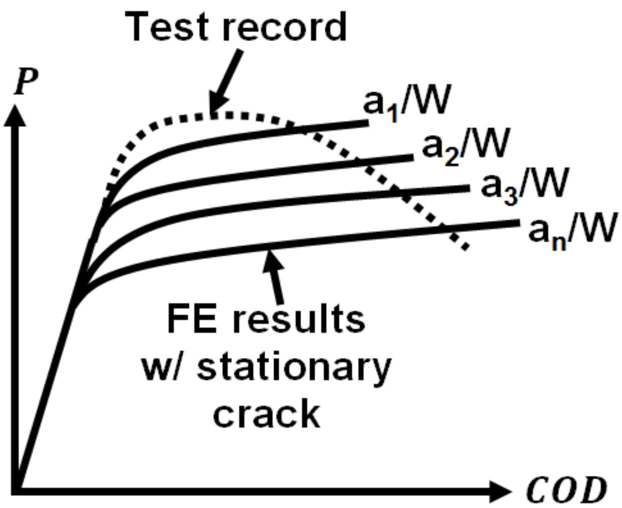

Figure 2.43: *Schematic diagram of the key curve method.*

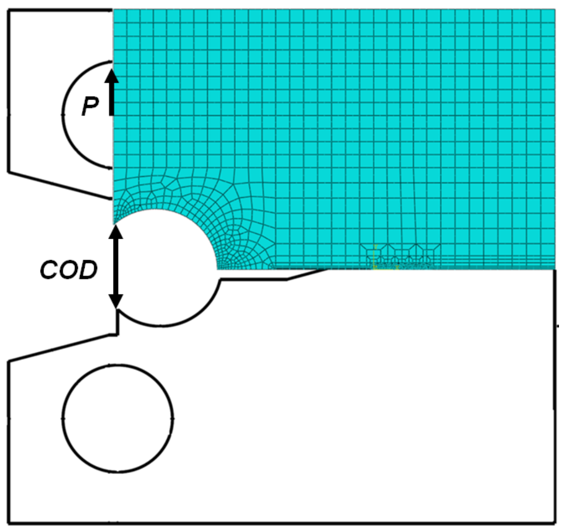

Figure 2.44: *FE model of the C(T) specimen for the key curve method application.*

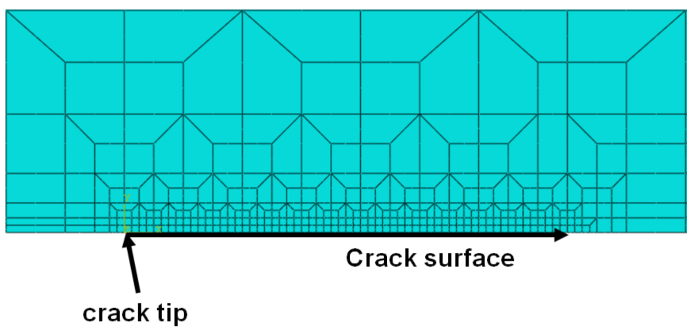

Figure 2.45: *Detail of the mesh close to the crack tip.*

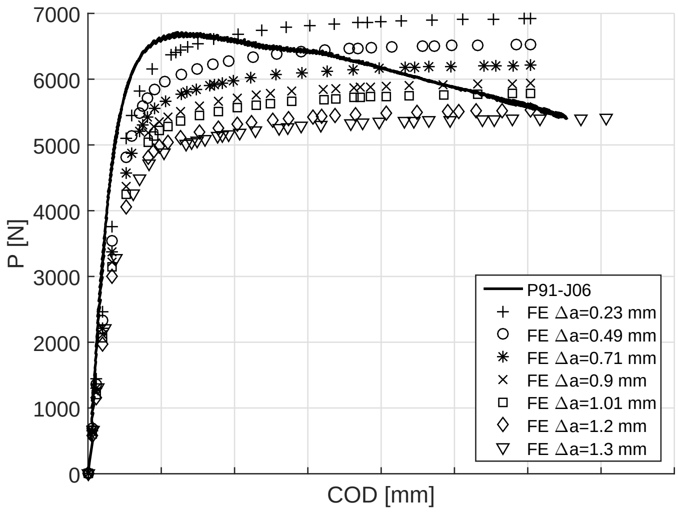

Figure 2.46: *Key curve method applied to evaluate P91-J06 J-Resistance curve from experimental data.*

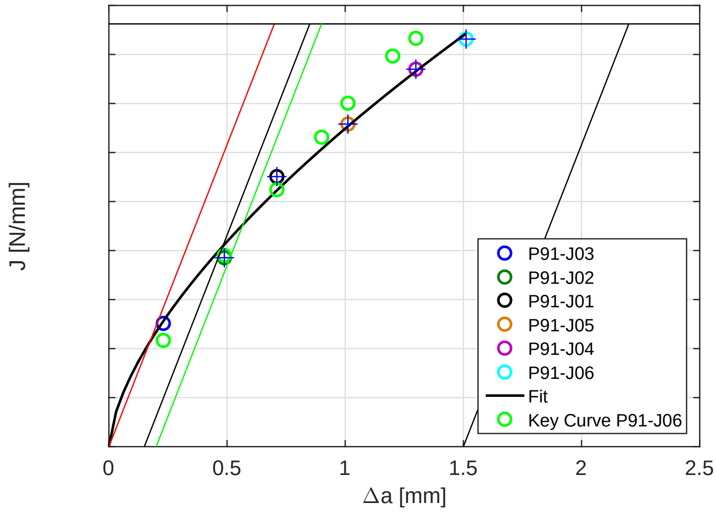

Figure 2.47: *$J - \Delta a$ curve obtained from the key curve method and comparison with the experimental J-Resistance curve for P91 at 600 °C.*

2.46. The intersection with the FE curves with the test record allowed the estimation of the J-Resistance curve shown in Fig. 2.47 that is compared with the one obtained experimentally. The J_{IC} value obtained by performing this procedure is N/mm and corresponds to a critical stress intensity factor $K_{IC} =$ MPa m$^{0.5}$. This value is similar to the one obtained experimentally although the results of the FE simulations exhibit a $J - \Delta a$ curve steeper than the experimental data. This might be due to the fact that the COD rate during experimental tests was not sufficient to exclude any creep strain contribution in the final results.

2.8 Summary

In this Chapter a deep characterization of the material properties of a modified P91 was presented. Starting from the results of high temperature tensile tests and uniaxial creep tests kindly provided by Tenaris, it was possible to estimate the high temperature elastic-plastic properties and the Norton power law constants according to Eq. (1.1). These last parameters were fundamental for an estimation of the crack tip parameters C^* and C_t deriving from experimental crack propagation and load-line deflection records of CCG tests performed at different initial stress intensity factors. The two parameters describe the crack propagation rate in EC and SSC conditions respectively according to a power law trend.
A similar procedure was performed to estimate the crack tip parameter $(C_t)_{avg}$ from CFCG tests performed at different initial stress intensity factor ranges and hold times. With the purpose to analyze the creep-fatigue propagation as a superposition of time-dependent and fatigue propagation, FCG tests have been performed at different frequencies and load ratios. The obtained coefficients of the Paris-Erdogan law that relates the crack propagation per cycle to the stress intensity factor range, have been used to assess the reliability of the superposition law that is nowadays the most common approach to model CFCG in calculation codes. With this purpose, with the superposition model that combines the Paris-Erdogan law and the $(C_t)_{avg} - (da/dt)_{avg}$ relation, the CFCG tests were simulated under the hypotheses of full creep reversal and partial reversal thanks to the C_R parameter that was estimated experimentally from the load-line deflection records of the experimental tests. The predictions based on the $(C_t)_{avg}$ estimation by means of C_R produced the most conservative solutions and thus the same approach will be used in the following pipe assessments of Ch. 3.
In order to verify the limit load of plastic collapse of cracked components, the J_{IC} parameter was determined from high temperature fracture toughness tests performed according to the basic procedure approach that involves the testing of multiple specimen to identify a single J-Resistance curve.
Lastly, by analysing with SEM the crack tip damage of the tested CCG and CFCG specimens, the fracture mechanisms occurring at high temperature in presence of stress intensification due to cracks, have been investigated. In both CCG and CFCG conditions, cracks propagate after voids growth and coalescence that leads to microcracks formation. The density of these voids is proportional to the time permanence at high temperature and the stress range.

CHAPTER 3

Residual Life Estimation of Pipe Components

This Chapter aims to transpose the crack tip parameters defined in Ch. 2 to more complex components, in order to study the standard code procedures to assess the acceptability of flaws in pressurized pipes.
In creep crack growth assessments, the application of experimental correlation between crack growth rate and C^* or C_t parameter is discussed. It is shown that, when material properties extracted from experimental data performed on the examined material are considered, the quality of the assessments is improved and in some particular conditions, the residual life estimation for the components might increase.
In order to address the lack of available standard codes that actually deal with interactions between creep and fatigue, rather than approaching the phenomenon with a simple superposition law, the $(C_t)_{avg}$ parameter associated to CFCG is introduced, under the hypothesis of partial creep strain reversal based on the creep reversal parameter C_R. With this approach a crack tip parameter, that accounts for small-scale creep, is introduced in the creep-fatigue crack propagation assessment.

3.1 Standard Assessment Procedures for Components

In the past years, different organizations have developed assessment procedures to determine the acceptability of flaws in pipe components operating at high temperatures.

The life prediction design of components in presence of defect is strongly dependent on material's uniaxial creep data in terms of temperature, stress, steady-state creep strain rate and failure time. However, experimental tests covers a limited range of failure times (until $t_R = 10^5$) while power plant components are designed to operate for longer. A crack growth assessment extrapolates experimental data on specimens to actual pipe components with sufficient reliability in order to guarantee a conservative residual life estimation.
The crack tip parameters C^* and $C(t)$, that have widely been used to describe crack propagation rates for several testing specimen geometries, characterize the material's behavior in a specific temperature T and load condition and thus they are independent from the geometry that is considered. This means that they are theoretically applicable also with actual components. However, they strictly depend on the load-line deflection values that are not always easily measurable. In a pressurized pipe for example, the triaxial stress state makes difficult to estimate of a proper load-line. Also measurement system can not be the same used for testing specimens.
Moreover, according to these standards, the resistance properties are given depending on material classes that often include material of same chemical composition but of different creep, creep-fatigue damage.
Among these assessment procedures it is worth mentioning the:

- EDF Energy R5 [10],
- BS 7910 [12],
- API 579-1/ASME FFS-1 [5], and
- FITNET [24]

The more recent between these standards is the EDF Energy R5 [10] that was updated in 2014. It covers cracked bodies that are subject to creep conditions in volumes 4 and 5. The creep and creep-fatigue crack propagation is based on the time dependent failure assessment diagram (TDFAD) that evaluates for a predefined amount of time whether an hypothetical defect propagation will occur or not. It recognizes two main failure mechanisms, one given by material creep toughness and the other given by plastic collapse. The first is given by the stress intensity factor that produces the supposed crack propagation in the assessed time while the latter identifies a limit load that brings to plastic collapse the entire ligament section. Creep-fatigue conditions are modelled by superposing the creep and fatigue damages. The supposed crack propagation that is going to be verified is reduced by a portion associated to pure fatigue crack propagation. As expected, this approach might over simplify the issues related to creep-fatigue

interactions presented in Sec. 1.2 although it is considered conservative and does not affect the assessment reliability.
Another calculation standard that recognizes and shares some approaches of R5 [10] and Fitnet [24] is the british standard BS 7910 [12]. The proposed CCG assessment defines a strategy, to evaluate the C^* parameter in pipe components, based on the concept of reference stress under the hypothesis that steady state creep generates a uniform stress distribution. In CFCG regime, it recalls the TDFAD concept of R5 [10], superposing creep and fatigue crack growth separately. In both R5 and BS 7910 the creep and fatigue properties are defined according to specific material classes, when no experimental data performed on the assessed material are available. Each class correspond to materials with similar chemical composition and creep-fatigue resistance properties.
The CCG approach contained in Part 10 of API 579 [5] considers the combination of two damages, one before crack initiation i.e. a crack propagation of 0.2 mm, and another after crack initiation. The damage before crack depends on rupture data defined with the Larson-Miller parameter [38] from uniaxial creep tests, while the damage after crack is calculated by using specific formulations of C^* and C_t parameters, always based on the reference stress. The creep-fatigue damage is modelled by simple superposition of creep and fatigue damages, and the acceptability criteria is given as a sort of safety coefficients that shall not be exceeded. API 579 suggests the use of experimental data performed on the material that is going to be assessed. However, when these are not available, strongly suggests the use of the MPC Project Omega Creep Data [42], a database that defines the creep properties of 23 classes of materials. Although a different approach is proposed, API 579 refers to R5 and BS 7910 and recognize them as alternative procedures.
FITNET [24] is part of a European project that finished at the end of May 2006. It covers fracture, fatigue, creep, and corrosion. The assessment of components operating in creep conditions is contained in part 8, and splits the calculation procedure in two parts that model creep crack initiation (CCI) and CCG. In order to assess CCI FITNET identifies two possible approaches: the TDFAD proposed by R5 and the two criteria diagram (2CD) by Edwald et al. [31]. The 2CD attributes initiation to three main damages: ligament, mixed mode, and crack tip. These damages are strictly related to the Larson-Miller parameter, the stress intensity factor at initiation of CCG tests, and the rupture stress at the assessment temperature all calculated based on the reference stress definition. Creep crack growth is modelled through a definition of the C^* for the pipe components based on the reference stress. Also the FITNET procedure accepts the use of experimental data or, in case they are missing, creep resistance data based on different classes of materials based on the chemical composition. Once again the

creep-fatigue interaction, when significant, is modelled through a simple superposition of the crack propagation due to creep and fatigue.
Although each procedure considers different approaches to model the creep and creep-fatigue crack propagation in components operating at high temperatures, one thing that is in common is the morphology of the possible defects that are defined according to Fig. 3.1. Crack is supposed to present a semi-elliptical or elliptical shape, when not

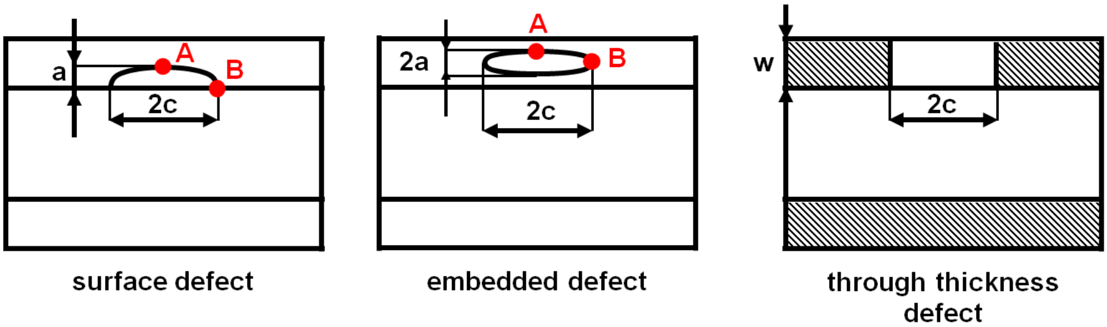

Figure 3.1: *Pipe crack morphology according to assessment standards.*

passing trough the wall thickness. Another important aspect that is treated in common for each standard is the assessment that is performed by evaluating two main regions of the crack surface identified as the A and B red dots of Fig. 3.1, that represent the plane strain and plane stress conditions respectively. By evaluating the crack propagation rate in these regions it is possible to estimate the crack shape evolution during the assessment time. This is important for a reliable assessment as the crack tip parameters, the reference stress, and the stress intensity factor directly depend on the ratio $a/(2c)$ between these two regions.

3.2 CCG Prediction

In this section an assessment procedure [2] based on the combination of the two criteria diagram (2CD), as suggested by FITNET [24] and the BS 7910 [12] C_{ref} model, is evaluated in order to model CCI and CCG in pipes subject to internal pressure, in presence of semi-elliptical longitudinal cracks on the inside surface. For the P91 grade steel under examination, the relationship between stress, temperature, and rupture time was given according to the Larson-Miller parameter previously introduced in Sec. 2.1. In order to describe the steady-state creep strain rate for the component, the Norton law relationship of Fig. 2.5 was used. The coefficients used in the assessment are the one reported in Tab. 2.3 for low and high stresses fit. The creep crack initiation data of CCG tests were used in the 2CD to estimate the time needed to the pipe component to present a crack propagation of 0.2 mm under plane strain conditions. With this purpose the relationship between the experimental values of stress intensity factor and time at initiation of Fig. 2.12, were modeled according to the fitted power law coefficients of Tab. 2.5. The creep crack growth rates for the pipe geometry were characterized according to the crack tip parameter C^* under the hypothesis that steady-state creep occurs prior to creep crack initiation after a complete stress redistribution on the ligament region close to the crack tip. Equation (1.19) that defines the creep crack growth (da/dt) as a function of the C^* based on experimental data, was modified in relation to material's multiaxial creep ductility ε_f^* according to the BS 7910 procedure [12] as follows:

$$\frac{da}{dt} = \frac{3 \cdot (C^*)^{\frac{n}{n+1}}}{\varepsilon_f^*} \tag{3.1}$$

In this assessment, the crack propagation was evaluated in two different locations of the crack front characterized by plane strain and plane stress conditions (point A and B of Fig. 3.3 respectively). According to Maleki et al. [45] the multiaxial ductility ε_f^* is equal to uniaxial ductility ε_f in plane strain conditions and equal to 1/7ε_f in plane stress conditions. A uniaxial creep ductility $\varepsilon_f = 0.25$ was derived as an average value from the creep tests of Sec. 2.1. This allows the evaluation of Eq. (3.1) under these two conditions and a comparison with the experimental data coming from CCG tests on C(T) specimens as shown in Fig. 3.2.

The first important observation is that the different slope of the predicted crack prop-

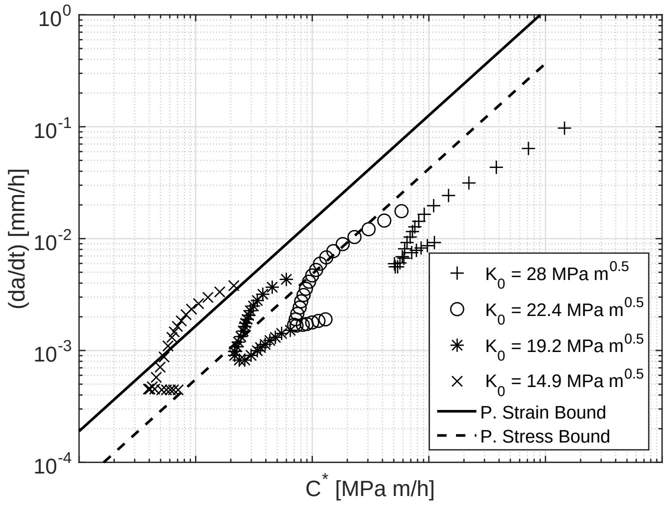

Figure 3.2: *Creep crack growth rate as a function of C^* parameter: comparison between the experimental tests and Eq.* (3.1).

agation rates versus the experimental ones demonstrating that this approach may be or not conservative depending on the range of the C^* parameter. In particular, for low C^*

values, typical of the average components operating conditions, may not be conservative.

Crack propagation in pipe components under creep conditions occurs similarly to testing specimens. The first stage is the time needed to crack initiation i.e. to propagate 0.2 mm. CCI is characterized by an accumulation of creep damage without a significant crack propagation. The second stage is characterized by steady-state creep conditions where crack propagation rate starts to increase leading to component failure. The accepted exposure time of a pipe component to 600 $°C$ is thus calculated as:

$$t_{\text{exposure}} = t_{\text{i}} + t_{\text{CCG}} \tag{3.2}$$

The data required in this proposed assessment are: operating conditions; geometry of the pipe and pipe's imperfection; creep and creep crack growth material data, which in this case were based on the same batch of material of the P91 used in power plants. The transferability of these data to multiaxial stress conditions is based on the concept of reference stress of the pipe primary load as defined in BS 7910 [12]. This approach works under the hypothesis that creep state, after stress relaxation, causes a uniform stress distribution along the ligament. Figure 3.3 shows the geometrical configuration of the pipe proposed as a case study for the application of this assessment procedure. A service temperature of 600 $°C$ and two pressure loads of 25 and 50 MPa were considered The 2CD was developed for the assessment of crack initiation in components

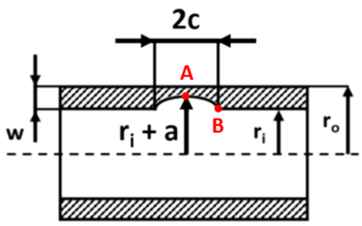

Figure 3.3: *Geometry of the defected P/T91 pipe proposed as case study.*

where ligament damage and crack tip damage are in competition among themselves, in determining the critical level of damage at the crack tip [23]. The 2CD of Fig. 3.4 shows that for each damage a different load parameter is considered. The nominal stress $\sigma_{n,pl}$, i.e the reference stress acting on the component, considers the stress situation along the ligament, while the nominal elastic stress intensity factor K_{Iid}, at a time zero, characterizes the condition at the crack tip. The nominal stress normalized with respect to the stress for creep failure at the assessment temperature identifies the stress ratio:

$$R_\sigma = \frac{\sigma_{n,pl}}{\sigma_R} \tag{3.3}$$

When the crack tip is considered, the nominal elastic stress intensity factor K normalized with respect to the stress intensity factor at initiation (K_{Ii}, in Fig. 2.12) identifies instead the stress intensity ratio:

$$R_K = \frac{K}{K_{Ii}} \tag{3.4}$$

The main difference between the two ratios is that R_K accounts for the presence of a defect in the assessed component while R_σ just take into consideration the creep effects on smooth specimens away from possible defects. The 2CD defines three mechanisms of damage responsible of crack initiation. A low value of $K/\sigma_{n,pl}$ is an indication that the crack initiation is due to widespread damage in the ligament section while a high ratio $K/\sigma_{n,pl}$ instead, indicates that the crack initiation is due to localized damage at the crack tip. The region between the two extremes of Fig. 3.4 accounts for damages interaction defining a mixed damage mode. Creep crack initiation is verified when the assessed point lies above the blue limit line of Fig. 3.4. In Fig. 3.4 diagram, the initial

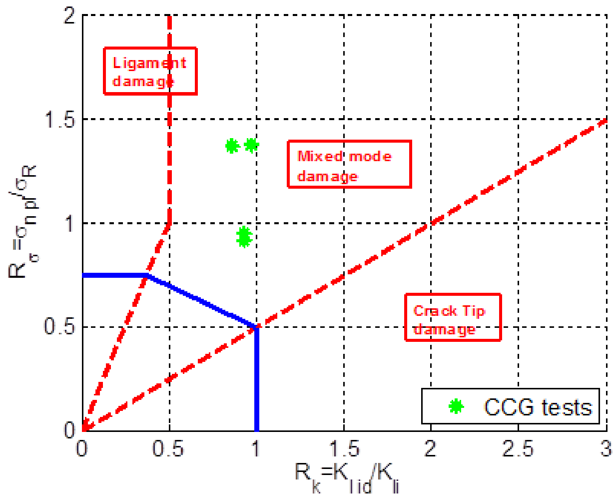

Figure 3.4: *Two criteria diagram for crack initiation time calculation.*

conditions of the CCG tests are evaluated according to the 2CD exhibiting a mixed mode damage failure given by a reference stress higher than the creep rupture stress and a nominal stress intensity factor close to the value at initiation.
For the pipe component of Fig. 3.3 the 2CD was applied by calculating:

- the time corresponding to the boundary line of the ligament damage zone. This time was calculated as the rupture time t_R evaluated according to the Larson-Miller parameter for an hypothetical rupture stress σ_R defined in relation to the nominal stress as $\sigma_{ref}/0.75$;

- the time corresponding to the boundary line of the crack tip damage zone. This limit time is calculated by reversing the power law relationship of Eq. (2.4) at the nominal stress intensity factor K_{Iid} for the component that was calculated according to the FITNET [24] procedure. The power law coefficients used in this assessment are the one reported in Tab. 2.5;

- the time corresponding to the boundary line of the mixed mode damage. This calculation requires an iterative procedure where the assessment time t_A is changed progressively. Each time t_A corresponds to a Larson-Miller parameter calculated according to Eq. (2.1). From the Larson-Miller parameter the equivalent rupture stress σ_R is calculated. The ratio $R_\sigma = (\sigma_{ref} = \sigma_{n,pl})/\sigma_R$ can now be calculated and plotted together with its analogous R_K point evaluated as the ratio between the nominal stress intensity factor K and the stress intensity factor at initiation time with $t_i = t_A$ according to Eq. (2.4). When the data point exits the acceptability area, the mixed mode initiation time is found.

The minimum of the three initiation times calculated corresponds to the time for a creep crack growth of 0.2 mm. The results are summarized in Tab. 3.1, for a operating pressure of 25 MPa and different initial defect sizes according to Fig. 3.3.

As seen in Fig. 3.2, where the experimental data of crack initiation are reported

Table 3.1: *Summary of the predicted initiation time for each type of damage and for each imperfection size of Fig. 3.3. The actual initiation time for each defect size is in underlined format.*

Imperfection size	Ligament damage	Mixed mode damage	Crack tip damage
5% w	38251 h	20880 h	513285 h
10% w	38251 h	12981 h	124511 h
12.5% w	38251 h	10745 h	76116 h

for CCG tests, this approach is expected to be conservative at nominal stress intensity factors within the range of the experimental tests. However it still needs to be verified at lower stress intensity factor applications.

After CCI was obtained through the 2CD, CCG was evaluated according to the crack tip parameter C^* by taking advantage of its linear trend with the creep crack propagation rates. The C^* parameter for the pipe geometry was calculated based on the reference stress σ_{ref} according to Eq. (3.5)

$$C^* = \sigma_{ref}\dot{\varepsilon}_{ref}\left(\frac{K}{\sigma_{ref}}\right)^2 \tag{3.5}$$

where $\dot{\varepsilon}_{ref}$ is the reference strain rate defined in the Norton creep law of Eq. (1.1) by using the high and low stresses fits reported in Tab. 2.3, K is the stress intensity factor evaluated at a time t for a crack of size a and $2c$ subject to a reference stress

σ_{ref} calculated from the formulation by Sun et al. [53]. Fig. 3.5 illustrates the crack propagation evolution with time until the maximum acceptable size, that in this work was set equal to the 85% of the wall thickness w, is reached. The plotted results were carried out for a low loading case (25 MPa of internal pressure) and mean trend of the material reported in Fig. 2.5. In all the three crack configurations, the admissible exposure time was higher than 10^5 hours. The reference stress approach of Eq. (3.5)

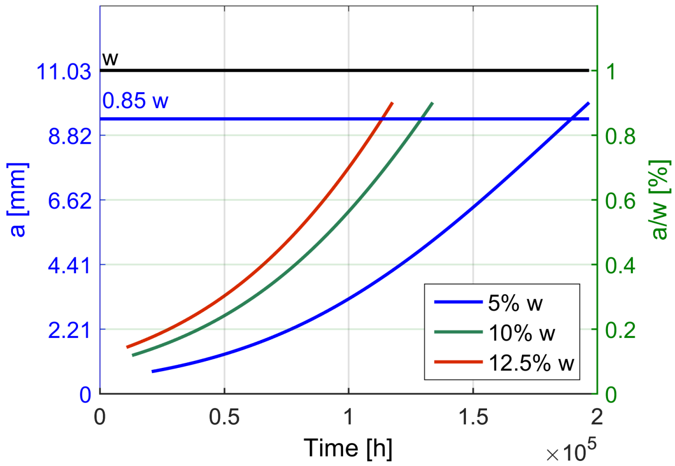

Figure 3.5: *Crack propagation versus time for geometry and imperfection size of Fig. 3.3.*

is valid under the hypothesis that the damage for the component is evaluated as the damage in uniaxial tests. Different expressions of the reference stress based on the plastic collapse definition led to a significant change in the results in terms of residual life estimation. Fig. 3.6 e.g. reports the crack evolution for an initial defect size of $5\%w$ when different reference stress global and local approaches [11], were applied. It might be worth noting that the C^* estimations deriving from different σ_{ref} expressions are higher than the definition of Sun [53] resulting in faster crack propagation rates. This represents another source of uncertainty in the application of the standardized procedures for components assessment.

The case study was also analyzed according to the assessment code API 579 [5], where the creep crack propagation rate is defined depending on the C_t parameter:

$$C_t = C^* \left[\left(\frac{t_{\mathrm{T}}}{t} \right)^{\frac{n-3}{n-1}} + 1 \right] \tag{3.6}$$

reminding that t_T is the transition time from small-scale to steady-state creep. According to this approach the C^* integral is calculated with an expression similar to Eq. (3.5):

$$C^* = \frac{\dot{\varepsilon}_{ref}}{1 - D_{BC} - D_{AC}} \left(\frac{K^2}{\sigma_{ref}} \right) \tag{3.7}$$

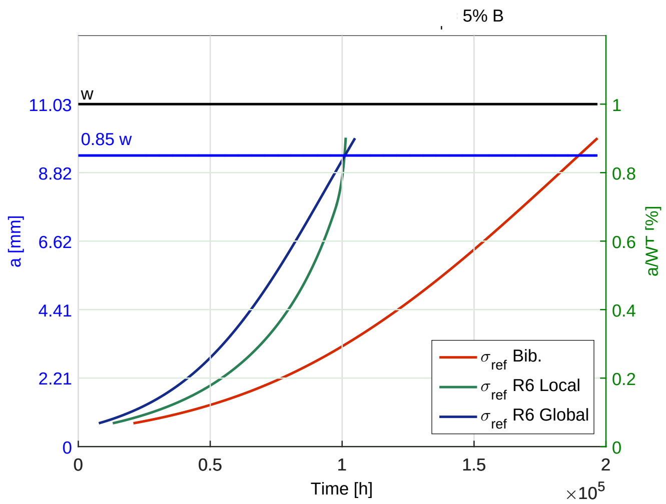

Figure 3.6: *Crack propagation versus time for imperfection size equal to 5% w and different methods to evaluate σ_{ref}. Bib. refers to [53].*

where D_{BC} and D_{AC} are the damage before and after cracking respectively, obtained by the application of the MPC Omega project method [42] that was developed from the examination of creep resistance properties of different materials. This method defines the time to failure and creep strain accumulation as a function of stress, temperature, and load conditions. The residual life of a pressurized pipe in presence of defect is calculated from the C_t parameter using Eq. (1.62) with the calibration coefficients D' and ϕ' given by the MPC Omega project [42]. The creep crack growth rate correlation with the C_t parameter provided by the MPC Omega project is compared with the experimental data of CCG in Fig. 3.7. As for the C_{ref} approach, the prediction according to the MPC Omega project, results conservative at high C_t values while at low C_t values, in the typical range of power plant components, it might produce non conservative estimations with respect to the experimental results. The coefficients of the 9Cr1MoV class of material reported in the standard were used to represent the creep damage on the modified P91 steel. Figure 3.8 a) and b) shows the crack propagation predicted according to API 579 code [5] for an initial defect size equal to $5\%w$ for the two pressure conditions of 25 and 50 MPa. As foreseen by standard, lower and upper bound were calculated to account for material's scatter band. The same case study in terms of initial crack size, load conditions, and scatter band was recalculated with the proposed model according to Eq. (3.5) leading to the results reported in Fig. 3.9 a) and b). It is interesting to note that the predictions based on the proposed model of Eq. (3.2) are in good agreement with the API 579 [5] residual life estimations, for low stress conditions that are intended to represent the actual operating conditions of power plant components. In high pressure conditions instead, the API 579 prediction resulted to be

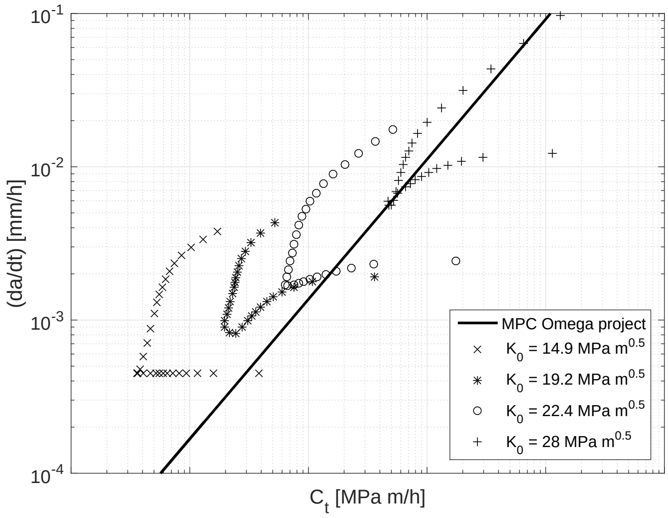

Figure 3.7: *Comparison between the (da/dt)-C_t relationship of the experimental CCG tests and the MPC Omega project.*

more conservative with respect to the Eq. (3.2) model. However the scatter bands of Fig. 3.8 a) and b) highlight the importance of having a reliable creep database based on the investigated material as well as CCG data to improve the residual life estimations. In this context, a reduction in the predicted life time by a factor of 2 can be observed for both low and high loading conditions. Moreover a degree of uncertainty is still present, due to: the application of the 2CD to predict crack initiation; the use of the reference stress concept to calculate the crack tip parameter C^* or C_t; the use of standard defined relationship between the crack growth rates and the crack tip parameters.

3.3 CFCG Prediction

This section deals with the definition and verification of an assessment procedure based on the combination of different approaches in order to predict creep fatigue crack initiation and growth in pressurized pipes with a longitudinal flaw on the inside surface. The following calculation codes strongly rely on material data that have been collected during this work and therefore are expected to produce a more accurate prediction of the creep fatigue behavior for the P91 steel. Creep-fatigue crack initiation (CFCI) has been obtained by means of the Time Dependent Failure Assessment Diagram (TDFAD) contained in R5 code [10]. Creep-fatigue crack propagation instead was defined according to the crack tip parameter $(C_t)_{avg}$ [4] that accounts for transient creep conditions where creep and cyclic plastic damaged zones interact within each other. At high hold times it trends to the stabilized value C^*, typical of CCG condition. The relationship between the average crack propagation rate $(da/dt)_{avg}$ and $(C_t)_{avg}$ obtained from CFCG tests on

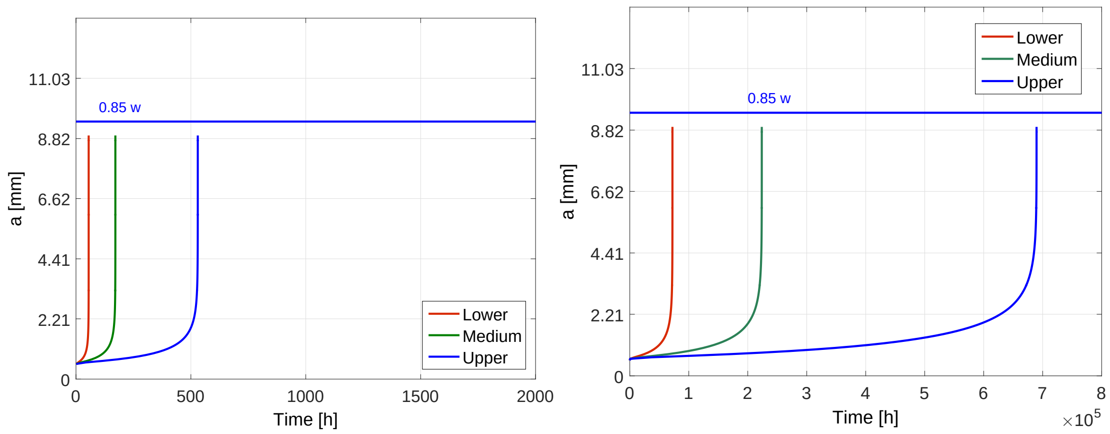

(a) *High Stresses.* **(b)** *Low Stresses.*

Figure 3.8: *Crack propagation versus time for imperfection size equal 5%w according to ASME/API Code [5].*

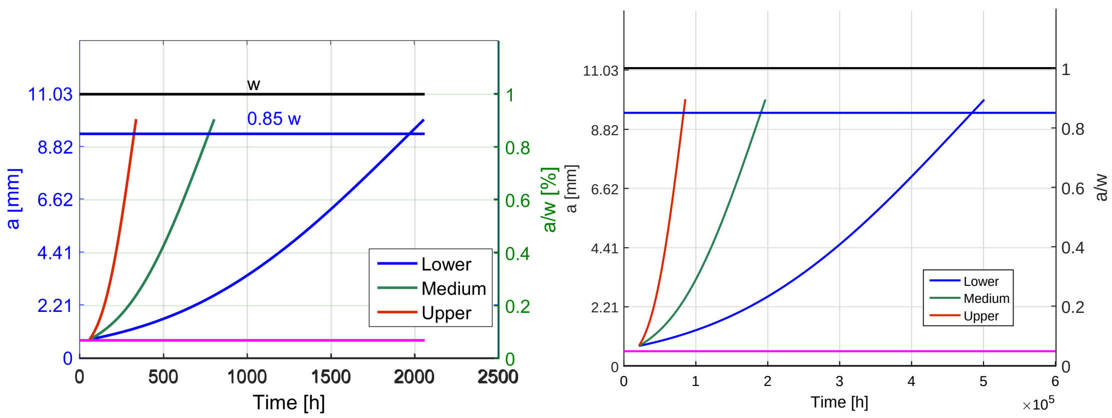

(a) *High Stresses.* **(b)** *Low Stresses.*

Figure 3.9: *Crack propagation versus time for imperfection size equal 5%w according to the BS 7910 model [12].*

C(T) specimens may be transposed to any kind of geometry for which a stress intensity factor can be defined.

3.3.1 CFCG estimation through the $(C_t)_{avg}$ approach

The crack tip parameter in creep-fatigue conditions is the $(C_t)_{avg}$ and since it represents the average value of the small scale creep parameter C_t during the hold time of a creep-fatigue test, it is supposed to represent crack propagation rate even during transients. For this reason it was used to predict CFCG in a pressurized pipe with an inside surface semi-elliptical shaped axial crack. As seen in Ch. 1.2, $(C_t)_{avg}$ can be estimated analytically under different hypothesis:

- Complete creep reversal, i.e. the fatigue cycle completely redistribute the stress field at the crack tip. In this case $(C_t)_{avg}$ is determined by the following equation expressed for a pipe component starting from Eq. (1.67):

$$(C_t)_{avg} = \frac{2\alpha_i\beta_0(1-\nu^2)}{E} F_{cr}(\theta, n)\frac{\Delta K^4}{w}\frac{F'}{F}(EA)^{\frac{2}{n-1}} t_h^{-\frac{n-3}{n-1}} + C^* \tag{3.8}$$

- No creep reversal, i.e. the hold time is long enough that the creep zone become dominant with respect to the cyclic plastic zone. In this case $(C_t)_{avg}$ is determined by the following equation expressed for a pipe component starting from Eq. (3.9):

$$(C_t)_{avg} = \frac{4\alpha_i\beta_0 F_{cr}(\theta, n)}{(n-1)Ew}(1-\nu^2)K^4\frac{F'}{F}(EA)^{\frac{2}{n-1}}(N\cdot t_h)^{-\frac{n-3}{n-1}} + C^* \tag{3.9}$$

- Interaction between creep and fatigue damages through the C_R parameter. In this case no assumption on the dominant damage mechanism is considered and the $(C_t)_{avg}$ definition for a pressurized pipe consists in the combination of Eq. (3.8) and (3.9):

$$\begin{aligned}(C_t)_{avg} =& \frac{2\alpha_i\beta_0 F_{cr}(\theta, n)}{Ew}(1-\nu^2)\Delta K^4\frac{F'}{F}(EA)^{2/(n-1)} \\ & \left[C_R + \frac{2(1-C_R)N^{-[(n-3)/(n-1)]}}{n-1}\right]\cdot(t_h)^{-[(n-3)/(n-1)]} + C^*\end{aligned} \tag{3.10}$$

where α_i has the same value of Eq. (1.46) with $\alpha_n^{n+1} = 0.69$ for $3 \le n \le 13$ and β is $1/3$ under plane strain conditions [8]. The angular function F_{cr} is estimated at different angles ϑ (eg. $\vartheta = 0°$ plane stress and $\theta = 90°$) and at different power law exponents n according to Riedel and Rice [29] (Fig. 1.9). With an average n value of 10 obtained from uniaxial creep data on the modified P91 and under plane strain conditions F_{cr} is equal to 0.3824. ν is the Poisson ratio and F' is the derivative of the shape function F that was calculated numerically according to the API RP 579 [5]

Table 3.2: *$h_1(a/W, n)$ values for C(T) specimens [37]: plane strain conditions.*

a/W	$n=1$	$n=2$	$n=3$	$n=5$	$n=7$	$n=10$	$n=13$	$n=16$	$n=20$
0.25	2.23	2.05	1.78	1.48	1.33	1.26	1.25	1.32	1.57
0.38	2.15	1.72	1.39	0.97	0.693	0.443	0.276	0.176	0.098
0.50	1.94	1.51	1.24	0.919	0.685	0.461	0.314	0.216	0.132
0.63	1.76	1.45	1.24	0.974	0.752	0.602	0.459	0.347	0.248
0.75	1.71	1.42	1.26	1.033	0.864	0.717	0.575	0.448	0.345
1.00	1.57	1.45	1.35	1.18	1.08	0.95	0.85	0.73	0.63

formulation. The average crack propagation rate $(da/dt)_{avg}$ is related to the creep-fatigue crack tip parameter $(C_t)_{avg}$ from the power law of Eq. (1.66). The values of D'' and ϕ'' used in the following assessments were chosen according to the values of Tab. 2.15 referred to the fit of CFCG tests performed on C(T) specimens where the $(C_t)_{avg}$ parameter was estimated by means of the creep reversal parameter C_R. Equations (3.8, 3.9) and (3.10) directly depend on the estimation of the stabilized value of the $C(t)$ integral, i.e. C^*, that, for this assessment, was calculated according to the BS7910 [12] C_{ref} approach based on the concept of reference strain rate $\dot{\varepsilon}_{ref}$ (Eq. (3.5)). After all the necessary parameters have been defined, it is now possible to evaluate the $(C_t)_{avg}$ and according to Eq. (1.66) the crack propagation rate. This procedure was included in a Matlab iterative script in order to assess the crack propagation rate during the entire operating life of a component subject to creep-fatigue. In order to validate the method, the model presented so far was applied to determine CFCG in C(T) specimens and compare the results with the experimental data. The formula of Eq. (3.10) was adapted to C(T) specimen by changing w with W and F'/F according to Eq. (2.8) [49]. A solution based on numerical simulations was used to determine the C^* of Eq. (3.10) in case of C(T) specimens. This solution is based on the work of Kumar et al. [37] that gives an analytical J-integral estimation. If the creep strain rate $\dot{\varepsilon}^c$ is considered instead of the plastic strain ε^p, J-integral becomes the crack tip parameter C^* as previously demonstrated in Eq. (1.18 a) with η_1 defined as per Eq. (1.17). The h_1 values estimated by [37] are reported for plane strain conditions in Tab. 3.2. When different values of a/W and/or n were considered, the values of h_1 were interpolated. The averaged stress constants of Tab. 2.3 were used to model CFCG according to the $(C_t)_{avg}$ model defined through the creep reversal parameter. The results in terms of creep-fatigue crack growth as a function of time are shown as dotted lines in Fig. 3.10 and compared with the experimental data (continuous lines). The time to failure of the C(T) specimens is well estimated for each test except the one performed at $\Delta K = 16.4$ MPa m$^{0.5}$ with $t_h = 1$ h which is overestimated. This is also shown in Fig. 3.11 where a comparison

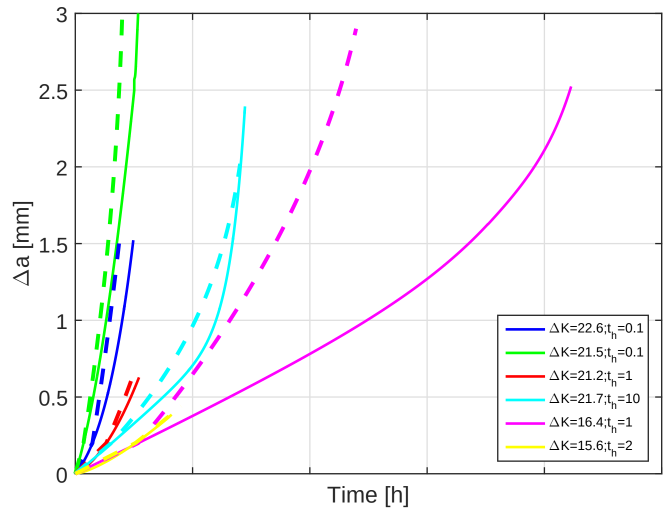

Figure 3.10: *CFCG model results for C(T) specimens and comparison with experimental data of P91 at 600°C.*

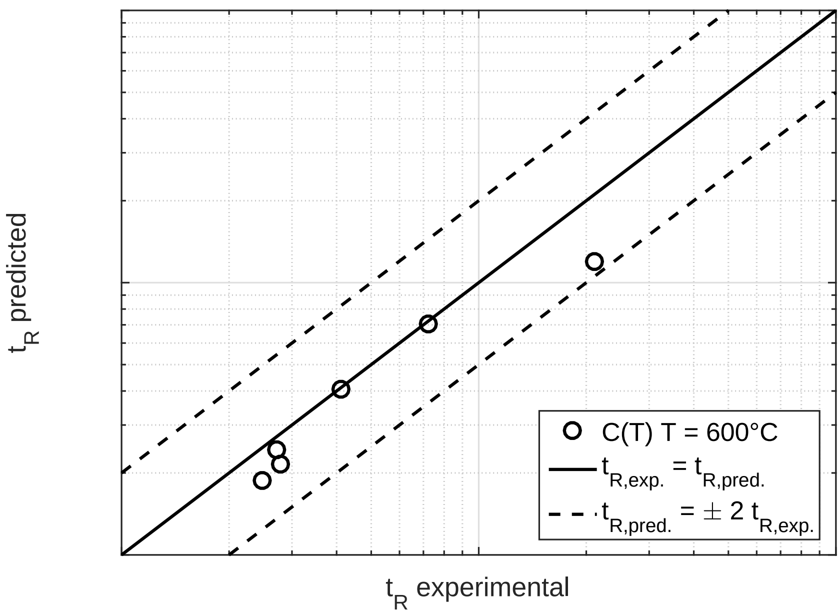

Figure 3.11: *Comparison of the predicted and experimental rupture times of C(T) specimens.*

between the experimental and predicted times to failure is shown.

3.3.2 CFCI estimation through the TDFAD approach

In this section the CFCI is modeled through the TDFAD approach contained in R5 [10] code. The TDFAD provides the construction of a limit line (Fig. 3.12) that changes according to the considered amount of time defining a region inside where, an hypothetical crack propagation will not be reached during the assessed time. It is built by evaluating K_r parameter according to:

$$K_r = \left[\frac{E\varepsilon_{ref}}{L_r\sigma_{0.2}^c} + \frac{L_r^3\sigma_{0.2}^c}{2 \cdot E\varepsilon_{ref}}\right]^{-0.5} \tag{3.11}$$

where E is the elastic modulus for the material at the temperature of the assessment, ε_{ref} is the total strain from average isochronous stress-strain curves calculated at the reference stress $\sigma_{ref} = L_r\sigma_{0.2}^c$. The stress $\sigma_{0.2}^c$ represents the 0.2% proof stress from the average isochronous stress-strain curves. K_r trends to a null value when L_r factor is greater than a cut-off value L_r^{max} defined as:

$$L_r^{max} = \frac{\sigma_R}{\sigma_{0.2}^c} \tag{3.12}$$

where σ_R is the rupture stress at the desired time of assessment. Since σ_R and $\sigma_{0.2}^c$ are time dependent, the limit line as well as the cut-off values change with the assessment time. The rupture time t_R of a uniaxial creep test can be expressed with reference to

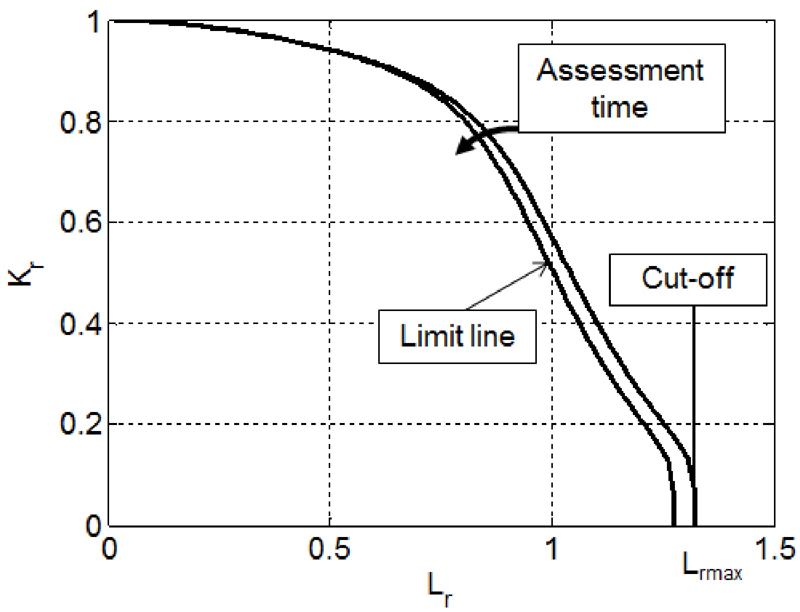

Figure 3.12: *Schematic diagram of the TDFAD.*

the test stress σ_R according to:

$$t_R(\sigma_R) = H\sigma_R^r \tag{3.13}$$

The coefficients of Eq. (3.13) are reported in Tab. 3.3 and were determined from a fitting procedure applied to the experimental creep rupture data presented in Sec. 2.1. Eq. (3.13) can be easily reversed in order to express the rupture stress σ_R at the assessed

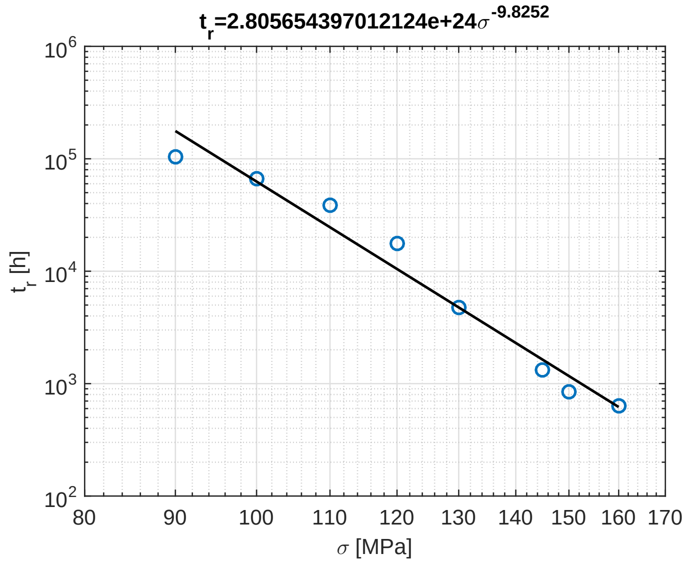

Figure 3.13: *Failure time t_R as a function of test stress σ_R of P91 at 600 °C.*

Table 3.3: *Coefficients of Eq. (3.13) for P91 at 600 °C.*

H	r
2.8057E24	-9.8252

time t_A

$$\sigma_R = \left(\frac{t_A}{H}\right)^{1/r} \tag{3.14}$$

In this TDFAD assessment the creep deformation is described through the secondary-tertiary creep law of Eq. (3.15):

$$\varepsilon^c(\sigma, t) = \lambda \dot{\varepsilon}_{min}(\sigma) t_R(\sigma) \left[1 - \left(1 - \frac{t}{t_R}\right)^{1/\lambda}\right] \tag{3.15}$$

where $\dot{\varepsilon}_{min}$ is the minimum creep strain rate of uniaxial creep tests and $t_R(\sigma)$ is the rupture time at the actual stress σ that acts on the component. λ is a material constants that was obtained equal to 7.74 by fitting the experimental uniaxial creep curves of P91 at 600 $^\circ C$ of Fig. 2.3 (a) and (b). The minimum creep strain rate during steady-state $\dot{\varepsilon}_{ss}$ was modeled according to the Norton law of Eq. (1.1) by using the high and low stresses A and n parameters of Tab. 2.3. CCG tests have been used to determine the material stress intensity factor at initiation i.e. a crack propagation of 0.2 mm. The experimental data of Fig. 3.14 were fitted to Eq. (3.16) in order to determine the material constants C_1, D_1 and q_1 of Tab. 3.4

$$K^c_{mat} = \left[E\left(C_1 + \frac{\Delta a}{D_1}\right)^{\frac{1}{q_1}} \cdot t_i^{-\left(\frac{1}{q_1}-1\right)}\right]^{0.5} \tag{3.16}$$

Because the assessment is performed in creep-fatigue regime, from high temperature

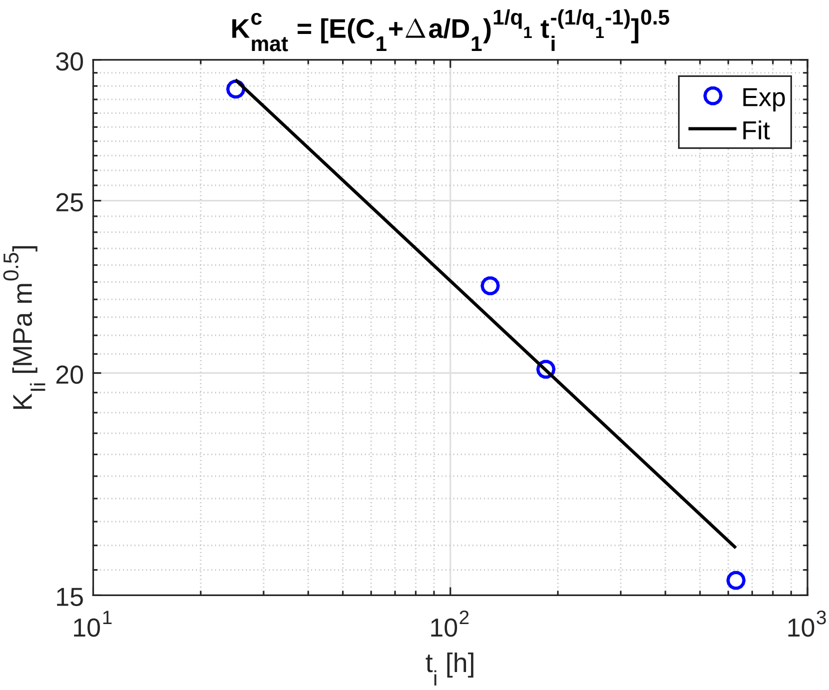

Figure 3.14: *Material creep fracture toughness at initiation: experimental data and fit.*

Table 3.4: *Material constants for determining creep fracture toughness of P91 at 600 °C.*

C_1	D_1	q_1

fatigue tests it is possible to identify the propagation ratio per cycle as a function of the stress intensity factor variation using the Paris law of Eq. (1.76). The experimental tests shown in Fig. 2.36 at different load ratios R and frequencies, provided 4 sets of Paris law constants. The set of constants obtained by test P91-24 performed at f =1 [Hz] and $R = 0.1$ was used in the following calculations. At this point the complete procedure to evaluate whether an hypothetical defect occurs during the assessment time or not is reported.

- The first step consists of assuming an initial assessment time t_A that shall be short enough to guarantee that initiation, i.e. a crack propagation of 0.2 mm, is not reached during this time.
- Evaluate the rupture stress σ_R at the time t_A with Eq. (3.14).
- Minimize Eq. (3.15) in order to obtain the stress $\sigma^c_{0.2}$ that produces a creep strain

ε^c of 0.2% in the assessment time t_A.

$$\varepsilon^c(\sigma^c_{0.2}, t_A) = 0.2\% \rightarrow \sigma^c_{0.2} \tag{3.17}$$

- Determine the cut-off value $L_{r,max}$ according to Eq. (3.12).
- In order to build the limit line a vector $\vec{L}_r$ shall be defined:

$$\vec{L}_r = \left(0 : \frac{L_{r,max}}{\Delta L_r} : L_{r,max}\right) \tag{3.18}$$

- The reference stress σ_{ref} can now be defined:

$$\vec{\sigma}_{ref} = \vec{L}_r \sigma^c_{0.2} \tag{3.19}$$

- The reference creep strain ε_{ref} can be obtained by using the isochronous creep curve of Eq. (3.15) and by subtracting the elastic part of the strain $\frac{\vec{\sigma}_{ref}}{E}$

$$\vec{\varepsilon}_{ref}(\vec{\sigma}_{ref}, t_A) = \lambda \dot{\varepsilon}_{min}(\vec{\sigma}_{ref}) t_R(\vec{\sigma}_{ref}) \left[1 - \left(1 - \frac{t_A}{t_R(\vec{\sigma}_{ref})}\right)^{1/\lambda}\right] + \frac{\vec{\sigma}_{ref}}{E} \tag{3.20}$$

- The limit line can now be calculated:

$$\vec{K}_r = \left(\frac{E\vec{\varepsilon}_{ref}}{\vec{L}_r \sigma^c_{0.2}} + \frac{\vec{L}^3_r \sigma^c_{0.2}}{2E\vec{\varepsilon}_{ref}}\right)^{-0.5} \tag{3.21}$$

The limit line defines a region inside which, a propagation of 0.2 mm will not be reached during the assessment time. This limit line entirely depends on material behavior in fact geometry, pressure and crack morphology of the pipe has not still been considered. It is now possible to evaluate the material creep toughness parameter K_{mat} based on the stress intensity factor range acting on the pipe 3.3 considering a load ratio $R = 0.1$ and different hold times t_h and operative pressures P_i. The existence of fatigue cycles requires a revision of the assumed defect propagation during the assessment time. The creep-fatigue crack propagation variation Δa_{cf} is then split between fatigue Δa_f and creep Δa_c damage respectively:

$$\Delta a_c = \Delta a_{cf} - \Delta a_f \tag{3.22}$$

where fatigue crack propagation during the assessment time is obtained with the Paris Law during the number of cycles N considered:

$$\Delta a_f = \int_0^{t_A} \left(\frac{da}{dt}\right) dt = \int_1^{\frac{t_A}{t_h}} \left(\frac{da}{dN}\right) dN = \sum_{i=1}^{\frac{t_A}{t_h}} C \Delta K^m \tag{3.23}$$

ΔK is calculated according to the API RP-579 code [5] and will be discussed later. The initiation model based on CCG experimental data of Fig. 3.14 is used to define a new material toughness parameter K_{mat} starting from the material creep toughness parameter K_{mat}^{c} of Eq. (3.16):

$$K_{mat} = K_{mat}^{c}\left[\frac{\Delta a_c}{\Delta a_{cf}}\right]^{1/2q_1} \tag{3.24}$$

As previously anticipated, mode I stress intensity factor K_i and stress intensity factor range ΔK was calculated according to the API RP 579 [5] code. For a cylinder with a semi-elliptical shape crack in longitudinal direction facing internal pressure the stress intensity factor and its range is given by Eqs (3.25 and 3.26):

$$K = \frac{P_i r_o^2}{r_o^2 - r_i^2}\left[2G_0 - 2G_1\left(\frac{a}{r_i}\right) + 3G_2\left(\frac{a}{r_i}\right)^2 - 4G_3\left(\frac{a}{r_i}\right)^3 + 5G_4\left(\frac{a}{r_i}\right)^4\right]\sqrt{\frac{\pi a}{Q}} \tag{3.25}$$

$$\Delta K = (1-R)K \tag{3.26}$$

where G_0 and G_1 coefficients can be determined by using the following equations

$$G_0 = A_{0,0} + A_{1,0}\delta + A_{2,0}\delta^2 + A_{3,0}\delta^3 + A_{4,0}\delta^4 + A_{5,0}\delta^5 + A_{6,0}\delta^6 \tag{3.27}$$

$$G_1 = A_{0,1} + A_{1,1}\delta + A_{2,1}\delta^2 + A_{3,1}\delta^3 + A_{4,1}\delta^4 + A_{5,1}\delta^5 + A_{6,1}\delta^6 \tag{3.28}$$

where δ is given by:

$$\delta = \frac{2\theta}{\pi} \tag{3.29}$$

where θ is the considered angle, e.g. $\theta = 0$ in plane stress condition (point B of Fig. 3.3) and $\theta = \pi/2$ in plane strain condition (point A of Fig. 3.3). $A_{i,i}$ coefficients are summarized in Tab. 3.5 for a longitudinal semi-elliptical inside surface crack in a cylinder. Different values of a/c and a/w were considered by linearly interpolating the given values. Q is a coefficient that depends on the crack geometry:

$$Q = 1 + 1.464\left(\frac{a}{c}\right)^{1.65} \qquad \text{for } a/c \leq 1 \tag{3.30}$$

$$Q = 1 + 1.464\left(\frac{c}{a}\right)^{1.65} \qquad \text{for } a/c > 1 \tag{3.31}$$

Coefficients G_2, G_3 and G_4 can be determined according to the following equations in plane strain conditions $\phi = \pi/2$:

$$G_2 = \frac{\sqrt{2Q}}{\pi}\left(\frac{16}{15} + \frac{1}{3}M_1 + \frac{16}{105}M_2 + \frac{1}{12}M_3\right) \tag{3.32}$$

$$G_3 = \frac{\sqrt{2Q}}{\pi}\left(\frac{32}{35} + \frac{1}{4}M_1 + \frac{32}{315}M_2 + \frac{1}{20}M_3\right) \tag{3.33}$$

Table 3.5: A_{ii} *influence coefficients for a longitudinal semi-elliptical inside surface crack in a cylinder.*

w/r_i	a/c	a/w	G_i	A_0	A_1	A_2	A_3	A_4	A_5	A_6
0.33333	0.03125	0	G0	0.1965046	2.9373464	-5.2582823	7.4889153	-6.9282667	3.3673349	-0.6677966
			G1	0.005178	0.175028	2.771868	-4.6457154	4.6780502	-3.276809	0.9840994
		0.2	G0	0.2172042	2.5042847	-2.1152523	-1.0663053	5.5897238	-5.8369981	1.9620413
			G1	0.0076407	0.2402259	2.3741989	-3.4818023	3.2921834	-2.5081221	0.8062819
		0.4	G0	0.221304	3.086523	-5.31628	10.10488	-9.41905	3.078245	-0.07513
			G1	0.010904	0.237907	2.725715	-4.55891	6.414869	-5.95648	2.022734
		0.6	G0	0.232672	3.453643	-7.51716	21.60268	-27.4566	15.28585	-3.30802
			G1	0.012487	0.283331	2.511357	-3.38107	6.255188	-7.18553	2.628915
		0.8	G0	0.243151	3.792504	-9.4367	34.62553	-49.5858	30.87791	-7.47816
			G1	0.012925	0.352624	1.997745	-0.58383	3.076408	-5.71804	2.284734
0.33333	0.0625	0	G0	0.2695332	2.1626001	-1.6551569	-1.2970208	4.5604304	-4.3163876	1.4010655
			G1	0.0138667	0.1827458	2.5749608	-3.9044679	3.3556301	-2.1772209	0.6420134
		0.2	G0	0.2844799	2.0640002	-1.1370689	-1.3784733	3.1901236	-2.4501643	0.6364234
			G1	0.0196105	0.216275	2.5422614	-4.2578287	4.5779897	-3.5058747	1.1186308
		0.4	G0	0.322094	2.438214	-1.98376	0.244152	4.224652	-5.91198	2.249442
			G1	0.03027	0.269097	2.624235	-4.32539	5.244741	-4.41492	1.427343
		0.6	G0	0.369015	2.865779	-3.67144	7.489422	-5.18818	-1.15028	1.427836
			G1	0.042148	0.350887	2.498683	-3.8769	6.128223	-6.28316	2.200696
		0.8	G0	0.427453	3.194318	-5.00364	17.18344	-22.1341	11.3312	-2.13695
			G1	0.054034	0.441918	2.130498	-1.76695	3.500662	-4.66738	1.655006
0.33333	0.125	0	G0	0.4065238	0.7772483	3.8861644	-12.573943	16.760207	-11.014593	2.8706957
			G1	0.032027	0.1825342	2.2670449	-2.7076615	1.2088194	-0.377743	0.0763155
		0.2	G0	0.4128225	1.1171748	1.7294667	-6.5703783	8.5967302	-5.578925	1.4430231
			G1	0.0491457	0.0109153	3.9207133	-9.2000295	12.768245	-9.8975712	3.034571
		0.4	G0	0.499977	1.11228	3.40801	-12.8313	19.95677	-15.1319	4.407079
			G1	0.065536	0.265337	2.296419	-3.19376	2.622579	-1.81326	0.549769
		0.6	G0	0.617501	1.225733	4.031972	-14.5662	24.32044	-19.8868	6.106634
			G1	0.099839	0.284951	2.683812	-4.61271	5.80132	-4.842	1.533094
		0.8	G0	0.792049	1.012777	6.866883	-21.9541	36.42926	-29.7102	9.010192
			G1	0.147658	0.224455	3.553285	-7.20684	10.47417	-8.38954	2.38831
0.33333	0.25	0	G0	0.6152816	-0.3348694	6.295562	-15.590618	19.299508	-12.488107	3.3010035
			G1	0.0703566	0.2828152	1.4036169	-0.6511596	-1.2076596	1.0318656	-0.2423741
		0.2	G0	0.61512	-0.2559286	6.9419508	-19.977395	28.061835	-19.892262	5.6000832
			G1	0.0890045	0.1593445	2.5204791	-5.1000189	6.3764694	-4.8919376	1.5129735
		0.4	G0	0.730513	-0.32208	6.342731	-15.3906	18.41126	-11.3497	2.819398
			G1	0.1265635	0.1445088	2.2324974	-3.0386458	2.2662085	-1.4535727	0.4548018
		0.6	G0	0.912433	-0.76652	9.156134	-23.0813	29.89695	-19.9456	5.311944
			G1	0.168776	0.101417	2.609113	-3.88848	3.419227	-2.20104	0.612027
		0.8	G0	1.162612	-1.39709	12.5962	-31.8562	42.73281	-29.1466	7.768164
			G1	0.245071	-0.1281	3.94243	-7.53721	9.006448	-6.08161	1.536629
0.33333	0.5	0	G0	0.8776607	-0.6729719	3.7721411	-6.520906	6.3377934	-3.7028038	0.9872447
			G1	0.1277541	0.4368502	0.4904522	1.0427434	-2.9631236	2.0826525	-0.5184313
		0.2	G0	0.8818313	-1.0917996	6.7441757	-15.991176	21.054792	-14.772037	4.2281725
			G1	0.1441557	0.1424866	2.3284045	-4.7895448	6.1386818	-4.8362727	1.5452935
		0.4	G0	0.940798	-0.49854	1.917025	-0.01925	-4.63706	5.216683	-1.80754
			G1	0.1711202	0.1668531	1.926756	-3.2630245	3.5831509	-2.8636537	0.9729171
		0.6	G0	1.115289	-1.34423	5.945865	-10.0972	8.932753	-4.06213	0.718593
			G1	0.2163543	0.1549463	1.5248691	-1.5230688	0.7692177	-0.7731253	0.369949
		0.8	G0	1.291008	-1.34637	4.360198	-3.76081	-1.33649	3.843603	-1.66933
			G1	0.261785	0.151261	1.179357	0.356858	-2.84394	2.601947	-0.874
0.33333	1	0	G0	1.1977992	-0.524487	0.1498299	2.3284866	-5.1058499	4.3469049	-1.348798
			G1	0.1870117	0.6987352	0.13169	0.7269255	-2.5259384	2.1756251	-0.6540458
		0.2	G0	1.1843664	-1.1847612	4.990228	-13.538735	21.119771	-17.017414	5.4794601
			G1	0.2064638	0.1880635	3.2277985	-9.0382566	13.410536	-10.743271	3.4724686
		0.4	G0	1.2310867	-1.2996546	5.3458402	-14.297856	22.283375	-18.132719	5.9308732
			G1	0.2232606	0.1330441	3.4286845	-9.5400946	14.273538	-11.599332	3.8156481
		0.6	G0	1.3016702	-1.3329884	4.6823879	-11.389326	16.885721	-13.394792	4.3283933
			G1	0.2440755	0.1533295	3.0387623	-7.9723882	11.374712	-9.0179366	2.9233036
		0.8	G0	1.405999	-1.48444	4.601583	-9.7191	12.97917	-9.59639	2.96047
			G1	0.254777	0.3338937	2.0367399	-5.9096868	9.5170399	-8.2252015	2.7607498
0.33333	2	0	G0	0.8150546	-0.5623828	1.4465771	-4.6778133	8.4192164	-7.9025932	2.9866351
			G1	0.1359146	0.070234	3.5558581	-11.034445	16.967724	-14.126991	4.8706612
		0.2	G0	0.8291377	-0.9895481	4.1798664	-12.600881	20.280744	-16.914774	5.7445745
			G1	0.1367171	0.0546432	3.3517976	-10.030368	14.931862	-12.199484	4.1771813
		0.4	G0	0.8281292	-1.0079708	4.356094	-13.17069	21.184349	-17.62477	5.9654552
			G1	0.1383911	0.0271839	3.5221879	-10.559706	15.796147	-12.905023	4.4038513
		0.6	G0	0.8416824	-1.0386714	4.4633302	-13.408838	21.463769	-17.80813	6.0224184
			G1	0.1432074	0.0086329	3.611371	-10.774368	16.083937	-13.122391	4.4757876
		0.8	G0	0.8492888	-0.8700518	3.1479406	-8.7543723	13.222524	-10.685678	3.6241547
			G1	0.1360843	0.2203399	2.2144388	-6.1874959	8.3319395	-6.6071612	2.3172922

$$G_4 = \frac{\sqrt{2Q}}{\pi}\left(\frac{256}{315} + \frac{1}{5}M_1 + \frac{256}{3465}M_2 + \frac{1}{30}M_3\right) \tag{3.34}$$

where M_1, M_2 and M_3 are equal to:

$$M_1 = \frac{2\pi}{\sqrt{2Q}}(3G_1 - G_0) - \frac{24}{5} \tag{3.35}$$

$$M_2 = 3 \tag{3.36}$$

$$M_3 = \frac{6\pi}{\sqrt{2Q}}(G_0 - 2G_1) + \frac{8}{5} \tag{3.37}$$

The plastic collapse load p_L was defined according to the global solution proposed by the R6 [11] code:

$$\begin{aligned} p_L =& \gamma f_{ps}\left[\frac{1}{M_{in}}\ln(1+a/r_i)\left(1+a/r_i\left(1-\frac{1}{M_{in}}\right)\right)\ln\left(\frac{1+w/r_i}{1+a/r_i}\right)\right] + \\ & \sqrt{\left(1+\frac{1}{2}\left(1+\frac{1}{M_{in}}\right)a/r_i f_{ps}\right)+\frac{1}{4}\left(1-\frac{1}{M_{in}^2}\right)(a/r_i f_{ps})^2 -} \\ & \left(1+\frac{1}{2}\left(1+\frac{1}{M_{in}}\right)a/r_i f_{ps}\right) \end{aligned} \tag{3.38}$$

where:

- $$M_{in} = \left(1 + \frac{1.4(a/r_i)}{\left(\frac{a}{c}\right)^2(1+a/r_i)}\right)^{0.5} \tag{3.39}$$

- $$f_{ps} = \begin{cases} 1 & \text{w/o crack face pressure} \\ \begin{cases} \frac{1}{1+\frac{1}{2}\alpha\eta_i} & \text{for } (a/c) \le 1 \\ \frac{\Phi}{\Phi+\frac{1}{2}\alpha\eta_i} & \text{for } (a/c) > 1 \end{cases} & \text{w/ crack face pressure} \end{cases} \tag{3.40}$$

- $$\gamma = \begin{cases} 1 & \text{Tresca based solution} \\ \frac{2}{\sqrt{3}} & \text{Mises based solution} \end{cases} \tag{3.41}$$

It is now possible to identify a point on the TDFAD diagram (Fig. 3.12):

$$L_r = \frac{P_i}{p_L} \tag{3.42}$$

$$K_{ri} = \frac{K}{K_{mat}^c} \tag{3.43}$$

If the assessed point lies inside the limit line of Fig. 3.12, the assessment time t_A is increased by a step time Δt. When the assessed point is no longer confined in the limit line, the initiation time is reached and crack propagation rate can now be evaluated according to the $(C_t)_{avg}$ model through the creep reversal parameter C_R.

3.3.3 Creep-Fatigue Crack Initiation and Propagation Assessment

After validation with experimental data, the proposed creep-fatigue crack initiation and growth model was extended to the pipe geometry displayed in Fig. 3.3 with an initial crack size $a = 5\%w$, $10\%w$, and $12.5\%w$ at the nominal pressure level of 25 MPa. The C^* parameter included in Eq. (3.10) was calculated according to the C_{ref} approach contained in BS 7910 standard ([12]). The results shown in Fig. 3.15 (a), (b), and (c) highlight the detrimental effect given by the cyclic load. The shorter the hold time t_h is, the faster the crack propagation is. However, if a hold time of 10 hours is considered, i.e. the typical operating condition of power plant pipes, the residual life is reduced by an approximated factor of 2.2 with respect to the life prediction in pure CCG conditions obtained by imposing a hold time $t_h = 500000$ hours. Regarding residual life estimations in CCG conditions, it might be worth noting how the failure time is reduced with respect to the CCG assessments of Sec. 3.2. This was expected because, as previously discussed, both approaches provided by API 579 [5] and BS 7910 [12] did not provide a conservative solution at low stress and crack growth rate levels with C^* and C_t (Fig. 3.2 and 3.7) while the procedure discussed in this Section strongly depends on crack propagation correlation functions obtained experimentally in Ch. 2.

3.4 Summary

In this Chapter methods to model creep and creep-fatigue crack initiation and growth in power plant pipes were discussed. Under creep conditions, the 2CD approach contained in the Fitnet [24] procedure was combined with the BS7910 [12] approach in order to model CCI and CCG respectively. The 2CD was based on the experimental tests of uniaxial creep and CCG performed on the modified P91 material. In this context, the ligament damage was evaluated according to the Larson-Miller parameter while the crack tip damage was based on the creep crack initiation data. The CCG rates were obtained by using their relationship with the crack tip parameter C_{ref} that was calculated with a reference stress approach. The Norton law coefficients for high and low stresses reported in Tab. 2.3 were used to identify a reference strain rate $\dot{\varepsilon}_{ref}$ that allowed the estimation of the crack tip parameter C_{ref}. The predictions performed with this method provided a good estimation of the residual life for the component operating at 25 MPa and were aligned to the same estimations performed with the API 579 [5] method. The predictions performed at an internal pressure of 50 MPa instead turned out to be less conservative that the API 579 code.

Under creep-fatigue conditions, the TDFAD approach contained in R5 code [10] was sided by an alternative method based on the analytic calculation of the crack tip pa-

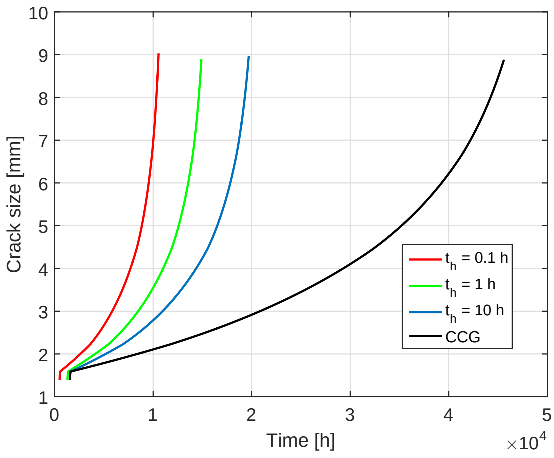

(a) $a_0 = 12.5\%w$.

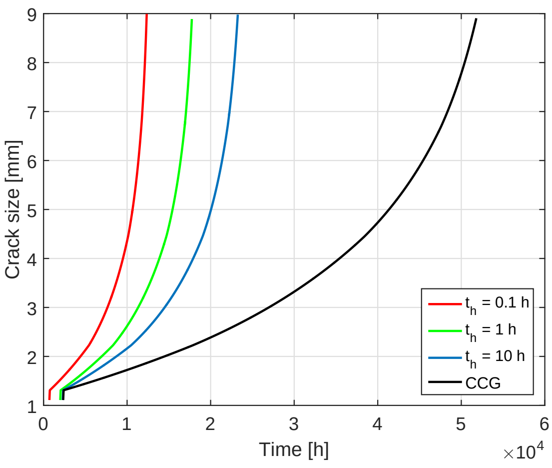

(b) $a_0 = 10\%w$.

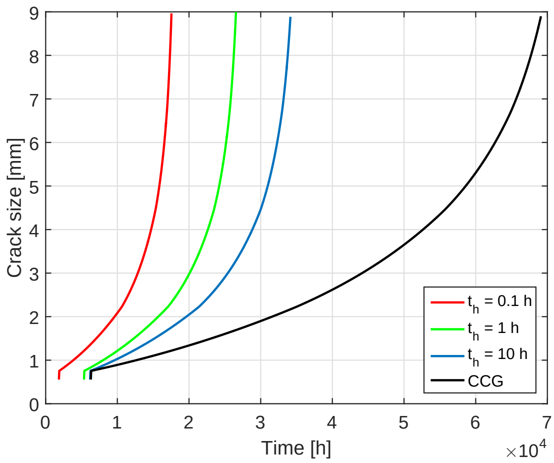

(c) $a_0 = 5\%w$.

Figure 3.15: *Creep-fatigue crack initiation and growth predictions in pressurized pipes with axial defect operating at 25 MPa .*

rameter $(C_t)_{avg}$ under the hypothesis of partial reversal of the creep strains during the fatigue cycles. The TDFAD approach was applied to evaluate the CFCI and required: experimental creep data in terms of rupture times, creep and minimum creep strain rates; experimental CCI data derived from the CCG tests of Sec. 2.2; the Paris-Erdogan coefficients derived from the HT FCG tests of Sec. 2.5. CFCG was modeled by means of the $(C_t)_{avg}$ parameter thanks to its analytical definition based on the creep reversal parameter C_R that was determined from the load-line displacement records of the experimental CFCG tests performed on C(T) specimens (Sec. 2.3). The results obtained from the application of this proposed method, highlighted at the operating conditions of 25 MPa, the detrimental effects of the fatigue damage. The shorter the hold time t_h is, the faster the crack propagation rates are. Although by assessing an hold time of 10 hours, close to the actual load cycles of power plant pipes, the time to rupture is reduced by a factor of 2.2 with respect to the pure CCG prediction.

CHAPTER 4

Numerical Simulations of CCG and CFCG

This chapter deals with the description of finite element (FE) analyses performed to predict the CCG and CFCG behavior of the experimental tests previously described in Ch. 2.
The CCG model, after validation by means of comparison with the experimental tests on C(T) specimens, is extended to a pipe geometry in order to characterize the creep damage distribution in axial cracks located on the inside surface.
A good estimation of the HT resistance for a material represents a starting point for the residual life assessment of cracked components. A comprehensive review of several uniaxial creep models with the aim to identify the one, that in combination with an opportune continuum damage approach, is able to estimate by FE analysis the creep crack propagation rate.
The numerical simulations were performed on the FE software Abaqus 6.14 with dedicated Fortran user subroutines to represent the viscous behavior of the material, the creep damage, and the crack propagation.

4.1 Uniaxial Creep Models

The main aspect regarding the numerical simulations under these critical conditions is represented by the need of an opportune creep model that, not only is able to describe

the experimental phenomenon accurately, but, also, it can be easily applied to the FE framework. For this reason, a critical review of the state-of-the-art uniaxial creep models shall be always considered when trying to predict CCG and CFCG behavior through numerical simulations.
All the different approaches found in scientific literature provided a good starting point for the FE simulations contained in this work. In addition to this, they also highlighted some limitations. Firstly, some of them, do not always provide a complete description of the creep damage. As it will be later shown, some approaches are formulated neglecting the primary part of the creep curves. This results in simulating under the hypothesis of an instantaneous steady-state creep behavior for the material that is acceptable when modeling high reference stresses, but might be not enough accurate when modeling low reference stresses, i.e. the standard operating condition for power plant pipes. This aspect, also, represents a limitation when modeling creep-fatigue crack growth. In fact, the interaction between the evolving creep zone and the cyclic plastic zone is not represented by neglecting the small-scale creep effects. This also explain the reason why nowadays not so many CFCG numerical models are available. The last important shortcoming related to CCG and CFCG simulations, is the transposition of these models to predict the resistance of components rather than testing specimens. Creep crack growth models are typically obtained by:

- uniaxial creep deformation models that explicitly admit cavitation damage;
- their extension to multiaxial stress conditions given by the presence of crack tip.

Uniaxial creep models can be further divided in two main groups depending on the variable that is used to describe the creep strain rate $\dot{\varepsilon}^c$:

- time dependent models;
- strain dependent models.

Among the time dependent models the one proposed by Kachanov [35] consists in a couple of continuum damage constitutive equations that define the creep strain rate $\dot{\varepsilon}^c$ and the damage evolution rate $\dot{\omega}$:

$$\dot{\varepsilon}^c = \frac{3}{2}A'\left(\frac{\sigma_{eq}}{1-\omega}\right)^{n'}\frac{S_{ij}}{\sigma_{eq}}t^{m'} \tag{4.1}$$

$$\dot{\omega} = B'\frac{\sigma_R^{\chi'}}{(1-\omega)^{\varphi'}}t^{m'} \tag{4.2}$$

where A', n', m', B', χ' and φ' are material constants that must be fitted to complete experimental creep curves at different stress σ_{eq} and S_{ij} is the deviatoric stress tensor.

The rupture stress σ_R is defined according to Eq. (4.3) in relation to the multiaxial stress state parameter α' and the maximum principal stress σ_1.

$$\sigma_R = \alpha'\sigma_1 + (1 - \alpha')\sigma_{eq} \tag{4.3}$$

This model does not require any extension to multiaxial stress state which is already included by considering Eq. (4.3). With the Kachanov model it is also possible to reproduce the entire creep curve including primary secondary and tertiary creep. The primary part of the creep curve is given by the $t^{m'}$ term where m' has a negative value. A' and n' have the same function of the A and n Norton law constants of Eq. (1.1) and therefore they describe the steady-state creep deformation. Equation (4.1) tends to an infinite value when the damage ω tends to a unit value simulating tertiary creep, i.e. a fast creep strain rate. In this model the determination of the six material constants might be challenging due to the different ranges of each constant. Hyde et al. [30] suggested a simplified three variable approach that can be applied if the normalized creep curves at the same temperature and at different stress levels show a similar behavior. Unfortunately, as previously discussed (Sec. 2.1), P91 is affected by a different creep mechanism if low and high stresses are considered as shown in the normalized creep curves of Fig. 4.1. For this reason, the simplified approach by Hyde [30] is not applicable in this work and therefore, the standard six variables approach shall be followed. However the numerical applicability of this model might be complicated due to the fact that the damage evolution (Eq. (4.2)) starts at ω values close to unity as, also, observed by Saber [46]. This causes an extreme damage localization at the crack tip and an high mesh dependency of the solution.

Another time dependent model that is less mesh-dependent is the one proposed much later by Liu and Murakami [39] based on a micromechanics approach. It consists in the two constitutive Eqs (4.4 and 4.5):

$$\dot{\varepsilon}^c = \frac{3}{2}A''\sigma_{eq}^{n''-1}S_{ij}\exp\left[\frac{2(n''+1)}{\pi\sqrt{1+3/n''}}\left(\frac{\sigma_1}{\sigma_{eq}}\right)^2\omega^{3/2}\right] \tag{4.4}$$

$$\dot{\omega} = \frac{B''(1-e^{-q_2})}{q_2}\sigma_R^{\chi''}e^{q_2\omega} \tag{4.5}$$

where A'', n'', B'', q_2 and χ are material constants. This model suggests an exponential damage evolution equation that reduces the singular stress sensitivity observed in the Kachanov's model. In this way the damage is no longer confined to a limited area of the crack tip and thus the mesh-dependency is drastically reduced. However the Liu and Murakami model itself does not account for primary creep. With the aim to simulate even the transient during the application of the load, it requires the extension proposed

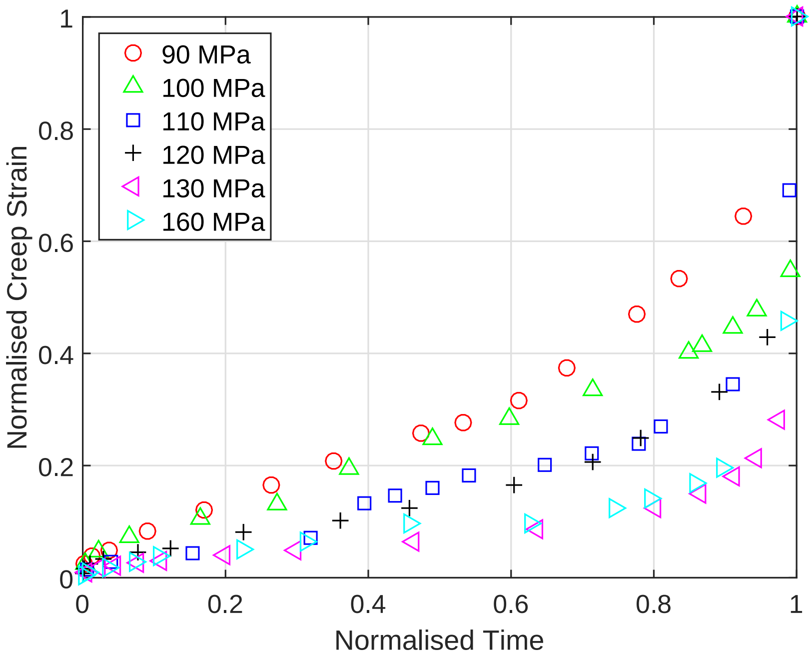

Figure 4.1: *Normalized creep curves of P91 at 600 °C.*

by Riedel [44] that changes Eq. (4.4):

$$\dot{\varepsilon}^c = \frac{3}{2} A'' \sigma_{eq}^{n''-1} S_{ij} \exp\left[\frac{2(n''+1)}{\pi\sqrt{1+3/n''}} \left(\frac{\sigma_1}{\sigma_{eq}}\right)^2 \omega^{3/2}\right] t^{m''} \tag{4.6}$$

The term $t^{m''}$ is analogous of the one present in Kachanov's model and is added to represent the primary creep in fact m'' has a negative value. The modified Liu-Murakami model depends on six material constants, that shall be determined from experimental creep uniaxial data, and the multiaxial stress state coefficient α, that can be determined either by fitting experimental creep tests of notched bars or experimental CCG tests on C(T) specimens.

In this work the material constants A'', n'' and m'' of Eq. (4.6) were fitted to the experimental uniaxial creep data of Fig. 2.3 that cover a stress range from 80 to 160 MPa through a least squares regression method. The material constants obtained during this fitting procedure are reported in Tab. 4.1. The Liu-Murakami modified model was then analytically applied to estimate the uniaxial creep behavior. Fig. 4.2 shows, as example, a comparison between the analytical estimation of the uniaxial creep test performed at $\sigma = 120$ MPa. The model gives a good prediction of the failure time for the specimen and, also, the primary creep and the minimum creep strain rate $\dot{\varepsilon}_{min}$ are well reproduced.

The next step is to verify the applicability of this model in a FE environment. With this purpose a 3D axisimmetric model was built with the FE software Abaqus based on the

Table 4.1: *Liu-Murakami model material constants for P91 at 600°C.*

A''	n''	m''
6.42E-21	8.02	-0.65

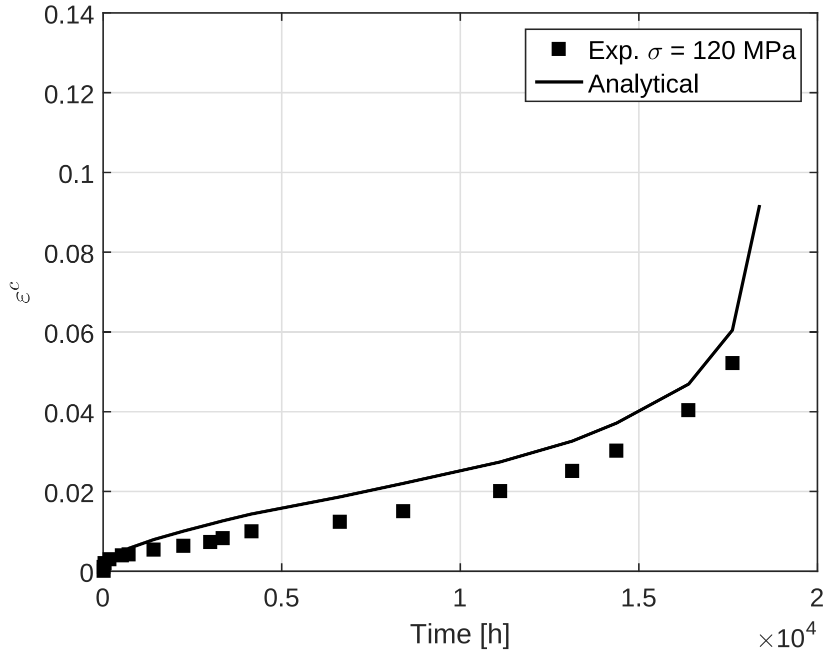

Figure 4.2: *Analytical application of the Liu-Murakami modified model with the material constants of Tab. 4.1.*

geometry of the creep cylindrical specimen of Fig. 4.3 with a gage length of 50 mm and a diameter of 10 mm. Because of axial symmetry only half of the specimen was studied. The elastic-plastic material properties previously discussed in Sec. 2.1 where applied together with the modified Liu-Murakami model that was linked to the FE software by means of a Fortran user-defined subroutine CREEP.for. The load, corresponding to a stress $\sigma = 120$ MPa, has been applied to a point lying on the symmetry section that was coupled to the upper surface. An average element size $L_{el} = 100\mu$m was used in the midline section and it is of the same order of magnitude of the average grain size for the studied P91 steel. Simulation was performed in two steps: the first consists in the application of the test load, while the latter is a viscous step where the irreversible creep deformation occurs. The strain has been acquired at the gauge length so that it was possible to compare the creep strain as a function of time with the experimental data and the analytical application of the model as shown in Fig. 4.4. The solution obtained with the FE method appears significantly different from the experimental and the analytical results. The reason of this can be attributed to the numerical integration of the FE simulation. In fact, at the beginning of the viscous step, small time steps are

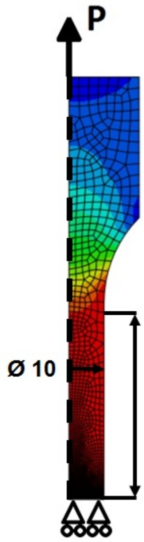

Figure 4.3: *Schematic draw of the uniaxial creep specimen.*

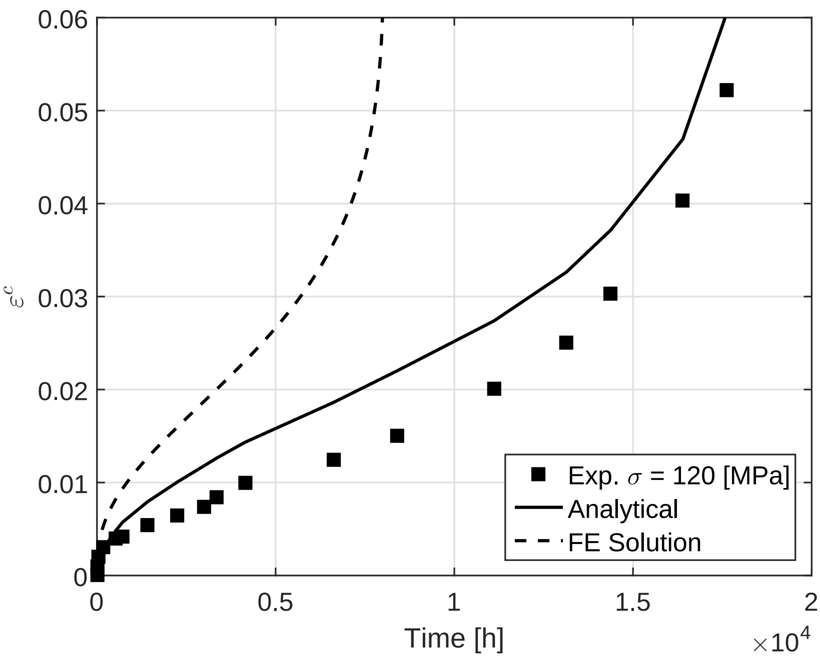

Figure 4.4: *Liu-Murakami modified model application to FE method: comparison with analytical model and experimental results*

required in order to converge to the solution. If a small time t is considered, e.g. 1E-10, Eq. (4.6) trends to high values of strain rates $\dot{\varepsilon}^c$ causing a premature creep deformation that decreases the time to failure significantly. This problem was solved by considering an initial time that is similar to the first creep strain data after the beginning of the experimental creep test. However, this approach is difficultly applicable to CCG simulations where the reference stress of the C(T) specimens is lower than the minimum stress σ of the uniaxial creep tests. This numerical integration issue could be solved by considering creep models that depend on other variables instead of the total time of the simulation.

The model proposed by Graham and Walles [26] depends on the creep strain ε^c and, therefore, the time dependency is implicit reducing any numerical integration issue. The original model contains also a temperature dependency that, for the purpose of this work, was neglected because a reference temperature of 600 °C is considered. It consists in the superposition of three power laws according to Eq. (4.7):

$$\dot{\varepsilon}^c = A_1 \sigma_{eq}^{n_1} (\varepsilon^c)^{m_1} + A_2 \sigma_{eq}^{n_2} (\varepsilon^c)^{m_2} + A_3 \sigma_{eq}^{n_3} (\varepsilon^c)^{m_3} \tag{4.7}$$

where A_i, n_i and m_i are material constants that as for previous models have been fitted to uniaxial creep data through a least squares regression technique. Due to the large range of the experimental creep strain rate data, the least squares LS were normalized according to:

$$LS = \left(\frac{\varepsilon^c_{exp.} - \varepsilon^c_{pred.}}{\varepsilon^c_{exp.}} \right)^2 \tag{4.8}$$

where $\varepsilon^c_{exp.}$ and $\varepsilon^c_{pred.}$ are the experimental creep strain and the predicted creep strain by using the Graham-Walles model. The fitting procedure allowed the determination of the 9 material constants reported in Tab. 4.2. It might be worth noting that since the available creep data highlighted a different behavior when low and high stresses are applied, splitting the fit procedure between two datasets representing the low and high stresses condition is expected to produce more accurate results. However, in a numerical simulation context, splitting the constitutive equation of the creep strain in two different solutions, reduces the time to convergence of the FE problem. For this reason it was chosen to represent the uniaxial creep data through a unique fit comprehending low and high stresses.

The axi-symmetric model used for the Liu-Murakami modified model was used, once

Table 4.2: *Graham-Walles model material constants for P91 at 600 °C.*

A_1	A_2	A_3	n_1	n_2	n_3	m_1	m_2	m_3
2.22E-42	7.75E-12	4.15E-13	16.42	1.45	6.03	-0.71	-0.80	3.69

again, to evaluate the numerical applicability of the model. For this reason, the user-defined subroutine CREEP.for was rewritten according to the Graham-Walles model and all the stress range of the experimental creep tests (Fig. 2.3, Ch. 2) were analyzed. Results are shown in Fig. 4.5 (a) and (b) in terms of creep strain as a function of time. The experimental data are well reproduced by the model at all the stress ranges. The failure time of the specimens is always underestimated except for the test performed

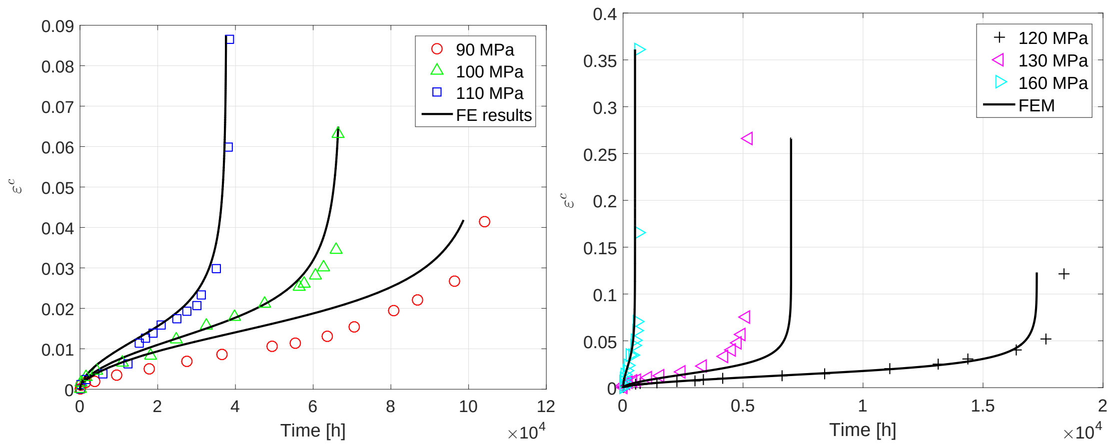

(a) *Low Stresses.*

(b) *High Stresses.*

Figure 4.5: *Graham-Walles FE model creep curves: comparison with experimental tests.*

at $\sigma = 130$ MPa that is slightly overestimated (Fig. 4.6. This can be attributed to the usual scatter in the experimental creep data. Fig. 4.7 shows the creep strain rate $\dot{\varepsilon}^c$ as a

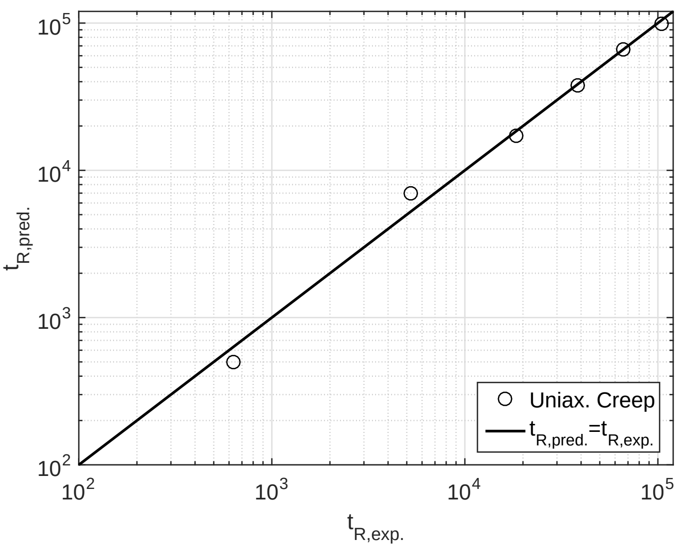

Figure 4.6: *Comparison between the predicted and the experimental failure times.*

function of time in low stresses (a) and high stresses (b) conditions. To summarize, the Graham-Walles model was successfully fitted to experimental creep data and included in a FE simulation of uniaxial creep cylindrical specimen. The numerical results were validated at different stress levels after they provided a good agreement with the experimental data. The primary creep phase is well represented and is expected to give a good estimation of the load-line displacement in the following CCG simulations. For this reason the Graham-Walles model was selected to represent the creep behavior in the FE simulations of the next section.

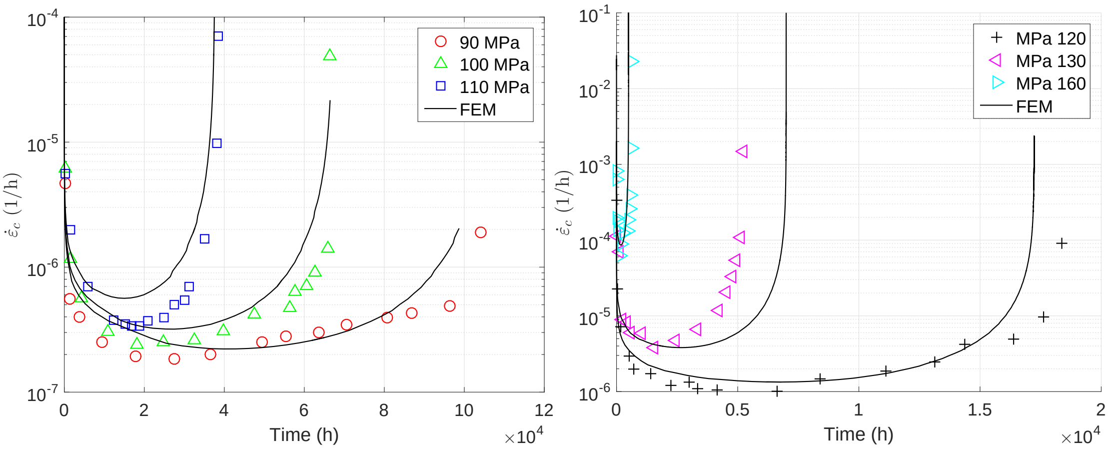

(a) *Low Stresses.* **(b)** *High Stresses.*

Figure 4.7: *Graham-Walles FE model creep strain rate as a function of time: comparison with experimental tests.*

4.2 Ductile Exhaustion Approach to Model Creep Damage

Once the creep behavior of the material is correctly described, CCG simulations requires an extension from uniaxial to multiaxial state conditions, and a formulation for the creep damage calculation. This extension which is already included in the damage formulations of Kachanov and Liu-Murakami modified models, however is not present in the Graham-Walles creep model. For this reason, a ductility exhaustion approach was studied and applied to this latter model, in order to be able to represent the creep damage even in cracked components that are affected by a multiaxial stress state close to the crack tip.

The ductility exhaustion approach can be summarized by looking at Fig. 4.8. It consists on considering the ligament ahead of the crack tip as a combination of multiple creep cylindrical specimens. As soon as one of these specimens reaches its creep ductility ε_f, it is no longer able to support stresses and therefore causes the crack to propagate. The damage approach used in the following simulations is based on a modification by Wen and Tu [54] of the Cocks and Ashby [14] model, for intergranular fracture during power-law creep under multiaxial stresses.

The typical morphology of a creep crack growth is shown in Fig. 4.9 and is the result of an experimental CCG test of Sec. 2.2. Fig. 4.9. Fig. 4.9 a) shows the initial formation of voids that nucleates at grain boundaries and, usually, with a perpendicular orientation with respect to direction of the tensile stress. Fig. 4.9 b) illustrates the coalescence of these voids that create a grain-sized crack. After long periods at high temperature, these micro-cracks link to each other causing the creep crack to propagate as shown in

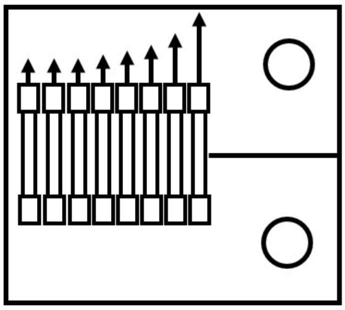

Figure 4.8: *Schematic diagram of the ductility exhaustion approach.*

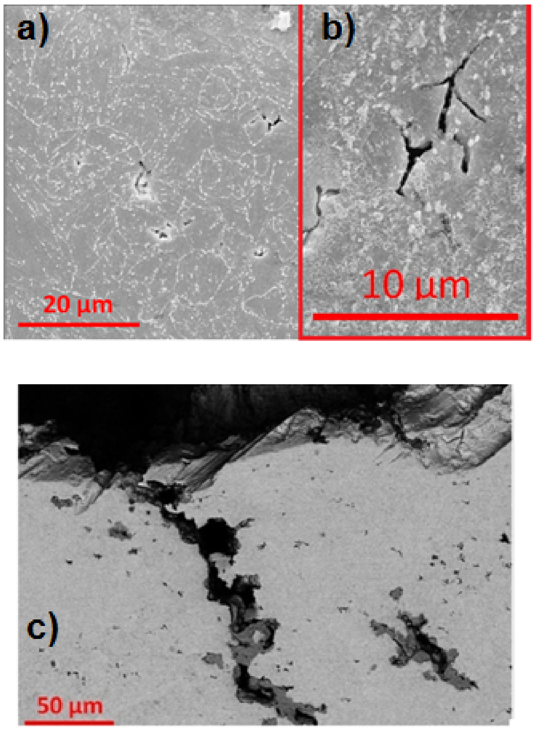

Figure 4.9: *Creep crack growth morphology of P91 tested at 600°C.*

Fig. 4.9 c).

The reason for cavity nucleation might be found in different mechanisms such as vacancy condensation, grain boundary sliding and dislocation pile-ups, but knowledge about them is not yet clear. Therefore the model herein described will deal with the cavity growth and coalescence rather than the nucleation processes. In this context several phenomenon are possible causes for cavity growth:

- Viscoplastic cavity growth;
- Diffusion controlled cavity growth;
- Constrained diffusion cavity growth.

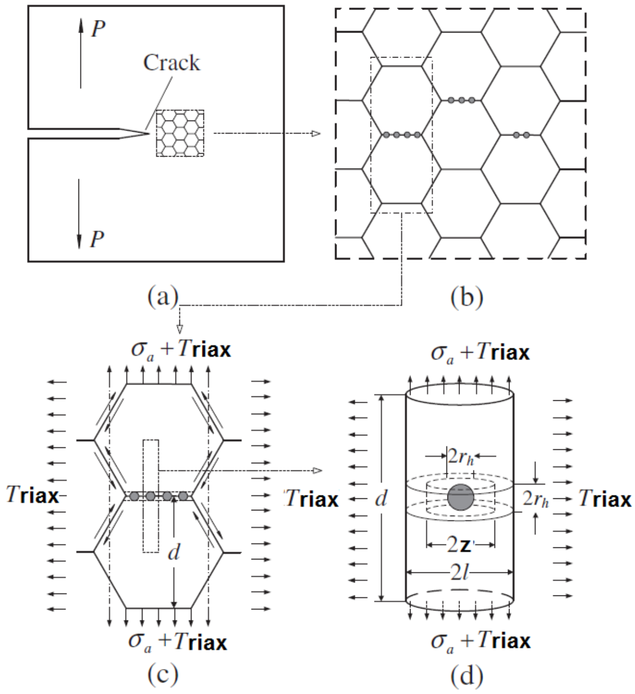

Figure 4.10: *Schematic Diagram of the cavity growth model [54].*

Each of these theories directly depend on the material properties and the temperature and stress levels applied to the material. It is known that at high strain rates and stresses the cavity growth might be due to viscoplasticity that directly alters the grains morphology, while at low strain rates and stresses, the vacancy diffusion is the driving mechanism for cavity growth. This explains, also, the different behavior found in the minimum strain rate of the uniaxial creep tests that varies with the applied stress (Fig. 2.5). In spite of that, in CCG conditions, the presence of an initial crack (Figs 4.10 a) and b)) drastically increases the strains and stresses in a region close to the cracktip. Therefore, viscoplasticity is assumed to be the driving mechanism for cavity growth and coalescence, if a contour close to the cracktip is considered.
In this area, Fig. 4.10 (c) shows two grains, with a group of voids located in the grain boundary region, subjected to a multiaxial traction σ_a + Triax. The cavity growth is measured by analysing the change of the volume of the slab containing the cavities if the following assumptions are verified:

- Incompressible material without volume variations;
- Shperical cavities of radius r_h change in volume but not in shape;
- Grain boundaries slide in order to accomodate the volume change in the slab;
- The slab width is much larger than its thickness;

- The cavity growth at grain boundaries is controlled by Power-law creep;
- The hydrostatic stress σ_h has no effect on the steady-state creep strain rate if there are no cavities.

The cylindrical volume of Fig. 4.10 (d) is considered in this model. This cylinder has a radius of dimension l equal to the semi distance between voids and height d i.e. the a grain size for the studied material. At the midline section of the volume a spherical cavity of radius r_h is considered and in order to obtain a better bound an additional arbitrary boundary zone cylinder of radius z where $r_h < z < l$ is identitfied. The cylinder is subjected to the axial stress σ_a and the triaxial stress Triax. On the grain boundary (see Fig. 4.11) the area fraction of voids f_h is easily described by Eq. (4.9)

$$f_h = \frac{\pi r_h^2}{\pi l^2} = \frac{r_h^2}{l^2} \tag{4.9}$$

The next step is to find a relationship between f_h and the and the creep strain without

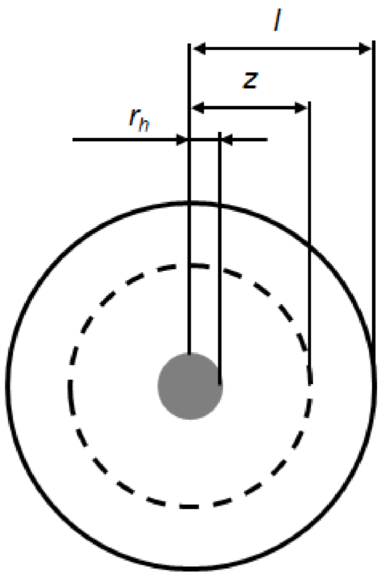

Figure 4.11: *Schematic draw of the grain boundary.*

considering any voids. In this context the variation of volume V can be expressed as a function of the rate of variation of f_h and the steady-state creep strain rate $\dot{\varepsilon}_{ss}$:

$$\frac{1}{V}\frac{dV}{dt} = \frac{2r_h}{d}\left(\frac{df_h}{dt} - f_h\dot{\varepsilon}_{ss}\right) \tag{4.10}$$

and at the same time as a function of the axial strain rate $\dot{\varepsilon}_a$:

$$\frac{1}{V}\frac{dV}{dt} = \dot{\varepsilon}_a + 2\dot{\varepsilon}_r = \dot{\varepsilon}_a - \dot{\varepsilon}_{ss} \tag{4.11}$$

where $\dot{\varepsilon}_r$ is the radial strain rate and in case of a cylinder is equal to $-\dot{\varepsilon}_{ss}/2$. Thanks to the energy principles, Cocks and Ashby [14] suggested the upper bound for $\dot{\varepsilon}_a$:

$$\dot{\varepsilon}_a = \dot{\varepsilon}_{ss}\left(1 - \frac{2r_h}{d}\frac{f_h}{f_z}\right) + \frac{2r_h}{d}\frac{f_h}{f_z}\left(\frac{\dot{\varepsilon}_{ss}}{(1-f_z)^n}\right)(1+G)^{(n+1)/2} \tag{4.12}$$

where $f_z = r_h^2/z^2$ is the area fraction of voids in the boundary cylinder of radius z and

$$G = 3\left(\frac{n}{n+1}\frac{1-f_z}{\ln f_w}\frac{\text{Triax}}{\sigma_a}\right)^2 \tag{4.13}$$

where $\text{Triax}/\sigma_a = \sigma_h/\sigma_{eq} - 1/3$. By combining Eqs (4.10 - 4.12) it is possible to express the void growth rate df_h/dt as a function of the power law creep:

$$\frac{df_h}{dt} = \dot{\varepsilon}_{ss}\frac{f_h}{f_z}\left(\frac{(1+G)^{(n+1)/2}}{(1-f_z)^n} - (1-f_z)\right) \tag{4.14}$$

Since of difficulties in finding a scientific relation between the void growth rate df_h/dt and the stress triaxiality σ_h/σ_{eq} Cocks and Ashby gave a semi-empirical equation:

$$\frac{df_h}{dt} = \frac{\dot{\varepsilon}_{ss}}{\alpha''}\left(\frac{1}{(1-f_h)^n} - (1-f_h)\right) \tag{4.15}$$

where α'' is a function of the hyperbolic sine of a parameter containing the creep power law exponent n and the stress triaxiality [14]:

$$\alpha'' = \sinh^{-1}\left[\frac{2(n-0.5)}{(n+0.5)}\frac{\sigma_h}{\sigma_{eq}}\right] \tag{4.16}$$

Eq. (4.15) can now be integrated in order to obtain the time to coalescence t_c of the micro-voids between the interval:

$$\begin{cases} f_h = f_i, & t = 0 \\ f_h = f_c, & t = t_c \end{cases} \tag{4.17}$$

where f_i and f_c are the initial void density and the void density at coalescence respectively.

$$t_c = \int_{f_i}^{f_c} \frac{\dot{\varepsilon}_{ss}}{\alpha''}\left(\frac{1}{(1-f_h)^n} - (1-f_h)\right) df_h \tag{4.18}$$

By multiplying and dividing by $(n-1)$ the integral can be solved considering that $\int f'(x)/f(x)$ is equal to $\ln f(x)$ where $f(x) = (1-(1-f_h)^{n+1})$ and $f'(x) = (n+1)(1-f_h)^n$:

$$\begin{aligned} t_c &= \frac{\alpha''}{\dot{\varepsilon}_{ss}}\int_{f_i}^{f_c}\frac{n+1}{n+1}\frac{(1-f_h)^n}{[1-(1-f_h)^{n+1}]}df_h \\ &= \frac{\alpha''}{\dot{\varepsilon}_{ss}(n+1)}\left|\ln\left[1-(1-f_h)^{n+1}\right]\right|_{f_i}^{f_c} \\ &= \frac{\alpha''}{\dot{\varepsilon}_{ss}(n+1)}\ln\frac{[1-(1-f_c)^{n+1}]}{[1-(1-f_i)^{n+1}]} \end{aligned} \tag{4.19}$$

The multiaxial ductility ε_f^* is easily determined according to Eq. (4.20)

$$\varepsilon_f^* = \dot{\varepsilon}_{ss} t_c = \frac{\alpha''}{n+1} \ln \frac{[1-(1-f_c)^{n+1}]}{[1-(1-f_i)^{n+1}]} \tag{4.20}$$

The uniaxial creep ductility ε_f can instead be calculated by updating the α'' function to its uniaxial formulation α_0'' obtained by observing that in uniaxial conditions $\sigma_h/\sigma_{eq} = 1/3$ at the time to coalescence t_{c0} in uniaxial conditions

$$\alpha_0'' = \sinh^{-1}\left[\frac{2}{3}\frac{(n-0.5)}{(n+0.5)}\right] \tag{4.21}$$

$$\varepsilon_f^* = \dot{\varepsilon}_{ss} t_{c0} = \frac{\alpha_0''}{n+1} \ln \frac{[1-(1-f_c)^{n+1}]}{[1-(1-f_i)^{n+1}]} \tag{4.22}$$

Thus the ratio, between multiaxial and uniaxial ductility, is now expressed by dividing Eq. (4.22) by Eq. (4.20):

$$\frac{\varepsilon_f^*}{\varepsilon_f} = \frac{\alpha''}{\alpha_0''} = \frac{\sinh\left[\frac{2}{3}\left(\frac{n-0.5}{n+0.5}\right)\right]}{\sinh\left[2\left(\frac{n-0.5}{n+0.5}\right)\frac{\sigma_h}{\sigma_{eq}}\right]} \tag{4.23}$$

As previously anticipated, in 2014 Wen and Tu [54] proposed a modification of the Cocks and Ashby cavity growth model that consists in the change of the function α'' and α_0'' with the following equations:

$$\alpha'' = \left[2 - 0.5\left(\frac{1}{5n}\right)^{n-1}\right] / \exp\left[\frac{2(n-0.5)}{(n+0.5)}\frac{\sigma_h}{\sigma_{eq}}\right] \tag{4.24}$$

$$\alpha_0'' = \left[2 - 0.5\left(\frac{1}{5n}\right)^{n-1}\right] / \exp\left[\frac{2}{3}\frac{(n-0.5)}{(n+0.5)}\right] \tag{4.25}$$

Following this approach the creep dutility ratio of Eq. (4.23) becomes:

$$\frac{\varepsilon_f^*}{\varepsilon_f} = \frac{\alpha''}{\alpha_0''} = \exp\left[\frac{2}{3}\left(\frac{n-0.5}{n+0.5}\right)\right] / \exp\left[2\left(\frac{n-0.5}{n+0.5}\right)\frac{\sigma_h}{\sigma_{eq}}\right] \tag{4.26}$$

and as shown in Fig. 4.12, with this modification, the theoretical normalized values of void growth rate $[1/(\dot{\varepsilon}_{ss} f_h) \cdot df_h/dt]$ is better described, especially at low levels of stress triaxiality σ_h/σ_{eq}, than the Cocks-Ashby original model.
For this reason the model by Wen-Tu [54] will be used to predict the crack propagation in the following CCG simulations because it is expected to represent better the void evolution even at low stress triaxiality condition, i.e. in regions where the stresses and strains intensification given by the crack tip is not relevant.

Thus a damage variable at the increment i, ω_i can now be defined by using Eq. (4.26)

$$\omega_i = \omega_{i-1} + \frac{\Delta\varepsilon^c}{\varepsilon_f^*} \tag{4.27}$$

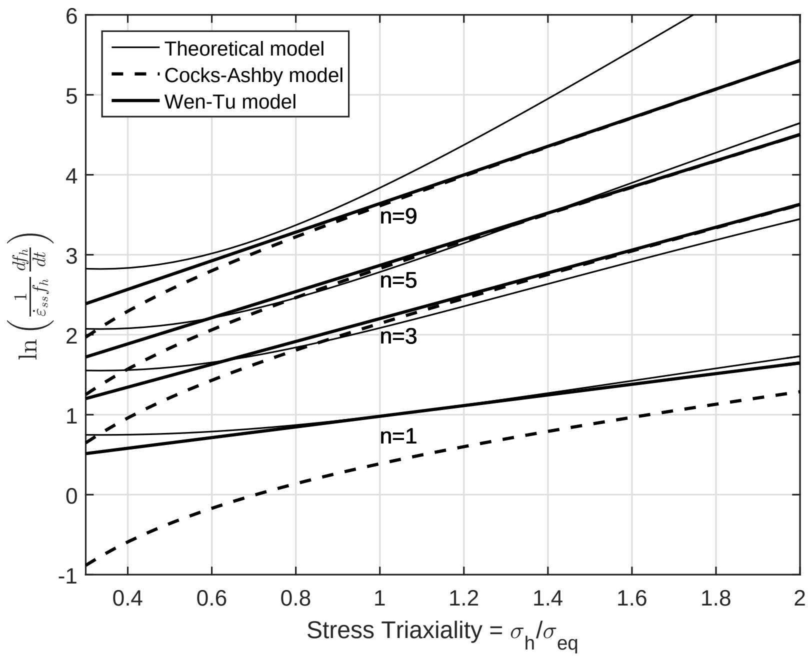

Figure 4.12: *Normalized void growth rate: comparison between the theoretical, Cocks-Ashby and Wen-Tu models.*

where $\Delta\varepsilon^c$ is the creep strain variation during increment i. This damage variable will be included in the FE code such as, when it reaches a value close to unity causes crack propagation.
This formulation of damage is included in the user-defined subroutine MPC.for for 2D analyses and in the user-defined subroutine USDFLD.for for 3D analyses.

4.3 CCG Numerical Simulation for C(T) Specimen [21]

Two FE models were considered during the numerical investigation of the CCG behavior of C(T) specimens of P91 material at 600°C:

- 2D plane strain 4 nodes elements model;
- 3D hexahedral 8 nodes elements model.

These two models were studied in order to identify possible variations in the results when considering a simplified plane strain condition rather than a 3D simulation that is known to correctly represent the constraint condition of the C(T) specimen (Fig. 2.7) used in the experimental tests of Sec. 2.2. In fact, in 3D, besides representing the correct conditions of plane strain and plane stress along the crack front, it is also possible to study the effects of the presence of the side grooves that reduce the section thickness

Table 4.3: *C(T) specimens data for FE simulations.*

W [mm]	B [mm]	B_n [mm]	a_0 [mm]	K_0 [MPa m$^{0.5}$]	P [N]	Δa_c [mm]
25.4	12.7	10.1	12.3	15.0	2940	2.4
				19.2	3770	1.8
				22.4	4400	2.7

B to the net section thickness B_n.

In both models same elastic-plastic properties of Sec. 2.1 were applied while the creep damage was modeled thanks to the user-defined subroutine CREEP.for that was implemented according to the Graham-Walles model of Sec. 4.1 and the user-defined subroutine MPC.for implemented according to the ductility exhaustion damage model of Sec. 4.2.

For the damage calculation according to Eq. (4.26), the uniaxial creep ductility ε_f was used to calculate its equivalent in multiaxial stress conditions according to Eq. (4.26). The value of ε_f was chosen from the experimental creep data of Fig. 2.3. However since the tests provided a very large scatter in data, different values of ε_f were studied in a sensitivity analysis that, in the following section follows the preliminary results obtained with an optimized value of uniaxial creep ductility based on the experimental CCG data of Sec. 2.2. For each model, three initial stress intensity factor conditions were studied in order to represent the experimental CCG tests of Sec. 2.2. The maximum crack propagation allowed was limited to the creep crack variation during the tests Δa_c. The specimen data for 2D and 3D FE simulations are reported in Tab. 4.3 where a_0 is the initial crack size, K_0 is the initial stress intensity factor, P is the applied load, and Δa_c is the final creep crack propagation.

Both FE analyses consists in two different time steps. The first lasts 1 hour and is a simple elastic-plastic step where the test load is applied. The second is a visco-elastic-plastic step that lasts the amount of time needed to reach the maximum creep crack propagation Δa_c allowed.

2D model

Because of symmetry only half of the C(T) specimen was modeled as shown in Fig. 4.13. A section thickness equal to the net section thickness B_n was given to the model and as a consequence the applied load P was changed with respect to the experimental data in order to obtain the same initial stress intensity factor K_0. Thus the load P was applied to a reference point RF that was coupled to a rigid body coincident with the pin hole. To the reference point only vertical displacements were allowed. The ligament section represented by the thick black line of Fig. 4.13 was constrained on a rigid surface through a multi point constraint implemented, together with the damage formulation, in the user-defined MPC.for subroutine that allows the sliding of the ligament in the crack propagation direction. This subroutine acts by constraining the vertical displacement of all the points lying along the ligament unless the value of damage at the integration points, close to the nodes at the crack tip (black points of Fig. 4.14 (b)), is greater than 0.99. When this condition is verified in both integration points, the crack tip node is then released causing a crack propagation of the same size of the element size L_{el}. The refined mesh, in a region with a length equal to Δa_c, is illustrated in Fig. 4.14 (a). An element size of 100 μm was adopted because it is of the same order of magnitude of the average P91 grain size, although, other element sizes were, also, studied in order to investigate the mesh dependency of the numerical results.

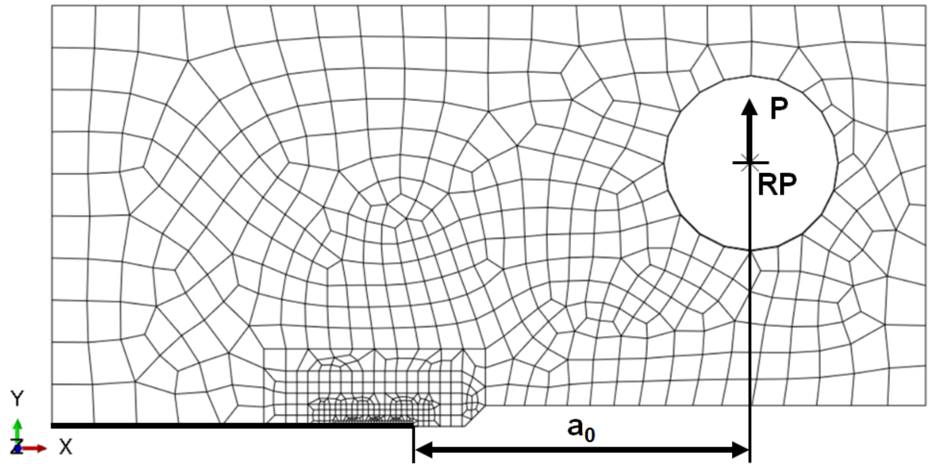

Figure 4.13: *Schematic diagram of the 2D FE model.*

3D model

Because of symmetry only a fourth of the C(T) specimen was modeled according to Fig. 4.15. In order to improve the mesh quality, the starting notch of the C(T) specimen was not reproduced. Once again the viscous behavior is modeled with the same user-defined subroutine CREEP.for while the damage and the crack propagation are modeled by the user-defined subroutine USDFLD.for. The damage model is the same ductility exhaustion approach used in 2D analyses, while the crack propagation is modeled in a different way. The subroutine defines the elastic modulus E as a function of the user-defined field variable, i.e. the damage ω according to Tab. 4.4. Thus, as soon as the damage ω reaches 0.99 at the crack tip node, the elastic modulus of the adjacent element, is slowly reduced to a unitary value as shown in Fig. 4.16. With a unit value of elastic modulus, the element is no longer able to support any stress causing the crack

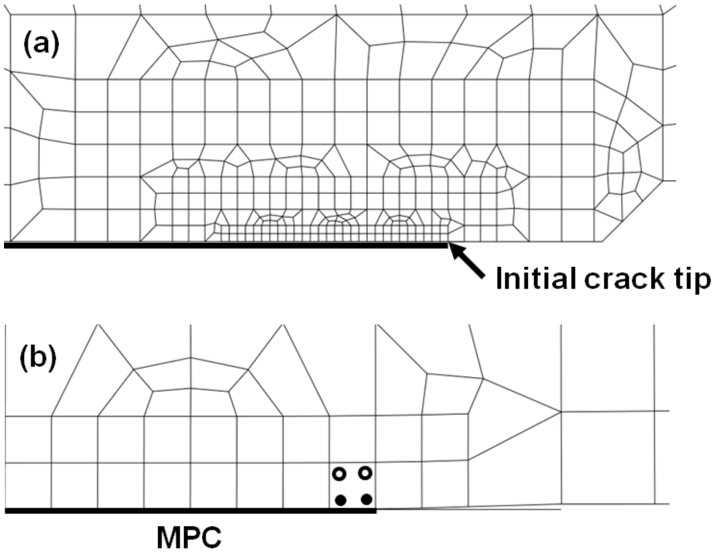

Figure 4.14: *Mesh detail close to the crack tip.*

Table 4.4: *Elastic modulus dependence on the field variable ω.*

E [MPa]	ω
147016	0
147016	0.99
1	1.00

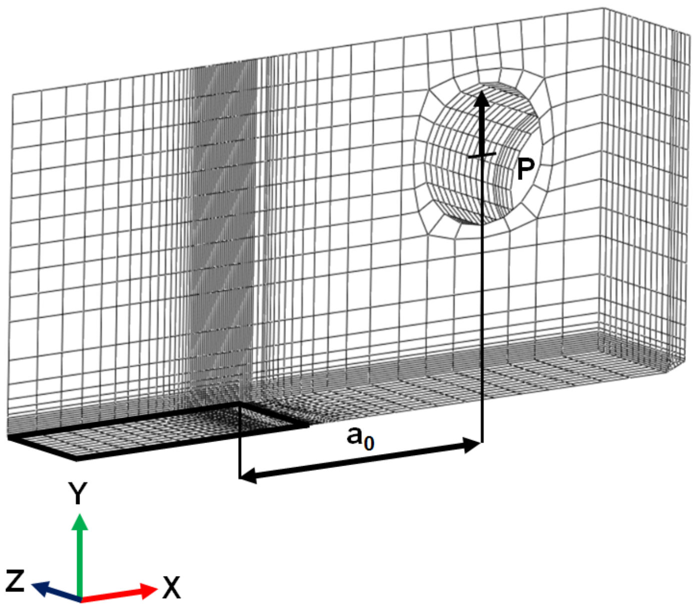

Figure 4.15: *Schematic draw of the 3D model.*

propagation. The load was applied to a reference point that was coupled to the cylindric

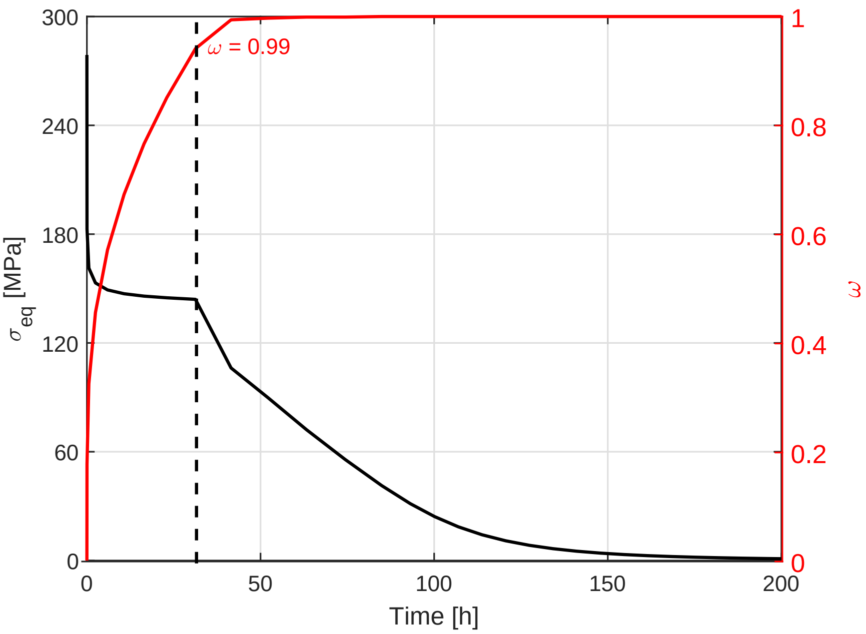

Figure 4.16: *Damage and stress evolution in one node of the 3D FE simulation.*

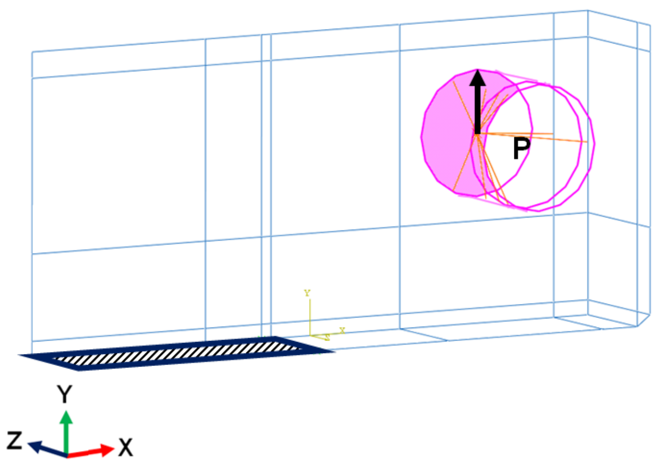

Figure 4.17: *Schematic diagram of the load coupling and the ligament section in the 3D FE model.*

section in magenta of Fig. 4.17. Symmetry boundary conditions were applied to the ligament section (dotted area of Fig. 4.17) and the midline section of Fig. 4.18 . In order to fully replicate the CCG tests a curvilinear crack front was given to each model according to the experimental pre-crack front sizes measured in nine points as shown in Fig. 4.19. Close to the crack tip the mesh was refined with an average element size of 100 μm as illustrated in Fig. 4.20. As per the 2D model, other element sizes will be studied in order to identify the mesh dependence of the numerical solution.

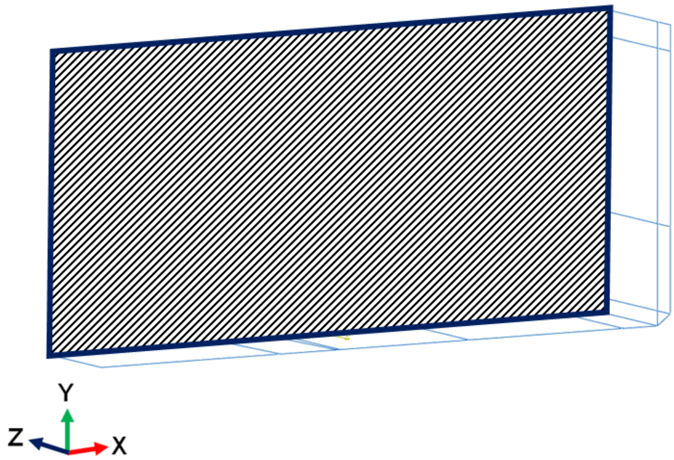

Figure 4.18: *Schematic diagram of the midline section in the 3D FE model.*

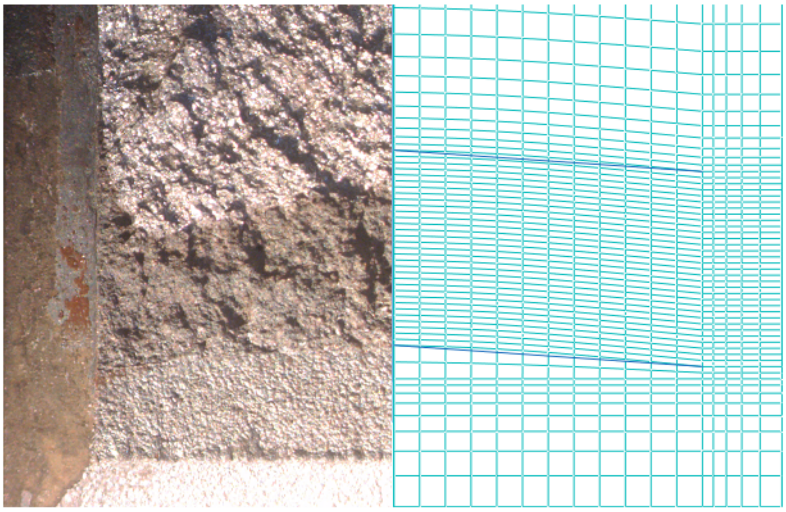

Figure 4.19: *Comparison between the experimental and numerical initial crack front.*

4.3.1 CCG Model Results on C(T) Specimens

All the FE simulations at different initial stress intensity factors are performed until the maximum creep crack growth allowed Δa_c was reached. Results in terms of crack propagation as a function of time are shown in Fig. 4.21. A good estimation of the crack propagation rates has been achieved numerically at different stress intensity factor levels for the correspondent uniaxial creep ductility values ε_f = 0.13 and 0.24 for 2D and 3D simulations respectively. A comparison between the predicted and experimental rupture times t_R is plotted in Fig. 4.22. It might be worth noting that the numerical model always underestimate the actual rupture time bringing to a conservative solution.

The 3D simulations are also able to provide the morphology of the final crack front. In Fig. 4.23 the fracture surface of the test performed at K_0 = 15 MPa m$^{0.5}$ is shown

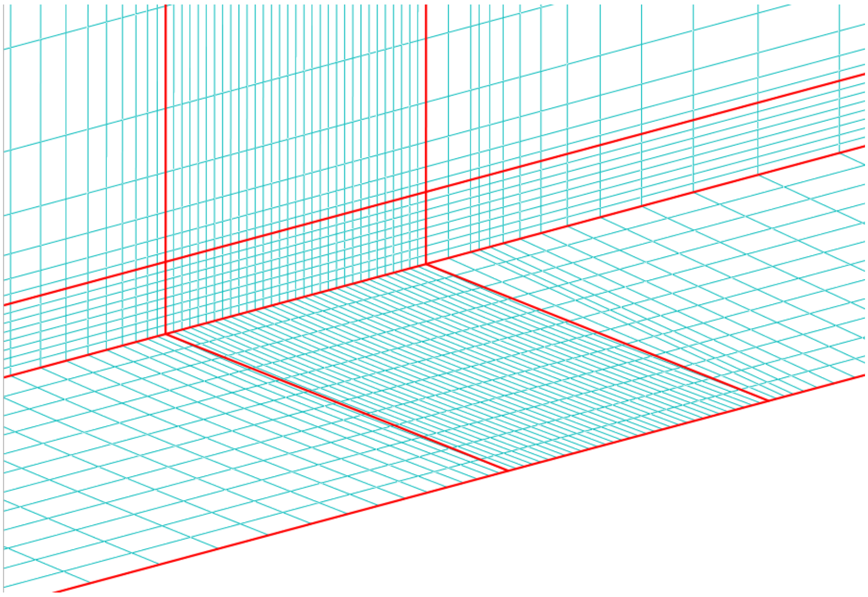

Figure 4.20: *Mesh refinement close to the crack tip.*

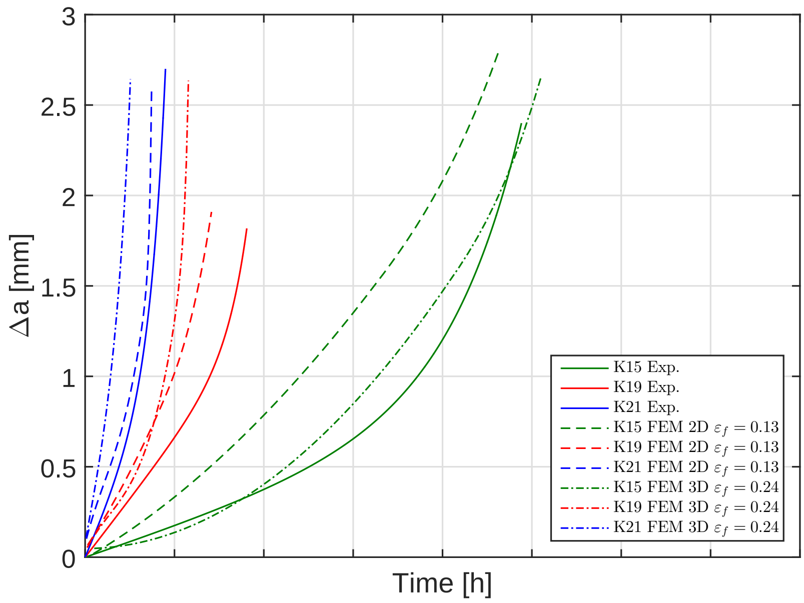

Figure 4.21: *FE results in terms of crack propagation as a function of time at different stress levels.*

and compared with the equivalent finite element simulation. The crack front is well predicted including the lateral surface of the C(T) specimen that is interested by a faster crack propagation since the stress field is affected by the presence of the side grooves. In order to be able to give a numerical estimation of C^* i.e. the crack tip parameter in CCG conditions, the crack propagation rate shall be considered in combination with the load-line displacement (LLD) rate $\dot{V}_t$ as demonstrated in Sec. 1.1.1. For this purpose

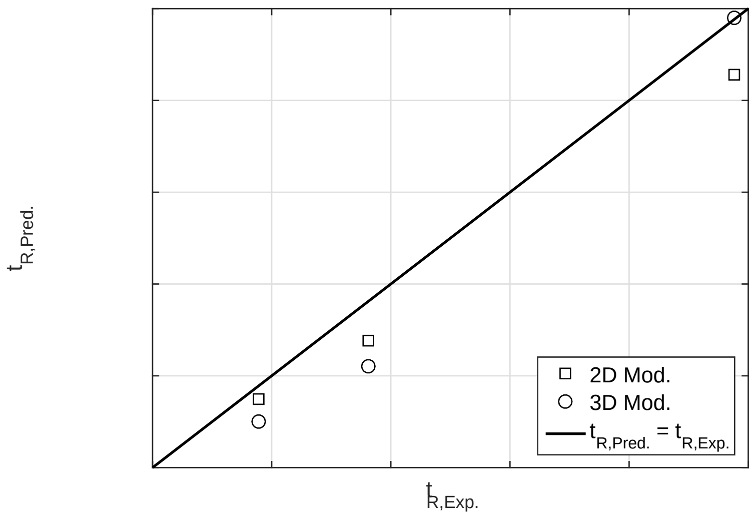

Figure 4.22: *Comparison between the predicted and experimental rupture times of the C(T) specimens.*

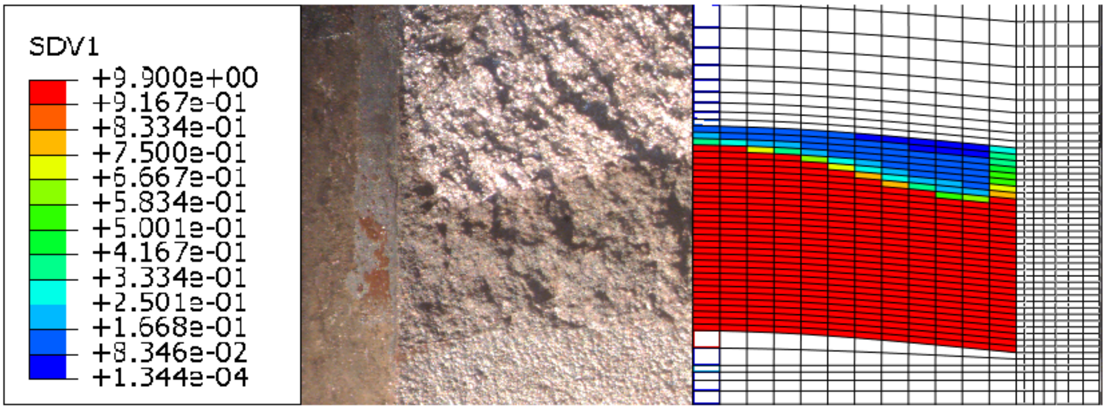

Figure 4.23: *Fracture surface at the end of CCG test performed at K_0 = 15 MPa m$^{0.5}$.*

in each FE simulation an additional history output has been requested: the vertical displacement of the load-line reference point RF. This value has been compared with the experimental one obtained during the tests by the LVDT instrumentation in Fig. 4.24. The results show that the LLD is correctly predicted for the test at K_0 = 15 MPa m$^{0.5}$ only. In fact the load-line displacement of the remaining tests is significantly underestimated. In Fig. 4.25 the load-line displacement rate is shown as a function of time. It might be worth observing how the correlation between the experimental and numerical results is missing especially in the first part of the curve. In this region the LLD is purely related to the creep deformation while in the linear and final regions it is mostly governed by the crack propagation rate. This is an indication that the viscous behavior of primary creep is not yet well represented. This might be due to limited uniaxial creep data that covers a stress range until 160 MPa. This limit is not enough

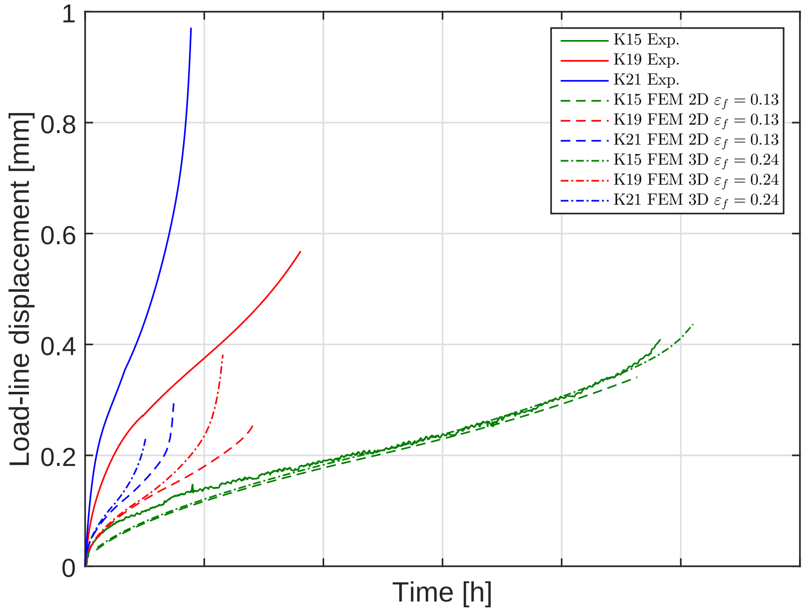

Figure 4.24: *Load-line displacement as a function of time.*

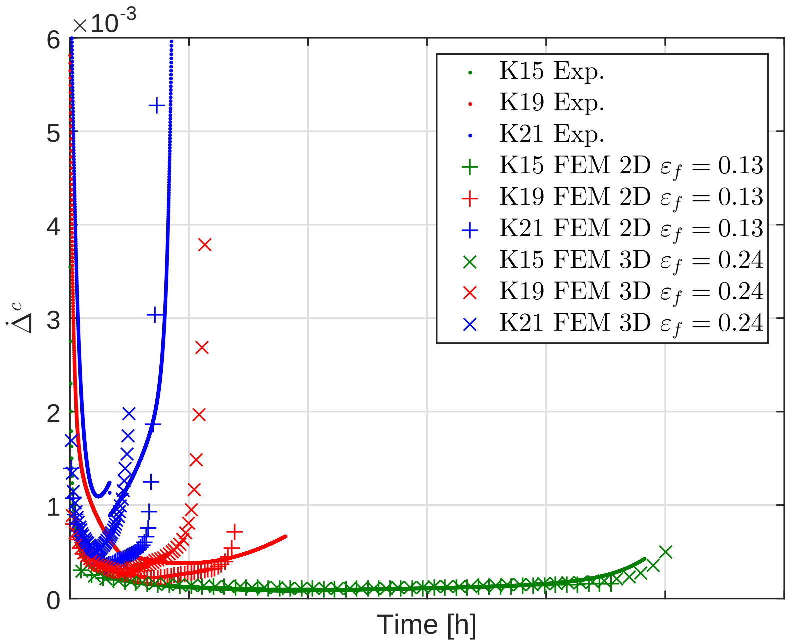

Figure 4.25: *Load-line displacement rate as a function of time: comparison between experimental and numerical results.*

to comprehends the stress intensification that happens at the crack tip at high stress intensity factors.

Sensitivity analysis to uniaxial ductility

As previously anticipated, the P91 creep data fitted in Sec. 4.1 provided a large scatter of uniaxial ductility ranging from values of 0.04, found at $\sigma = 20MPa$, until 0.37 found at $\sigma = 160MPa$. The optimum values of 0.13 and 0.24 have been found with reference to 2D and 3D simulations respectively. In Fig. 4.26 the results of the model sensitivity to ε_f are shown and compared with the experimental test performed at $K_0 = 15MPam^{0.5}$ in terms of crack propagation (a) and load-line displacement (b). The 3D model is clearly more affected by the ductility variation than the 2D model. Its rupture time t_R is significantly reduced to approximately 1/5 of the experimental data. The optimized value $\varepsilon_f = 0.24$ for 3D simulations represent the experimental creep data obtained at high stresses while the value of 0.13 for 2D simulations is more close to the results at low stresses. This suggests that the 3D model is more accurate since the stress field at the crack tip is high because of stress triaxiality and thus a higher value of ε_f is needed. A net specimen thickness B_n of 10.1 mm might be too short to verify the hypothesis of testing in purely plane strain conditions. If an intermediate condition between plane strain and plane stress is considered, the crack growth rate of the 2D simulation would increase. Thus a higher uniaxial ductility would be needed in order to slow down the crack growth to a level comparable with the experimental crack growth rate.

Numerical estimation of the C^* parameter

The load-line displacement rate together with the crack propagation rate can be used to evaluate the crack tip parameter in CCG conditions. According to the ASTM standard E1457 [6] the C^* parameter is calculated as suggested in Eq. (4.28).

$$C^* = \frac{P\dot{V}_c}{B_n(W-a)}\left[2 + .522\left(1 - \frac{a}{W}\right)\right]\frac{n}{n+1} \tag{4.28}$$

From numerical simulations performed at $K_0 = 15MPam^{0.5}$, thanks to the definition of a crack tip, it is also possible to estimate the C(t) integral that is able to describe the crack growth in different creep conditions. In small-scale creep regime it is path dependent and thus needs to be calculated through a limited crack tip contour in order to confine the problem to an area where the stress-strain fields are purely dominated by creep rather than elasticity. In steady-state creep conditions, after the transition time t_T is passed, the C(t) integral becomes path independent trending to the same value of C^*. The transition time of $t_T = 35$ hours has been determined experimentally and numerically according to Eq. (1.34). Thus the comparison between experimental C^*, C^* calculated by LLD and crack propagation rate of numerical simulations and C(t) integral is proposed in Fig. 4.27. All the data prior to the transition time were excluded.

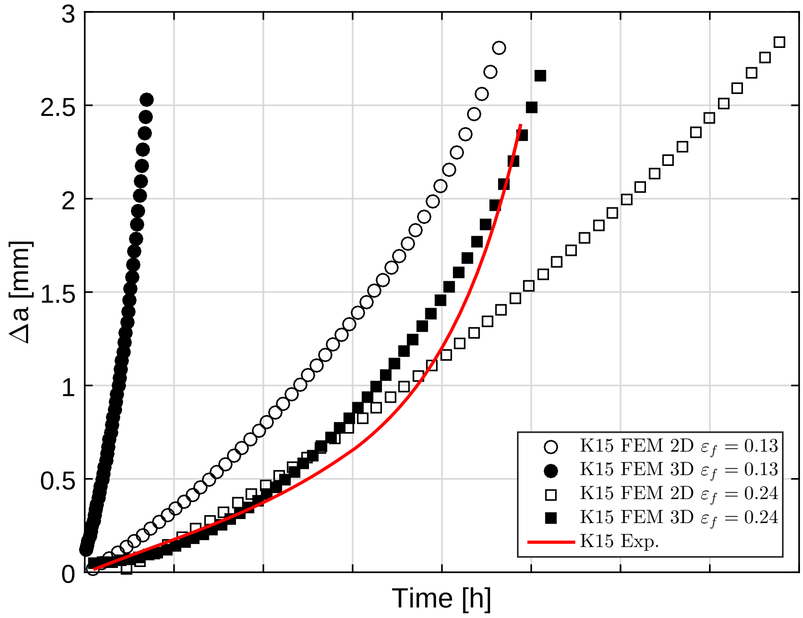

(a) *Crack propagation.*

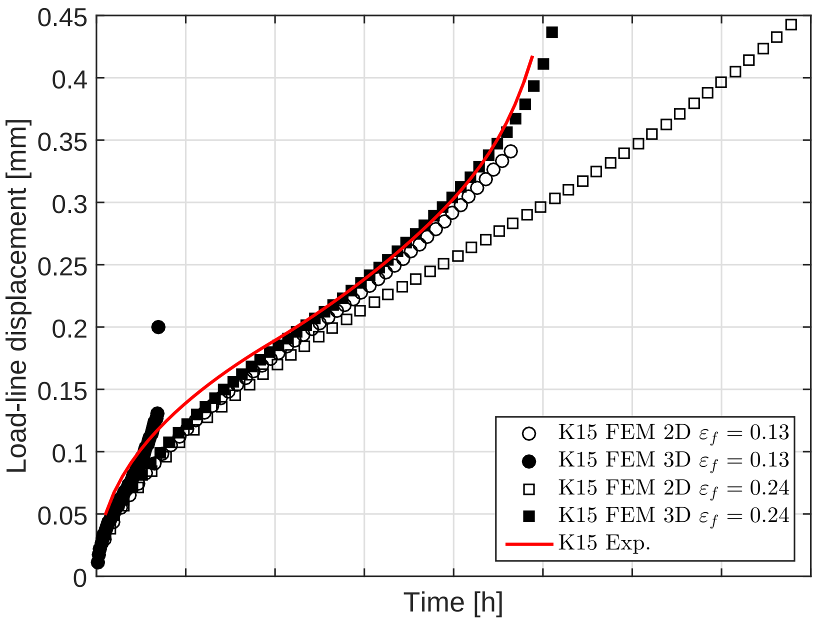

(b) *Load-line displacement.*

Figure 4.26: *Sensitivity analysis of the uniaxial creep ductility.*

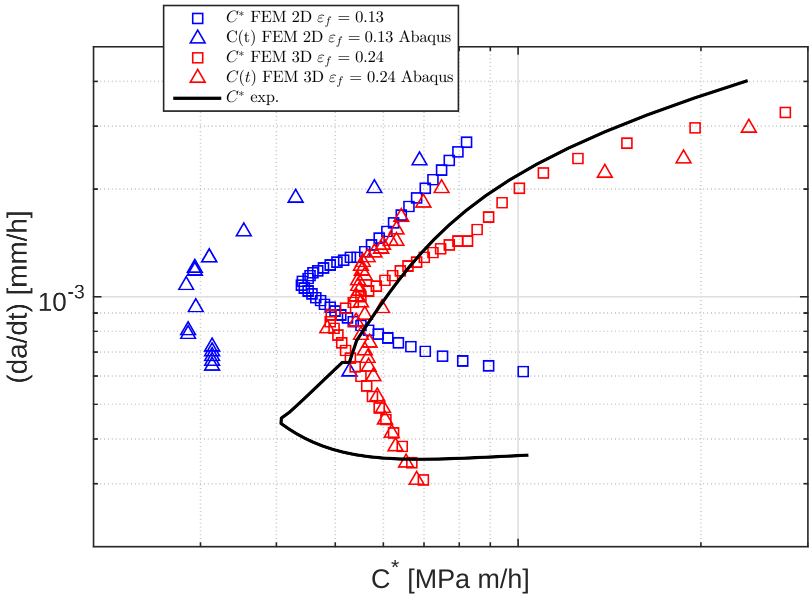

Figure 4.27: *Comparison between the C^* and $C(t)$ integral obtained: experimentally from CCG test of P91 at $K_0 = 15MPam^{0.5}$, from crack propagation and LLD data derived by numerical simulations and from Abaqus calculation of the $C(t)$ integral using crack tip contours.*

The 3D model exhibits a similar behavior of C^* and $C(t)$ integral while the 2D model shows a significant difference between the two parameters. In spite of that the crack tip parameters obtained with the simulations fall in the experimental range provided by the test performed at $K_0 = 15MPam^{0.5}$. However it is interesting to note how the power-law relationship of Eq. (1.19) is lost at low crack propagation rates, i.e. at the beginning of the CCG. This indicates that the transition time t_T of 35 hours might be too short to reach extensive creep conditions. This means that the creep zone is not yet large enough with respect to the elastic and plastic zones. Under these conditions the relationship provided by Eq. (1.19) is no longer unique.

4.4 CCG Model of a pressurized cracked cylinder

Since the combination of the Graham-Walles creep model and the modified void growth theory by Cocks and Ashby provided a good estimation of the CCG resistance of C(T) specimens, the 3D FE model was extended to predict the behavior of a pressurized cylinder with a pre-existing axial defect on the inside surface.

The geometry analyzed in this Section is shown in Fig. 4.28 and features an initial crack size with $a = 5\%w = 0.555$ mm, and $a/(2c) = 0.025 \rightarrow c = 11.1$ mm. Due to the axial symmetry of the model, only 1/8 of the pipe was analyzed in order to reduce the computational time. The pipe geometry consists of two different parts that were

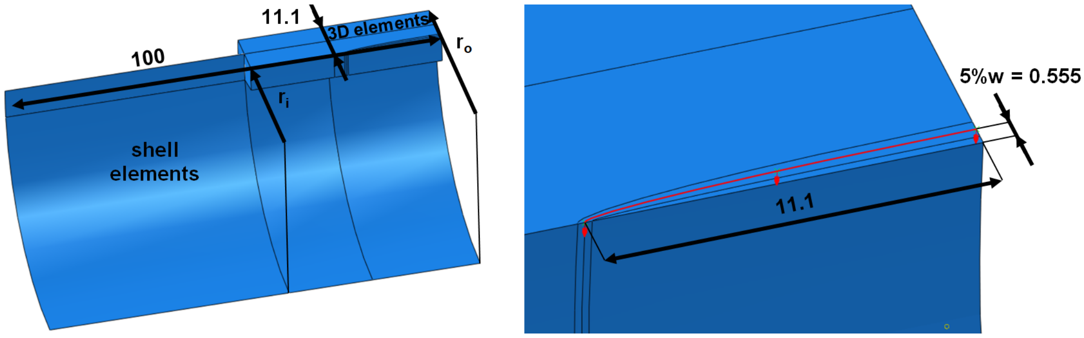

Figure 4.28: *Finite element model of the pressurized pipe with an axial defect on the inside surface.*

analyzed with different element types: 2D 8-node doubly curved thick shell elements with reduced integration for the further region from the crack tip,, and 3D 20-node quadratic brick elements with reduced integration for the region in proximity of the crack tip. Splitting the model in two parts was fundamental to further reduce the size of the problem. The shell to solid coupling constraint of Fig. 4.29 was applied in order to transfer stresses from one region to the other. The same elastic-plastic properties of

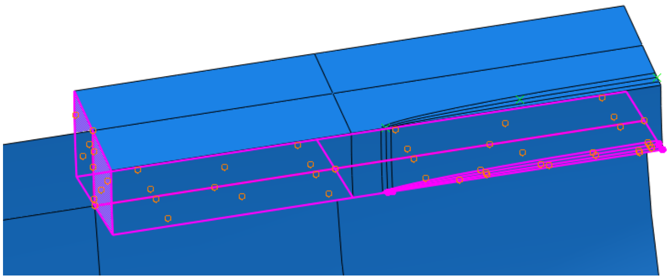

Figure 4.29: *Representation of the shell to solid coupling constraint between the 2D and the 3D element regions.*

the FE model for the C(T) specimen were used, while the creep behavior, the crack tip damage, and the crack propagation, were modeled with the combination of CREEP.for and USDFLD.for user-defined subroutines previously discussed for the 3D C(T) model. An internal pressure load of 25 MPa was applied to the model together with an axial stress $\sigma_{ax} = 32.2$ MPa that was calculated from the thick walled pipes formulations of Lame. The boundary conditions are represented in Fig. 4.30 and consist in the circumferential symmetry of the pipe thickness and the axial symmetry. The mesh size close to the crack tip was built in order to guarantee an average element size $L_{el} = 100\mu m$ comparable to the one used in C(T) specimen simulations. The detail of the mesh is shown in Fig. 4.31. The simulation consists in two steps: a first static step where the pressure load is applied followed by a second step, where the viscous behavior of the material is evaluated together with the creep damage distribution and the crack prop-

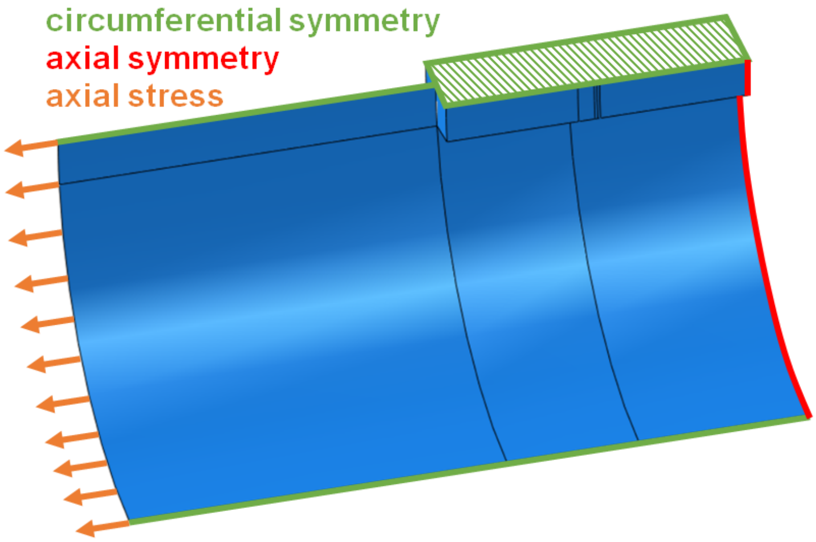

Figure 4.30: *Schematic representation of the boundary conditions of the FE pipe model.*

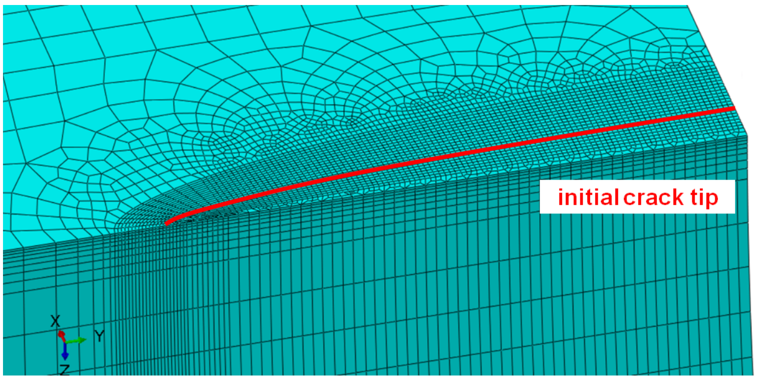

Figure 4.31: *Detail of the mesh at the crack tip.*

agation. A maximum time of 200000 hours was simulated according to the analytical residual life estimations of Sec. 3.2.

The results of the FE simulation performed on the pressurized pipe exhibited an initial damage concentration on the plane strain section as shown in Fig. 4.32 (a) where the creep damage contours are plotted over the crack tip region. The crack propagation, i.e. a creep damage greater than 0.99, starts at a time $t = 78400$ h on the symmetry section of the FE model (Fig. 4.32 (b)) and reaches the plane stress section at a time $t = 133000$ h as shown in Fig. 4.32 (c). The simulation ended at 157000 hours reaching a crack propagation of 0.4 mm in the plane strain section and 0.2 mm in the plane stress section as shown in Fig. 4.32 (d). The FE analysis stopped because the minimum increment time of 1E-30 hours was reached indicating the beginning of a propagation phase characterized by high crack propagation rates. The crack propagation in the three regions on the crack tip A, B, and C is illustrated in Fig. 4.33 showing a crack initiation of 0.2 mm at approximately 10^5 hours. The plane strain crack propagation recorded at the end of the simulation is consistent with the average creep crack growth prediction provided by the API 579 procedure illustrated in Fig. 3.8 (b).

The FE model described in this Section is also applied to perform a numerical evaluation of the $C(t)$ integral distribution along the crack front. Since creep crack propagation introduces a discontinuity in the $C(t)$ calculation, the model has been modified in order to represent the early stage of steady-state creep damage, where the crack is stationary. With this method, the $C(t)$ integral estimation by FE software, is not affected by numerical errors but, in the meantime, accounts for the creep damage since the user-defined subroutine CREEP.for, based on the Graham-Walles model, is still applied. The $C(t)$ integral has been calculated on eight different crack tip contours along the entire crack front. The maximum time for the simulation has been set to 80000 hours because in this amount of time, no significant crack propagation occurs.

The crack tip contours provided by the FE simulation have been analyzed in the three regions A, B, and C of Fig. 4.33. In all the three regions, among the eight crack tip contours, the third one provided the highest $C(t)$ values without being affected by numerical singularity and thus it is the one shown in Fig. 4.34. The numerical simulation confirmed that the plane strain region is the one interested by an higher $C(t)$ integral with respect to the rest of the crack front. The plane stress region is interested by the minimum $C(t)$ integral and, as seen in the previous numerical simulations, is characterized by a slower crack propagation than the plane strain section. Moreover, the $C(t)$ estimation at point A, is also consistent with the analogous estimation performed by means of the API 579 approach based on the C_t parameter validating the FE model described so far.

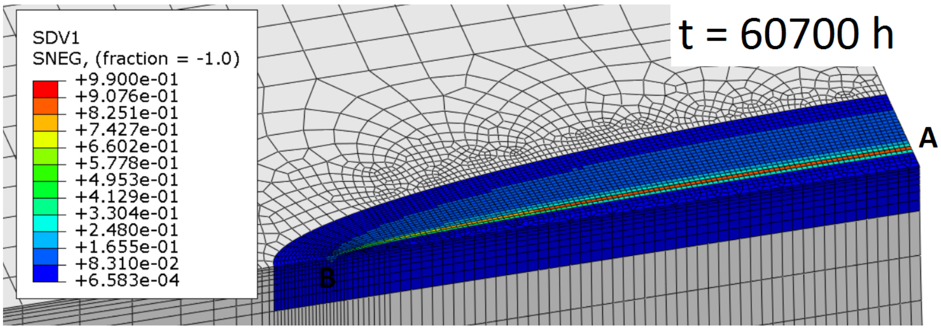

(a)

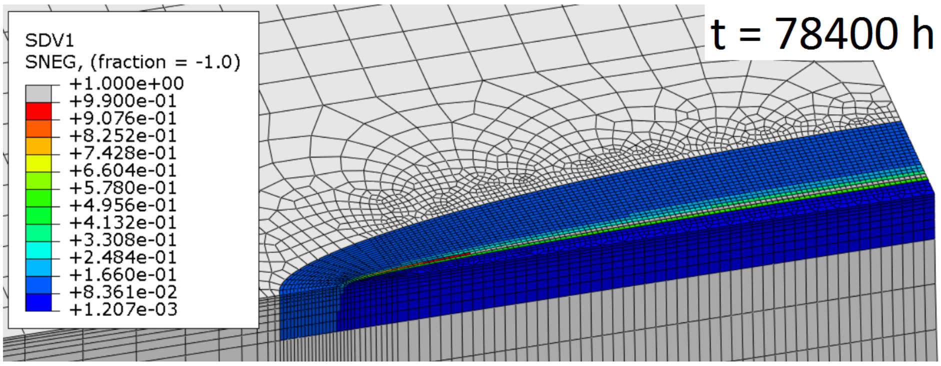

(b)

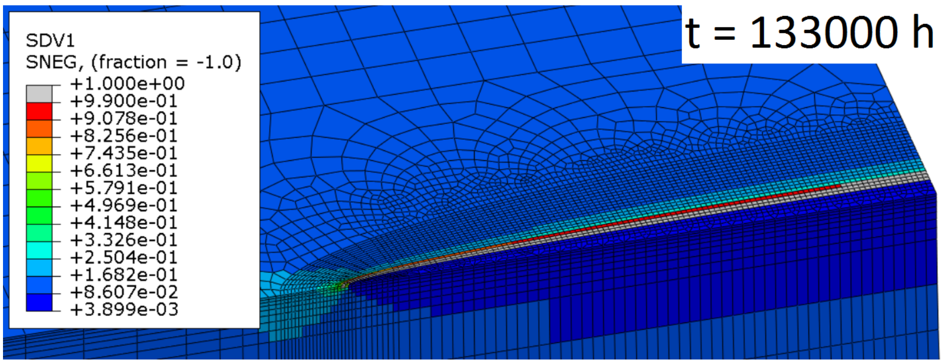

(c)

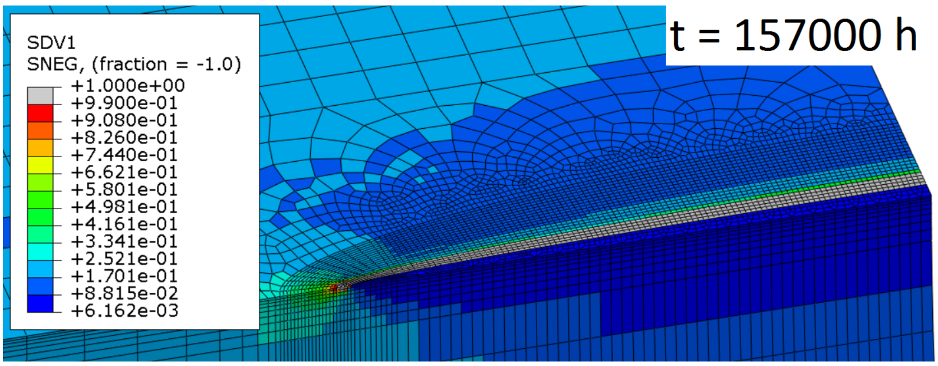

(d)

Figure 4.32: *Evolution of the creep damage ω along the crack front.*

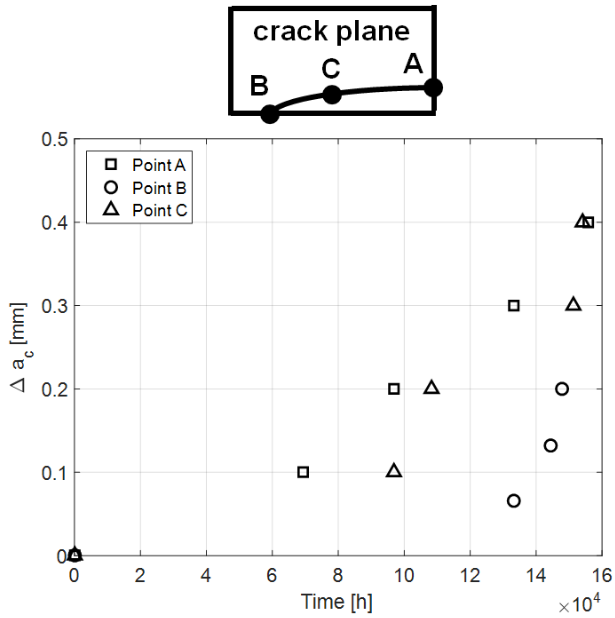

Figure 4.33: *Creep crack propagation in three regions at the crack tip.*

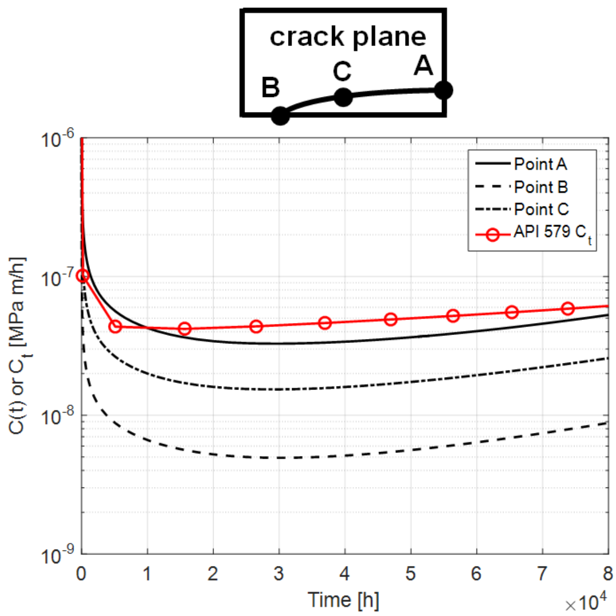

Figure 4.34: *Comparison between the $C(t)$ integral numerically evaluated in three crack tip regions and the C_t parameter according to API 579 [5].*

4.5 CFCG Numerical Simulations

In this Section the preliminary study of a CFCG model based on the combination of the Chaboche cyclic plasticity model [13] and the averaged Norton law of Sec. 2.1. The model was applied first to simulate cyclic plasticity in Low Cycle Fatigue (LCF) tests in presence of hold time and then was applied to evaluate the interactions within the creep zone size, the monotonic plastic zone, and the cyclic plastic zone.

4.5.1 Cyclic Plasticity Model

The non-linear kinematic hardening model by Chaboche is based on the definition of a yield surface:

$$f(\sigma - \alpha_c) = \sigma_0 \tag{4.29}$$

where σ is the stress tensor, α_c is the backstress tensor, and σ_0 is the yield stress. The yield surface is usually defined in the deviatoric space assuming the following expression:

$$f(\sigma - \alpha_c) = \sqrt{\frac{3}{2}(S - \alpha^{dev}) : (S - \alpha^{dev})} \tag{4.30}$$

where S is the deviatoric stress tensor and α^{dev} is the deviatoric part of the backstress tensor. The plastic strain increment can be obtained by using the normality flow rule:

$$\dot{\varepsilon}^p = \frac{\partial(\sigma - \alpha_c)}{\partial\sigma}\dot{\bar{\varepsilon}}^p \tag{4.31}$$

where the equivalent plastic strain increment is defined as:

$$\dot{\bar{\varepsilon}}^p = \sqrt{\frac{2}{3}\dot{\varepsilon}^p : \dot{\varepsilon}^p} \tag{4.32}$$

The isotropic hardening gives the change of the yield stress as a function of the accumulated equivalent plastic strain. In the FE software Abaqus, the isotropic hardening is considered by using a Voce type equation:

$$\sigma_0 = \sigma|_0 + Q_\infty \left(1 - e^{-b_c\bar{\varepsilon}^p}\right) \tag{4.33}$$

where $\sigma|_0$ is the yield surface size at zero plastic strain, and Q_∞ and b_c are additional material parameters that shall be calibrated from cyclic test data. The kinematic hardening is described through a non-linear kinematic law. The overall backstress is composed of multiple backstress components, where the evolution of each backstress component is defined as:

$$\dot{\alpha}_k = C_k\dot{\bar{\varepsilon}}^p\frac{1}{\sigma_0}(\sigma - \alpha_c) - \gamma_k\alpha_k\dot{\bar{\varepsilon}}^p \tag{4.34}$$

and the overall backstress is computed from the relation:

$$\alpha_c = \sum_{k=1}^{N_{bs}} \alpha_k \tag{4.35}$$

where N_{bs} is the number of backstress and C_k and γ_k are material parameters. The material parameters that were used in the cyclic plasticity model by Chaboche, were taken from a technical report containing LCF and ratchetting tests performed at 600 °C on the modified P91 steel of Tenaris (Tab. 4.5). As previously discussed the deformation

Table 4.5: *Cyclic plastic model parameters for P91 at 600 °C.*

σ_0	Q_∞	b_c	N_{bs}	C_1	C_2	C_3	γ_1	γ_2	γ_3
220	-100.9	0.9	3	140105	17701	2499	2000	333.3	1

associated to creep damage was modeled through a simple Norton power law because the application of the Graham-Walles model of Sec. 4.1 resulted in convergence problems during the loading-unloading phases of the fatigue cycles. The averaged Norton law coefficients of Tab. 2.3 were used in the FE model. The combined cyclic plasticity and creep model was first verified by replicating the two test conditions reported in Tab. 4.6 derived from the LCF tests with hold time where R_ε is the strain ratio and ε_a is the strain amplitude.

Table 4.6: *LCF with hold time test conditions.*

Specimen:	R_ε	t_h [h]	ε_a [mm/mm]	$\dot{\varepsilon}$ [mm/mm/s]
Test1	0.5	1	0.0025	0.001
Test2	0	1	0.0025	0.001

4.5.2 CFCG Model: FE Framework

Due to symmetry, the LCF specimen geometry of Fig. 4.35 was modeled by considering half of the gauge length with 4-node bilinear axisymmetric quadrilateral elements. The element size in all the gauge length considered was kept equal to 50 μm. As shown in Fig. 4.35 the load was obtained by imposing a uniform displacement on the upper surface of the numerical model. The load, hold, and unload phases were obtained by defining a strain amplitude that reaches its maximum during the loading phase according to the predefined strain rate of 0.001 mm/mm/s, remains constant during the hold phase, and reaches the minimum strain during the unload sequence with the predefined strain rate. During the simulation, the vertical reaction force at the loading point was acquired together with the vertical strain at the gauge length at equidistant time points. The Chaboche model parameters were given as the plastic properties for the FE model

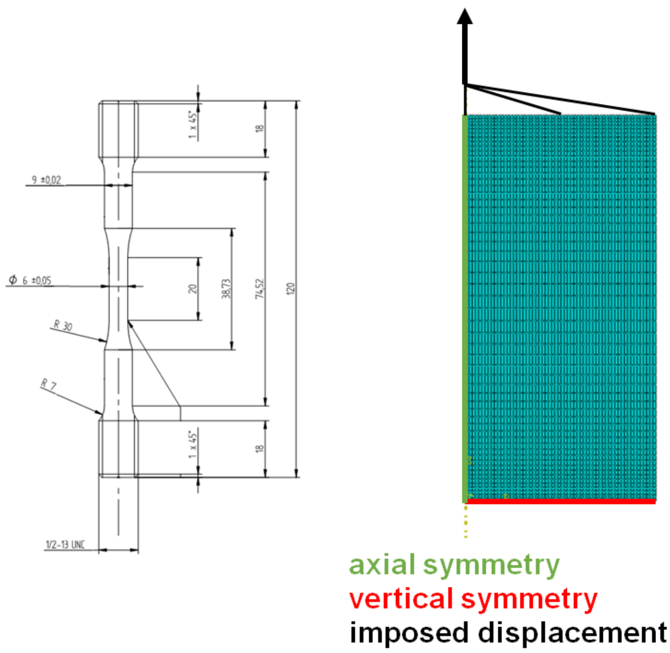

Figure 4.35: *LCF test specimen geometry and FE model.*

while the Norton law coefficients, were implemented in a CREEP.for user-defined subroutine.

4.5.3 CFCG Model Results

In Fig. 4.36, the results of FE simulations are compared with the experimental tests of Tab. 4.6 in terms of cyclic plastic curves at the first ($N = 1$) and last fatigue cycle ($N = 25$). The combination of the cyclic plasticity model and the averaged Norton law is able to numerically predict the experimental tests at different strain ratios. For this reason, the CFCG model has been used to characterize the evolution of the creep, the monotonic plastic, and the cyclic plastic zones during CFCG tests. In Fig. 4.37 the extension of these zones is shown for a CFCG test with $t_h = 0.1$ h at the end of the second cycle. This study, which is currently under investigation, might lead to a new approach to numerically evaluate the creep reversal parameter C_R, overcoming the difficulties found during the experimental evaluation at short hold times. However, to reach this relevant result, numerical problems have to be solved in order to simulate the evolution of the creep, plastic, and cyclic plastic zones at higher number of cycles.

4.6 Summary

The importance of a valid uniaxial creep model that is able to represent the material's behavior even in a FE environment has been discussed. For this purpose the continuum

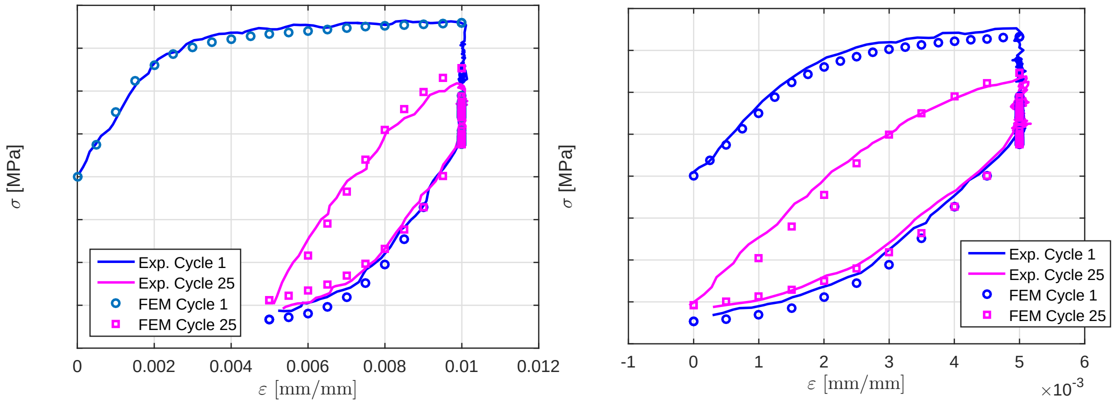

(a) $R_\varepsilon = 0.5, \varepsilon_a = 0.0025$.

(b) $R_\varepsilon = 0, \varepsilon_a = 0.0025$.

Figure 4.36: *Results of the visco-cyclic plastic FE model and comparison with the experimental data.*

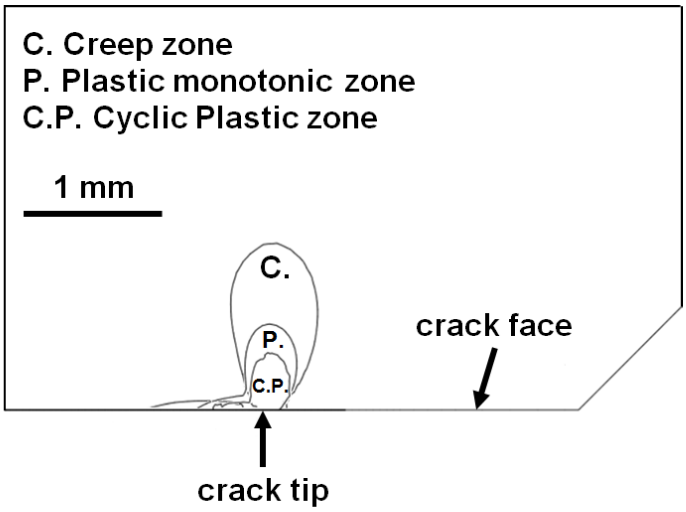

Figure 4.37: *Creep, plastic, and cyclic plastic zones predicted by FE analysis at the end of the second cycle of a CFCG test with $t_h = 0.1$ h.*

damage mechanics based models of Kachanov [35] and Liu-Murakami [39] and the Graham-Walles model [26] were studied and fitted to the uniaxial creep data of Fig. 2.3. The time dependent models of Kachanov and Liu-Murakami exhibited numerical issues when applied to FE. The short increment times required to converge at the beginning of the numerical solutions, caused premature creep strain. This issues were solved by changing to the strain dependent model by Graham-Walles. Once its FE applicability was verified by means of creep simulations that gave a good correlation with the experimental data, the uniaxial problem was extended to its multiaxial case. With this aim a modification of the cavity growth theory by Cocks-Ashby [14] was used to predict CCG through a plane strain (2D) and a 3D FE model of the C(T) specimen. Considering the large scatter deriving from experimental data, the uniaxial creep ductility used in the simulations was used as an optimization parameter. Plane strain and 3D simulations provided a good correlation with experimental creep crack growth rates and a good estimation of the load-line displacement at low stress intensity factors only. This suggests that the range of stresses covered by the Graham-Walles model fit shall be extended by means of additional uniaxial creep models at higher stresses. For the case study $K_0 = 15$ MPa m$^{0.5}$ the load-line displacement and crack propagation records from numerical simulations have been used to recalculate the crack tip parameter C^* showing a good prediction when compared with the experimental data as well as with the numerical estimation provided by Abaqus software. However the first hours after the transition time t_T from small-scale to extensive creep conditions as per ASTM E1457 [6], confirmed the absence of a unique relationship between crack propagation rates and C^* as previously observed in Sec. 2.2.2.

The 3D model of the C(T) specimen was extended to characterize CCG in a pressurized cylinder with an axial defect on the inside surface. The results of the FE simulation, highlighted the creep damage evolution on the pipe, that starts from the plane strain symmetry section and spreads up to the plane stress section.

The same numerical model for the pipe was analyzed under stationary crack conditions in order to predict the stabilized value of the crack tip integral $C(t)$ in EC conditions i.e. C^*. The FE model provided a good prediction of the integral $C(t)$ in agreement with the API 579 [5] estimation, based on the C_t parameter, evaluated for the same geometry.

A preliminary study to numerically describe the creep-fatigue interactions was also presented. A CFCG model was proposed, based on the combination of the cyclic plasticity model by Chaboche [13] and the Norton law of Eq. (1.1), in order to predict the LCF behavior of the modified P91 when a hold time is applied during the fatigue cycle. The model provided a good correlation with the experimental data at different strain ratios R_ε and for this reason, it has been used to assess the creep, plastic, and cyclic plastic zones interaction during the first cycles of a CFCG test, on a C(T) specimen, with a hold time $t_h = 0.1$ h. The results have shown that from the end of the second hold cycle, the creep zone size is dominant with respect to the plastic and cyclic plastic zones. In this context, additional simulations will be performed in order to study the evolution of these zones, at higher number of cycles, after solving the issues given by the numerical discretization of the problem.

CHAPTER 5

Concluding Remarks and Further Developments

This thesis dealt with the study of the creep and creep-fatigue resistance properties of a modified P91 power plant steel. The methodological approach used in this work was strongly focused on the application of time-dependent fracture mechanics concepts in creep and creep-fatigue regime to components with the aim to:

- present a critical review of the classical approaches to high temperature assessments of such components that does not account for creep-fatigue interaction phenomena;
- discuss and validate a new approach to improve the quality of future assessments based on a fracture mechanics parameter able to describe the creep-fatigue interaction effects related to crack tip damage evolution;
- study a numerical approach to simulate time-dependent crack propagation in components by means of accurate FE analyses.

The starting point was the discussion of the crack tip parameters that govern the initiation and propagation of defects under creep and creep-fatigue regime, and their transposition to large scale components in order to analyze the effects of critical operating conditions, like high frequency load cycles, and over pressure. In addition to this, the finite element method was used to recreate not only the experimental test conditions but

also the crack tip parameters evolution in order to validate its application to estimate the residual life of components.
To support the methodological approach, an experimental campaign to collect homogeneous CCG and CFCG resistance data in order to characterize the intrinsic response of the material to high temperature and cyclic loads was presented.
In this thesis, Chapter 1 contained a comprehensive review of all the state-of-the-art crack tip parameters that describe CCG and CFCG in both specimens and components. Starting from the definition of the elastic-plastic crack tip parameter J integral, the time-dependent fracture mechanics C^* was introduced. Its empirical and analytical formulations made it a perfect candidate to characterize CCG in both testing specimens and components for whom it is possible to define a stress intensity factor. When analyzing small-scale or transition creep conditions, the C^* is replaced by the $C(t)$ that is defined at a small contour close to the crack tip, where creep zone is still dominant. However, considering its difficult experimental estimation, $C(t)$ was replaced by the C_t parameter easily measurable at the load-line. C_t, not only characterizes the CCG in small-scale creep, transition creep, and extensive creep but it is also measurable at the load-line and, as C^*, has an analytical formulation that make it extendable to different geometries. The ability to describe the crack tip stress fields in transient conditions, is also important in CFCG regime. From a modified expression of C_t the crack tip parameter in CFCG conditions $(C_t)_{avg}$ is defined. As the other crack tip parameters, $(C_t)_{avg}$ can be calculated at the load-line of testing specimens and, through analytical expressions under the hypotheses of complete and absent creep strain reversal due to cyclic plasticity, for complex geometries.
After having analyzed the main crack tip parameters that describe the crack propagation of defects under creep and creep-fatigue conditions, Chapter 2 includes a brief introduction of the modified P91 material object of this thesis. The elastic-plastic properties at high temperature and the uniaxial creep test data provided by Tenaris represented a starting point for the experimental campaign performed during this work. The Norton law and the Larson Miller parameters determined from uniaxial creep tests were fundamental in the description of the pure creep behavior, however, in presence of cracks, additional tests are required to describe the evolution of defects in HT conditions. CCG tests were performed at different initial stress intensity factors with the aim to: characterize the creep crack initiation through a power law relationship between the time and the stress intensity factor at initiation; determine the crack tip parameters of time-dependent fracture mechanics. The parameters C^* and C_t obtained from the experimental CCG data of crack propagation and load-line displacement were correlated to the crack propagation rates through a power law relationship. In creep-fatigue

conditions, CFCG tests were performed to assess the effects of different hold times and initial stress intensity factor ranges. The load-line displacement records, were used to estimate the crack tip parameter $(C_t)_{avg}$ that correlates the average crack propagation rate $(da/dt)_{avg}$. Due to the difficult estimation of the load-line deflection during short hold times, the $(C_t)_{avg}$ was also estimated according to its analytical formulation under the hypothesis of complete creep reversal and partial creep reversal after the experimental determination of the creep reversal parameter C_R. Fatigue crack growth tests performed at 600 °C were used to identify the Paris-Erdogan law for P91 and combine it with the $(C_t)_{avg}$ parameter in order to apply a superposition model that provides creep-fatigue crack propagation by summation of time-dependent and fatigue damage. In order to conclude the material's resistance map at high temperature, fracture toughness tests carried out according to the basic procedure of ASTM E1820 [17] provided the estimation of J_{IC} for the modified P91 that was later validated with FE simulations based on the key-curve method.
The correlation between the CCG and CFCG crack tip parameters and the crack propagation rates set the basis for the creep and creep-fatigue crack growth assessments of Chapter 3, where new flaw acceptability methods based on the combination of different approaches were presented. In CCG conditions, the Two Criteria Diagram contained in Fitnet [24] code was applied together with the reference C^* approach (C_{ref}) proposed in British Standard 7910 [12] to evaluate the evolution of different defect morphologies in a pressurized pipe. The Two Criteria Diagram for creep crack initiation estimation was built with the uniaxial creep data on the modified P91 provided by Tenaris, and the initiation data derived from the experimental CCG tests. The CCG was predicted by means of the C_{ref} approach under the hypothesis of a uniform stress distribution on the ligament section due to stress relaxation given by creep strain. The residual life estimations performed at different initial defect sizes, provided a good agreement when compared with the API 579 [5] approach based on the C_t parameter at the low internal pressure of 25 MPa and less conservative result at the critical high pressure of 50 MPa. However, it might be worth noting that, the conservative results of both approaches provided by BS 7910 and API 579 might be lost when assessing lower loading conditions, as observed from the comparison between the reference stress based crack tip parameters and the experimental crack tip parameters of C^* and C_t derived during CCG tests. With the purpose to propose an alternative CFCG assessment method for pressurized pipes with internal defects, the Time Dependent Failure Assessment Diagram suggested by R5 code [10] was analyzed in combination with the $(C_t)_{avg}$ approach under the hypothesis of partial creep strains reversal thanks to the creep reversal parameter C_R that was previously obtained from experimental CFCG tests on C(T) specimens. The latter

method considers the effective interaction between the creep and fatigue damages and does not model the creep-fatigue damage as a simple superposition between the two phenomena. In this proposed procedure, creep-fatigue crack initiation is predicted according to the TDFAD, that was personalized with the P91 experimental data derived from creep, CCG, and FCG tests. Creep-fatigue crack growth instead, was predicted after the definition of a $(C_t)_{avg}$ for the investigated component that was based on the C_R parameter and on an analytical formulation of the C^* parameter. The results of this method highlighted the effects of the hold time t_h: the shorter the hold time is, the faster the crack propagation is. However, when typical power plant hold times are considered, the detrimental effect given by the fatigue cycle does not play an important role in the residual life estimation. The defects acceptability assessments highlighted the need of an accurate crack tip parameter description in complex geometries.
The numerical simulations discussed in Chapter 4 were studied with this purpose. CCG required a deep material characterization in terms of creep resistance that was obtained by analyzing strengths and weaknesses of different uniaxial creep models. Among all the investigated models, the Graham-Walles was selected because it was able to represent complete creep curves at different stress conditions, without being affected by numerical integration issues. For this reason it was implemented in the FE software Abaqus through the user-defined subroutine CREEP.for in combination with a continuum damage mechanics approach based on a modified void growth theory by Cocks and Ashby [14], to predict CCG in C(T) specimens. The results of the FE model provided a good correlation with the experimental CCG data, as well as a good estimation of the crack tip parameter C^* derived from the numerical crack propagation and load-line displacement records of 2D and 3D simulations.
Hence, the model was extended to assess the creep damage distribution on a pressurized pipe with a semi-elliptical axial defect on the inside surface. The numerical simulation on pipe geometry highlighted a damage concentration in the plane strain section at the crack tip that slowly evolves to the plane stress section in agreement with the results obtained from the CCG assessments presented in Chapter 3. With the aim to analyze the creep fatigue damage interactions a preliminary study of a numerical CFCG model based on the combination of the Chaboche cyclic plasticity theory and the steady-state creep strain rate distribution according to the Norton law, was introduced. The FE model was able to correctly simulate the creep-fatigue interaction in LCF tests in presence of hold times. The same model was used to characterize the size of the creep, plastic, and cyclic plastic zones on a CFCG test, with hold time $t_h = 0.1$ h, on a C(T) specimen. The FE model showed a dominant creep zone already at the end of the second cycle while the size of the cyclic plastic zone is similar to the monotonic plastic

zone.

5.1 Further Developments

The results achieved in this thesis analyzed new strategies to assess time-dependent fracture mechanics in pipe components by means of analytical and numerical approaches that calls for further developments.

The proposed assessment procedure to evaluate CFCG in cracked pipes by means of the combination of the TDFAD and the $(C_t)_{avg} - (da/dt)_{avg}$ correlation, still relies on analytical estimations of the crack tip parameter C^*. In this context, a numerical estimation of the C^*, based on the CCG FE model presented in this thesis and validated on the investigated material, could enhance the accuracy of the residual life assessments without affecting reliability. *This improvement strongly demands for the study of different pipe and crack configurations that could be easily obtained thanks to additional FE analyses based on the user-defined subroutines examined during this work.*

The presented pipe FE model, that accounts for creep crack propagation, could be further investigated by studying the solutions given by different mesh sizes and crack shapes. *Analyses with different mesh sizes allow to critically analyze the evolution of the creep damage zone in different crack front regions. The analyses with different crack shapes allow to analyze the crack propagation front as a function of the initial defect geometry.*

Analytical and numerical approaches strongly depend on material resistance data obtained from experimental tests. In this context, the CFCG data collected during this work (Fig. 2.22), strongly demand *to perform additional tests in order to gain a more reliable crack propagation rate correlation for the $(C_t)_{avg}$ based assessment.*

The CFCG numerical model used to simulate the interaction between the creep, plastic, and cyclic plastic zones, potentially leads to a new method to calculate the creep reversal parameter C_R overcoming the experimental difficulties found at short hold times. *However, additional issues given by the numerical discretization of the problem, need to be solved in order to be able to extend the model at higher number of cycles.*

Bibliography

[1] TyssenKrupp Materials International alloy steel tubes for high-temperature service. `http://www.s-k-h.com/media/de/Service/Werkstoffblaetter_englisch/Kesselrohre_ASTM/P91_T91_engl.pdf`. Accessed: 2016-10-24.

[2] R. Sanfilippo M.E. Cristea A. Lo Conte, F. Bassi. Structural integrity assessment of pipes for high temperature applications. *ECCC-Creep and Fracture Conference 2014, May 5-7*, page Rome Italy, 2014.

[3] K. Yagi A. Saxena and M. Tabuchi. Crack growth under small scale and transition creep conditions in creep-ductile materials. *ASTM STP 1207*, 24:481–497, 1994.

[4] A. Saxena and B. Gieseke. Transients in elevated temperature crack growth. *Proceedings of MECAMAT, International Seminar on High Temperature Fracture Mechanisms and Mechanics*, (III):19–36, 1987.

[5] American Petroleum Institute, ASME. *API 579-1 / ASME FFS-1*. Washington DC, 2007.

[6] ASTM E1457-15. *Standard Test Method for Measurement of Creep Crack Growth Times in Metals*. ASTM, 2015.

[7] J.L. Bassani and F.L. McClintock. Creep relaxation of stress around a crack tip. *International Journal of Solids and Structures*, 17:79–89, 1981.

[8] Bassani J. L., Hawk D. E. and Saxena A. Evaluation of c_t parameter for characterising creep crack growth rate in the transient regime. *ASTM STP 995 Nonlinear fracture mechanics: Time-dependent fracture mechanics*, 1:7–29, 1989.

[9] Belloni G., E. Gariboldi, A. Lo Conte, M. Tono and P. Speranzoso. On the experimental calibration of potential drop system for crack length of compact tension specimen measurements. *Journal of Testing and Evaluation*, 30:461–469, 2002.

[10] British Energy Generation. *R5, Assessment Procedure for the High Temperature Response of Structures*. Issue 3, 2014.

[11] British Energy Generation Ltd. *R6: Assessment of the Integrity of Structures Containing Defects*, 2001.

[12] BSi. *BS7910:2013, Guide to Methods for Assessing the Acceptability of Flaws in Metallic Structures*. London, 2013.

[13] Chaboche J. L. Constitutive equations for cyclic plasticity and cyclic viscoplasticity. *Int. J. of Plast.*, 5:247, 1989.

[14] Cocks A. C. F. and Ashby M. F. Intergranular fracture during power-law creep under multiaxial stresses. *Metal Science*, August-September:395–402, 1980.

[15] Landes J. D. and Begley J. A. A fracture mechanics approach to creep crack growth. *Mechanics of Crack Growth*, ASTM STP 590:128–148, 1976.

[16] ASTM E139-11. *Standard Test Methods for Conducting Creep, Creep-Rupture, and Stress-Rupture Tests of Metallic Materials*. ASTM, 2011.

[17] ASTM E1820-11. *Standard Test Method for Measurement of Fracture Toughness*. ASTM, 2011.

[18] ASTM E2760-10. *Standard Test Method for Creep-Fatigue Crack Growth Testing*. ASTM, 2010.

[19] ASTM E647-13. *Standard Test Method for Measurement of Fatigue Crack Growth Rates*. ASTM, 2013.

[20] ASTM E8-15. Standard test method for tension testing of metallic materials. 2015.

[21] A. Lo Conte S. Beretta F. Bassi, A. Saxena and M.E. Cristea. Experimental and simulated displacement in cracked specimen of p91 steel under creep conditions. *Procedia Structural Integrity*, 2:911–918, 2016.

[22] S. Foletti F. Bassi and A. Lo Conte. Creep fatigue crack growth and fracture mechanisms of t/p91 power plant steel. *Materials at High Temperatures*, 32:250–255, 2015.

[23] F. Mueller, A. Scholz, C. Berger. Comparison of different approaches for estimation of creep crack initiation. *Engineering Failure Analysis*, 14:1574–1585, 2007.

[24] GKSS. *FITNET, European Fitness-for-Service Network, Project G1RT-CT-2001-05071 Procedure*. Germany, 2006.

[25] N.L. Goldman and J.W. Hutchinson. Fully plastic crack problems: the center cracked strip under plane strain. *International Journal Solids and Structures*, 11:579–591, 1975.

[26] Graham A. and Walles K. F. A. . Relationship between long- and short-time creep and tensile properties of a commercial alloy. *Journal of the Iron and Steel Institute*, 179:104–121, 1955.

[27] P.S. Grover. Creep-fatigue crack growth in cr-mo-v base material and weldments. *PhD Thesis. Georgia Institute of Technology*, 1996.

[28] Grover P. S. and Saxena A. Modelling the effect of creep-fatigue interaction on crack growth. *Fatigue FractEngng Mater Struct*, (22):111–122, 1999.

[29] H. Riedel and J. R. Rice. Tensile cracks in creeping solids. *Fracture mechanics: twelfth conference*, (ASTM STP 700):112–130, 1980.

[30] Hyde T. H., Sun W. and Tang A. Determination of material constants in creep continuum damage constitutive equations. *Strain*, August:83–90, 1998.

[31] K.H. Keienburg J. Edwald and K. Maile. Estimation of manufacturing defects in the creep range. *Nucl. Engng. a. Des.*, 87:389–398, 1985.

[32] M. Tramer G. Schellenberg F. Mueller J. Granacher, A. Klenk and J. Ewald. Creep fatigue crack behavior of two power plant steels. *International Journal of Pressure Vessels and Piping*, 78:909–920, 2001.

[33] H. Ernst J. Joyce and P. Paris. Direct evaluation of j-resistance curves from load displacement records. *ASTM STP*, 700:222–236, 1980.

[34] G. A. Webster. K. M. Nikbin and C.E. Turner. Relevance of nonlinear fracture mechanics to creep crack growth. *Crack and Fracture*, ASTM STP 601:47–62, 1976.

[35] Kachanov L. M. Time to the fracture process under creep conditions. *Izv. Akad. SSSR OTN Teckh. Nauk,*, 8:26, 1958.

[36] A. Saxena K.B. Yoon and P.L. Liaw. Characterization of creep-fatigue crack growth behavior under trapezoidal waveshape using c_t-parameter. *International Journal of Fracture*, 59:95–114, 1993.

[37] Kumar V., German M. D. and Shih C. F. *An Engineering Approach for Elastic-Plastic Fracture Analysis, NP-1931*. Electric Power Research Institute, 1981.

[38] F.R. Larson and J. Miller. *Transactions ASME*, 74:765–771, 1952.

[39] Liu Y. and Murakami S. Damage localization of conventional creep damage models and propositions of a new model for creep damage analysis. *JSME International Journal Series A*, 41(1):57–65, 1998.

[40] D.L. McDowell N.B., Adefris and A. Saxena. An alternative analytical approximation of the c_t parameter. *Fatigue & Fracture of Engineering Materials & Structures*, 21:375–385, 1998.

[41] P. Paris and F. Erdogan. A critical analysis of crack propagation laws. *Journal of Basic Engineering*, Transactions of the American Society of Mechanical Engineers:528–534, 1963.

[42] Prager, M. *Development of the MPC Project Omega Method for Life Assessment in the Creep Range,*. ASME, 1994.

[43] J.R. Rice. A path-independence integral and the approximate analysis of strain conocentration by notches and cracks. *Journal of Applied Mechanics, Trans. ASME*, 35:379–386, 1968.

[44] Riedel H. *Fracture at High Temperatures*. Springer-Verlag, 1987.

[45] S. Maleki, Y. Zhang, K. Nikbin. Prediction of creep crack growth properties of p91 parent and welded steel using remaining failure strain criteria. *Engineering Fracture Mechanics*, 77:3035–3042, 2010.

[46] Saber M. *Experimental and finite element studies of creep and creep crack growth in P91 and P92 weldments*. University of Nottingham, 2011. Ph.D. thesis.

[47] A. Saxena. Mechanics and mechanisms of creep crack growth. *Fracture Mechanics: Microstructure and Micromechanisms*, pages 283–334, 1989.

[48] A. Saxena. Creep crack growth in ductile materials. *Engineering Fracture Mechanics*, 40:721–736, 1991.

[49] Saxena A. Creep crack growth under non steady-state conditions. *Fracture Mechanics*, 7(ASTM STP 905):185–201, 1986.

[50] Saxena A. *Nonlinear Fracture Mechanics for Engineers*. CRC Press, Boca Raton, FL, 1998.

[51] A. Saxenas. Evaluation of c^* for characterization of creep crack growth behavior of 304 stainless-steel. *Fracture Mechanics: Twelth Conference*, ASTM STP 700:131–151, 1980 Philadelphia.

[52] R. Viswanathan. Damage mechanisms and life assessment of high-temperature components. *AMS International, Metals Park, Ohio*, 1989.

[53] W. Sun, T.H. Hyde, A.A. Becker, J.A. Williams. Steady-state creep reference rupture stresses for internally pressurized pipes for use un life prediction. *International Journal of Pressure Vessels and Piping*, 79:135–143, 2002.

[54] Wen Jian-Feng and Tu Shan-Tung. A multiaxial creep-damage model for creep crack growth considering cavity growth and microcrack interaction. *Engineering Fracture Mechanics*, 123:197–210, 2014.

APPENDIX A

Computational Resources and Times for FE Analyses

Table A.1: *Computational resources and times for FE analyses.*

Simulation	Elements number	Nodes number	Hardware	Time required [h]
CCG C(T) 2D	702	765	4 cores 8 GB RAM	20 min
CCG C(T) 3D	16758	18751	16 cores 128 GB RAM	14 h 30 min
CCG Pipe	48250	53197	16 cores 128 GB RAM	35 h
Pipe Stat. Crack	48250	53197	16 cores 128 GB RAM	10 h 45 min